KAUNAS UNIVERSITY OF TECHNOLOGY

AGNĖ ŠULČIŪTĖ

SYNTHESIS, STRUCTURE AND ELECTROCHEMICAL PROPERTIES OF ZnO AND Zn-Co OXIDE COATINGS

Doctoral Dissertation
Physical Sciences, Chemistry (03P)

2016, Kaunas

UDK 546.47-31 + 544.654.2 + 544.526.5](043.3).

The research was carried out in 2011–2015 at Kaunas University of Technology, Faculty of Chemical Technology, Department of Physical and Inorganic Chemistry.

Scientific Supervisor:

Prof. Dr. Eugenijus VALATKA (Kaunas University of Technology, Physical Sciences, Chemistry – 03P).

English Language Editor:

dr. Armandas RUMŠAS (Publishing house "Technologija").

Lithuanian Language Editor:

Rozita ZNAMENSKAITĖ (Publishing house "Technologija").

ISBN 978-609-02-1178-6

KAUNO TECHNOLOGIJOS UNIVERSITETAS

AGNĖ ŠULČIŪTĖ

ZnO ir Zn–Co oksidinių dangų sintezė, struktūra ir elektrocheminės savybės

Daktaro disertacijos santrauka
Fiziniai mokslai, chemija (03P)

2016, Kaunas

UDK 546.47-31 + 544.654.2 + 544.526.5](043.3).

Disertacija rengta 2011–2015 metais Kauno technologijos universitete, Cheminės technologijos fakultete, Fizikinės ir neorganinės chemijos katedroje.

Mokslinis vadovas:

Prof. dr. Eugenijus VALATKA (Kauno technologijos universitetas, fiziniai mokslai, chemija – 03P)

Anglų kalbos redaktorius:

Armandas RUMŠAS (Leidykla "Technologija")

Lietuvių kalbos redaktorė:

Rozita ZNAMENSKAITĖ (Leidykla „Technologija")

ISBN 978-609-02-1178-6

CONTENTS

SYMBOLS AND ABBREVIATIONS

a, b – Tafel slope constants
AAS – atomic absorption spectroscopy
a.u. – arbitrary units
CB – conduction band
Co–Pi – cobalt phosphate bulk catalyst
CPS – counts per second
CV – cyclic voltammetry
DSC–TG – differential scanning calorimetry and thermogravimetry
E – electrode potential
E_g – band-gap energy
e^- – electron
ECD – electrochemical deposition
EDX – energy dispersive X-ray spectroscopy
EPD – electrophoretic deposition
FT-IR – Fourier transform infrared spectroscopy
h^+ – hole
HER – hydrogen evolution reaction
I – current
IPCE – incident photon-to-current efficiency
j – current density
j_{ph} – photocurrent density
OER – oxygen evolution reaction
SEM – scanning electron microscopy
SHE – standard hydrogen electrode
TEC 15 – type of fluorine tin oxide (FTO) coated glass plate
v – potential scan rate
VB – valence band
XRD – X-ray powder diffraction
XPS – X-ray photoelectron spectroscopy
wt. % – weight percentage
η – overpotential
θ – Bragg diffraction angle
λ – wavelength

INTRODUCTION

Relevance of the work. Transition metal oxides have been widely studied due to their good electrocatalytic activity for many types of electrode reactions such as oxygen or hydrogen evolution, oxygen reduction and organic electrosynthesis. Particular attention is paid to the search of efficient and low-cost electrocatalysts suitable for the implementation of the water photo-splitting process. In this regard, zinc oxide (ZnO) is a material of prime choice. It is widely used in various industrial applications, such as catalysts, rubber and concrete additives, photovoltaics, pigments, gas sensors and mixed oxide varistors; however, its use in aqueous photoelectrochemical systems is hindered by rather fast photocorrosion. In order to overcome this drawback, recent research efforts have been systematically focused on the improvement of ZnO stability and catalytic properties by mixing it with 3d transition metal oxides. Mixed metal oxides exhibit a novel set of physicochemical properties that are completely different from those of individual metal oxides. Experimental evidence shows that the bulk Zn–Co oxides exhibit enhanced adsorptive, catalytic, optical and magnetic properties. However there is a lack of information concerning the use of mixed Zn–Co oxides in aqueous photoelectrochemical systems. Another approach to enhancing the performance of ZnO is a modification of its surface with an oxygen evolving catalyst (OEC). Recently, inorganic cobalt-phosphate complex (termed Co–P_i) has emerged as a particularly promising OEC based on earth-abundant elements.

Aim of the work. To synthesize zinc oxide and zinc-cobalt oxide coatings on stainless steel and electroconductive glass, to investigate their structure and electrochemical properties.

In order to achieve the goal we had to solve the following tasks:

1. To form nanostructured ZnO coatings on stainless steel by using electrophoretic deposition and to evaluate the influence of synthesis conditions on their photoactivity.
2. To synthesize ZnO coatings on stainless steel by using the electrochemical deposition method and to characterize them.
3. To prepare mixed Zn–Co oxide coatings on stainless steel and conductive glass, to evaluate their structure, morphology, optical properties and photoelectrochemical activity in aqueous solutions.
4. To evaluate the influence of the oxygen-evolving Co–P_i catalyst on the photoelectrochemical activity of the prepared coatings.

Scientific novelty of the dissertation. The structure and the photoactivity of electrophoretically and electrochemically deposited ZnO coatings on stainless steel were compared. Structural, morphological and photoelectrochemical properties of mixed Zn–Co oxide coatings on stainless steel and conductive glass were explored in detail. The influence of Co–P_i catalyst on the photoelectrochemical activity of the prepared coatings in phosphate buffer solutions was also evaluated.

Practical significance of the dissertation. The results presented in the dissertation expand the knowledge in the field of semiconductor

photoelectrocatalytic systems and facilitate the real life application of semiconductor photoelectrocatalytic systems for the water anodic oxidation. It was demonstrated that mixed Zn-Co oxide coatings on FTO substrate serve the objective fairly well and thus are highly promising materials.

Approval and publication of research results. Results of the research are presented in 11 publications: 3 of them are presented in journals listed in the *Thomson Reuters™ Web of Science* publication database with a citation index; 1 article was published in a reviewed periodical scientific journal included into the list of *other databases*; 7 articles were printed in proceedings of conferences.

Structure and content of the dissertation. The dissertation consists of an introduction and chapters covering a review of scholarly writings pertaining to the topic of the thesis, the applied materials and methods, the results of the research and their discussion, conclusions, a list of references and a list publications on the topic of the dissertation. The list of references includes 164 bibliographic sources. The main results are discussed on 93 pages and illustrated in 12 tables and 63 figures.

Statements presented for the defense:

1. Photoactivity of nanostructured ZnO coatings on stainless steel under UV irradiation depends on their annealing temperature and the amount of ZnO.
2. Electrochemically deposited *n*-type Zn-Co oxide coatings are characterized by high photoelectrochemical activity in aqueous solutions and are promising materials for water anodic oxidation.
3. Co–Pi catalyst significantly increases the electrocatalytic activity of the ZnO coating in the phosphate buffer solution; however it does not enhance the properties of mixed Zn-Co oxide coatings.

1. LITERATURE REVIEW

1.1. Basics of photocatalysis

Photocatalytic reaction is usually defined as a chemical reaction induced by absorption of light quanta by a solid semiconducting material (termed "photocatalyst") [1]. The photocatalyst acts catalytically and remains chemically unchanged during the reaction under photoirradiation. The main difference between thermal catalysis and photocatalysis is that thermal catalysts are activated by heat while photocatalysts are activated by photons of the appropriate energy. In numerous papers it has been reported that the activation energy of the photocatalytic reaction is very small compared to that of the thermal catalytic reaction. For the first time, the term 'photocatalysis' was introduced by Karl Hauffe (*Heterogeneous Photocatalysis*; joint research with W. Doerfler) in 1964 as a result of his investigation of CO oxidation using ZnO under UV irradiation.

Photocatalytic reactions are classified into two major categories: homogenous and heterogeneous. In recent years, heterogenous photocatalysis has been studied more intensively because of its potential use for such environmental and energy-related processes as mild or total oxidations, dehydrogenation, metal deposition, water detoxification/decomposition, gaseous pollutant removal, etc. Heterogeneous photocatalysis can be carried out in various media: in the gas phase, pure organic liquids or aqueous solutions.

The principle of photocatalysis is explained in terms of the electronic structure of semiconducting materials using the band model. According to this model, the electronic structure of semiconductors (e.g. ZnO, ZnS, TiO_2, $SrTiO_3$, CdS, etc.) is represented by a valence band (VB) filled with electrons and a vacant conduction band (CB). The energy difference between the lowest energy level of the CB and the highest energy of the VB is known as the band-gap energy (E_g). Photocatalysis over a semiconductor is initiated as a result of the absorption of a photon with the energy equal to, or greater than, the band-gap of the semiconductor producing electron-hole pairs. Holes and photoelectrons that are formed in the semiconductor particle under irradiation exhibit strong oxidation-reduction properties. These charge carriers can not only take place in the oxidation-reduction reaction with the surface compounds but also can oxidize or reduce the semiconductor itself.

For example, the irradiation of such semiconductor particles as ZnS generates e_{cb}^- and h_{vb}^+ as described previously. A competition reaction often occurs among water, oxygen, organic molecules and trace metals which may be present in the system. As a result, various radical species are formed in aqueous solutions. It is commonly accepted that there are two routes through which $^{\bullet}OH$ radicals can be formed. The reaction of the valence-band "holes" (h_{vb}^+) with either adsorbed H_2O or with adsorbed OH^- ions on the ZnS (or ZnO, TiO_2) particle takes place [2, 3]:

$$ZnS\left(h_{vb}^{+}\right) + H_2O_{ads} \longrightarrow ZnS + HO^{\bullet}_{ads} + H^+ \quad (1.1)$$

$$ZnS\left(h_{vb}^{+}\right) + HO^{-}_{ads} \longrightarrow ZnS + HO^{\bullet}_{ads} \quad (1.2)$$

In general, such donor (D) molecules as H_2O will adsorb and react with a hole in the valence-band whereas the acceptor (A), for instance, O_2, will also be adsorbed and react with the electron in the conduction band (e_{cb}^-) as shown in equations 1.3 and 1.4.

$$ZnS\left(h_{vb}^{+}\right) + D_{ads} \longrightarrow ZnS + D_{ads}^{+} \quad (1.3)$$

$$ZnS\left(e_{cb}^{-}\right) + A_{ads} \longrightarrow ZnS + A_{ads}^{-} \quad (1.4)$$

Oxygen can trap conduction-band electrons thus forming superoxide ion $O_2^{\bullet -}$ as demonstrated in equation (1.5). These superoxide ions can react with hydrogen ions (formed by splitting water) with $HO_2^{\bullet}$ as the initial product of the reaction:

$$ZnS\left(e_{cb}^{-}\right) + O_{2ads} + H^{+} \longrightarrow ZnS + HO_2^{\bullet} \longrightarrow O_2^{\bullet -} + H^{+} \quad (1.5)$$

Hydroxide peroxide can be formed from a $HO_2^{\bullet}$ radical via the following reaction:

$$ZnS\left(e_{cb}^{-}\right) + HO_2^{\bullet} + H^{+} \longrightarrow H_2O_2 \quad (1.6)$$

Cleavage of H_2O_2 by one of the ensuing reactions (equations 1.7, 1.8 and 1.9) may yield an $HO^{\bullet}$ radical.

$$H_2O_2 + h\upsilon \longrightarrow 2HO^{\bullet} \quad (1.7)$$

$$H_2O_2 + O_2^{\bullet -} \longrightarrow HO^{\bullet} + O_2 + HO^{-} \quad (1.8)$$

$$H_2O_2 + ZnS\left(e_{cb}^{-}\right) \longrightarrow HO^{\bullet} + HO^{-} + ZnS \quad (1.9)$$

1.2. Photocatalytic materials

A wide range of semiconductors may be used for photocatalysis including TiO_2, ZnO, ZnS, MgO, WO_3, Fe_2O_3, CdS and a number of others. The ideal photocatalyst should possess the following characteristics [4]:

- high sensitivity suitability towards the visible or near-UV spectral region;
- suitable conduction and valence band positions determining the oxidation-reduction properties of photoelectrons and holes;
- efficient charge transport in the semiconductor;
- biological and chemical stability in the reaction medium under irradiation and in the dark;
- low cost and lack of toxicity.

The first requirement is determined by the band gap of the material. The minimum band gap necessary for the photo-splitting of water is estimated to be 1.23 eV [5]. However, taking into account the thermodynamic losses and the overpotentials that are required to ensure sufficiently fast reaction kinetics, it is

estimated that the band gap should be at least 1.9 eV. This corresponds to the absorption of light with a wavelength shorter than 650 nm. It was suggested that the optimum band gap is 2.03 eV which should ensure the maximum solar-to-hydrogen efficiency up to 16.8%.

In order to drive the photocatalytic processes in aqueous solutions, the band edges of the semiconductor should straddle the water reduction and oxidation potentials (Fig. 1.1.). Only a few materials are known to fulfill this requirement. In addition, some of them (Cu_2O, CdS) are unstable in water under UV-Vis irradiation due to the photocorrosion. Others, like $SrTiO_3$ or $KTaO_3$, are characterized by the large band gap energy. It means that these materials are active only in the region of UV irradiation.

Chemical and biological stability, low cost and non-toxicity of photocatalytic materials are parameters of paramount importance from the practical point of view. The photostability of a semiconductor is determined by the standard potential for anodic decomposition relative to the oxidation potential of water (Figure 1.1.). Most metal oxide semiconductors are kinetically stable against photocorrosion whereas most chalcogenide semiconductors are unstable and require sacrificial reagents [6].

The third requirement concerning an efficient charge transport is determined by the electronic band structure of the semiconducting material. In some semiconductors this requirement is easily fulfilled (TiO_2, ZnO, WO_3) while in others (the most important example is α-Fe_2O_3) the charge transport is slow and causes low overall efficiency.

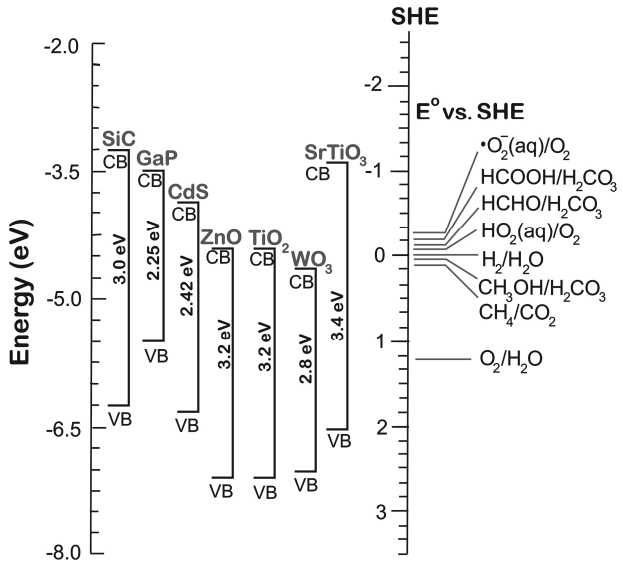

Fig. 1.1. Band-gap positions of some semiconductor photocatalysts in absolute and SHE scales relative to the energy levels of various redox couples in water [6]

Photocatalysts are activated with light in a number of competing processes that schematically are presented in Figure 1.2. Steps (1) and (2) show electronic processes of e^- and h^+ active centers on the photocatalyst surface. These processes have to compete with deactivation processes (3) and (4) leading to e^- and h^+

recombination. The increase of the distance toward the surface of the active centers of photogenerated electrons and holes also increases the probability of their recombination. The increase in the photocatalyst surface enhances the catalyst activity because the number of active centres depends on the surface area. In order to hinder the recombination process and to increase the photocatalytic activity, it is important that the semiconductor particles must be small and well-crystallized.

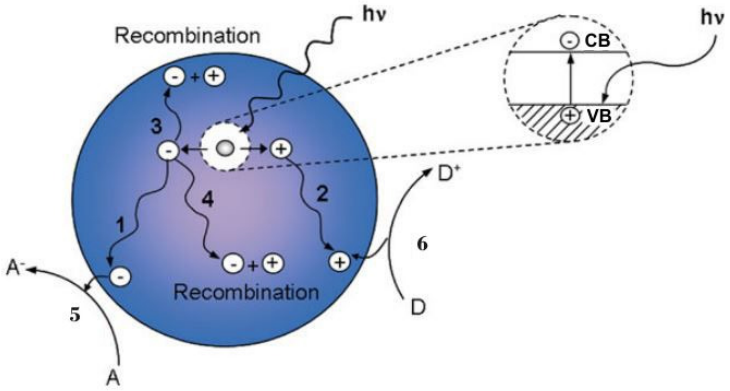

Fig. 1.2. Schematic diagram showing the charge carrier dynamic upon irradiation of a semiconductor: 1 – electron transport to the surface, 2 – hole transport to the surface, 3 – surface recombination, 4 – bulk recombination, 5 – electron transfer to an acceptor molecule, 6 – hole trapping by a donor molecule [7]

Photocatalytic activity can be improved by covering the surface of the catalyst with co-catalysts [8] capturing conduction-band electrons or valence-band holes and thereby reducing the likelihood of electron–hole recombination. It permits to transfer electrons and holes to the surface of water molecules, thus reducing the activation energy for the reduction/oxidation of water. Examples of active oxygen evolution catalysts are iridium and ruthenium oxides, cobalt-based compounds whereas the most efficient hydrogen evolution catalysts are known to be Pt, Rh, ruthenium or nickel oxides [5].

1.3. Photoelectrochemical water splitting

Water is oxidized to oxygen (oxygen evolution reaction, OER) and reduced to hydrogen (hydrogen evolution reaction, HER). The reversible cell potential for this reaction is 1.23 V (vs. SHE). The overall water splitting reaction is a thermodynamically uphill reaction with a large positive change in Gibbs free energy (ΔG^0 = +237 kJ· mol^{-1}, equal to 1.23 eV) involving multiple electron transfer processes [9]. The photon energy is used to overcome the large positive change in the Gibbs free energy for water splitting by generating electrons and holes that can respectively reduce and oxidize the water molecules adsorbed on photocatalysts.

In order to achieve overall water splitting, a number of thermodynamic conditions are required to be fulfilled [10] such as: the bottom of the conduction band of the photocatalyst must be located at a more negative potential than the proton reduction potential ($2H^+/H_2$=0 V vs. the standard hydrogen electrode (SHE)

at pH 0) whereas the top level of the valence band has to be more positive than the redox potential of O_2/H_2O (+1.23 V vs. SHE at pH 0). Therefore, the band gap should be wider than 1.23 eV. It should be emphasized that the semiconductor reducing ability increases when the bottom of the conduction band becomes more negative and the ability to oxidize increases when the upper level of the valence band is pushed towards a more positive potential.

The water splitting reaction ($2H_2O \rightarrow 2H_2 + O_2$) is composed of two half-reactions: the hydrogen evolution and oxygen evolution reactions (HER and OER, respectively) [11]:

HER $2H^+ + 2e^- + \rightarrow H_2$ (acidic) (1.10)

$2H_2O + 2e^- \rightarrow H_2 + 2HO^-$ (basic) (1.11)

OER $2H_2O \rightarrow 4H^+ + HO^- + O_2 + 4e^-$ (acidic) (1.12)

$4HO^- \rightarrow 2H_2O + O_2 + 4e^-$ (basic) (1.13)

It can be concluded that light-driven water splitting is a three-stage process that is initiated when a photo-semiconductor absorbs light photons with energies greater than its band gap energy (Eg) [8]. Firstly, such absorption creates excited photo-electrons in the conduction band (CB) and holes in the valence band (VB) of the semiconductor. Secondly, the charge separation ensues, and the migration of photogenerated electron–hole pairs from the bulk of the semiconductor towards the reaction sites on the photocatalyst surface occurs. Finally, as a result of the chemical reactions taking place on the surface, water molecules release oxygen and hydrogen.

Two systems can be envisaged for the realization of photoelectrochemical water splitting [8, 10, 12]:

1. A photoelectrochemical cell constituted of two electrodes immersed in aqueous solutions, one of which is a photocatalyst sensitive to light (Fig. 1.3.).

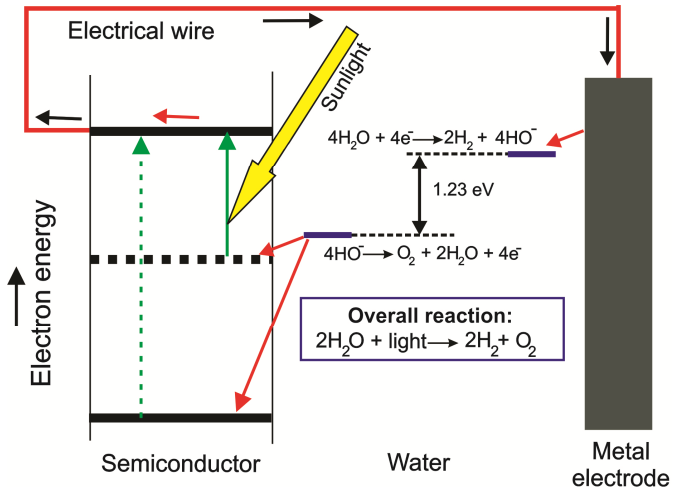

Fig. 1.3. Photoelectrochemical cell for water splitting [5]

2. Solid photocatalysts are in the form of particles suspended in an aqueous solution. In the solution, each particle acts as a microphotoelectrode performing both the oxidation and reduction reactions of water on its surface (Fig.1.4.). Up to now, the efficiency benchmark for photoelectrochemical devices is a monolithic photoelectrochemical cell composed mainly of GaAs and $GaInP_2$ compounds [12]. An impressive solar-to-hydrogen efficiency of 12.4% was achieved with this cell; however, high costs and the very poor stability in the aqueous solution of the used semiconducting materials hinder their practical application.

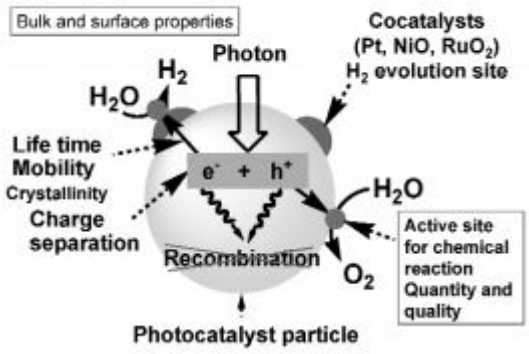

Fig. 1.4. Processes taking place during the photocatalytic reaction in a powdered system [10]

Particulate photocatalytic systems exhibit disadvantages compared to photoelectrochemical cells, specifically, (1) the separation of charge carriers is not as efficient as it is the case with photoelectrode systems, and (2) there are difficulties associated with the effective separation of the stoichiometric mixture of oxygen and hydrogen so that the reverse reaction could be avoided [8]. Also, while using the photocatalyst, it is important to be aware of the stability, mobility and lifetime of charge carriers, the crystallinity of the powder (area, size, and porosity), etc. However, the advantage of particulate photocatalytic systems is that they are slightly cheaper and less complex.

Tafel plots have been long known to fit the experimental data obtained in studies of the activation overpotential such as the evolution of hydrogen and oxygen at various electrodes. Thus the passage of the net current causes the potential to deviate from its equilibrium value called the activation overpotential η [13]. For many electrochemical reactions, Tafel plots describe the interrelationship between the reaction rate (given in terms of the current density *j* measured in $A \cdot cm^{-2}$) and the electrode overpotential η [13]:

$$j = j_0\left[\exp\left(-\frac{\alpha z F \eta}{RT}\right) - \exp\left(\frac{(1-\alpha) z F \eta}{RT}\right)\right]; \qquad (1.14)$$

j_0 – the exchange current density, α – transfer coefficients, η – overpotential.

η is the surface or activation overpotential defined as the deviation of the electrode potential away from its equilibrium potential, i.e., $\eta = E - E_{eq}$. The first term on the right side denotes the anodic reaction rate, and the second term gives the rate of the cathodic reaction, i.e., anodic currents (forward reaction dominating) are positive, whereas cathodic currents are negative [13].

This overpotential is caused by slow kinetics in the electron transfer reaction and must be distinguished from the concentration of oxidized and reduced species. For large positive or large negative overpotentials (where η >50 to100 mV), one of the exponential terms will dominate over the other. The resulting relationship can be rewritten in the general form [13]:

$$\eta = a + b \ln j \tag{1.15}$$

This equation is known as the Tafel equation, and constants *a* and *b* are defined as the Tafel slope.

For the cathodic reaction:

$$a = \frac{RT}{\alpha z F} \ln j_0; \;\; b = -\frac{RT}{\alpha z F}, \tag{1.16}$$

For the anodic reaction:

$$a = -\frac{RT}{(1-\alpha) z F} \ln j_0; \;\; b = \frac{RT}{(1-\alpha) z F}. \tag{1.17}$$

From the equations it is evident that overpotential η and ln*j* should exhibit linear dependence. It was discovered that these values are linear when η > 50 mV.

The most widely accepted representation to show the relationships between material fundamental properties and electroactivity is the so-called volcano plot. The volcano plot provides a graphical representation of the dependence of the exchange current density on the strength of the bond between the catalyst surface and hydrogen.

In alkaline media, the overpotentials required to achieve a set current density were measured for the transition metals [14] (Fig. 1.5.) . A plot of such data against the periodic group gives a similar volcano relation with Pt, Pd, and Ni as the most active pure metals. Hence conclusions can be drawn that the HER (hydrogen evolution reaction) mechanism for a given metal is the same in both acidic and basic media.

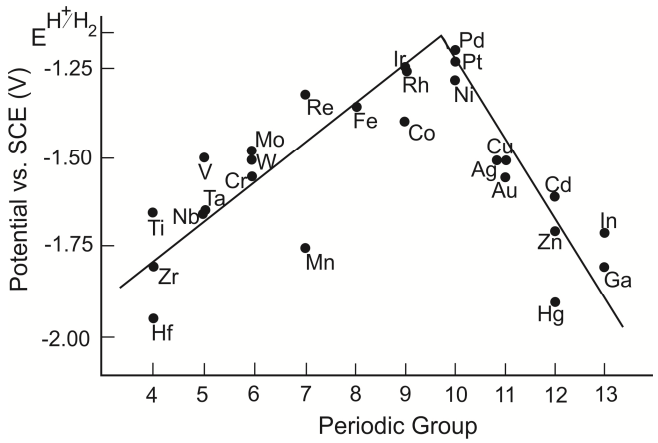

Fig. 1.5. The volcano relation based on potentials [14]

Stefano Trasatti suggested a volcano curve for OER catalysts using the relationship between the OER overpotential and the strength of the metal-oxygen bonds in the surface oxide [15]. The volcano plot is derived on the grounds of correlating the overpotential at a fixed current density to the enthalpy of a lower to-higher oxide transition (Fig. 1.6.). Oxides to the left of the volcano plot maximum show that the required overpotential increases as the strength of the oxide-intermediate interaction increases. Oxides to the right are easily oxidized. Hence these oxides exhibit a high coverage of the absorbed intermediate thus increasing the overpotential for oxygen evolution [15].

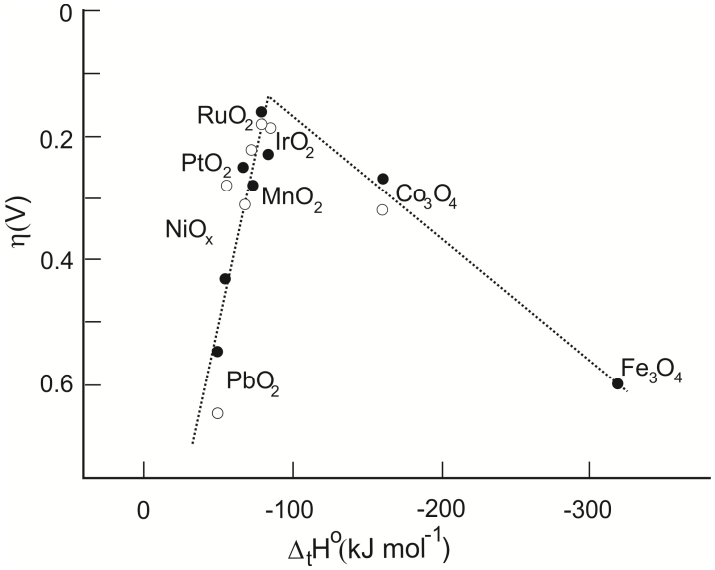

Fig. 1.6. OER volcano plot from Trasatti [15]. Filled circles: in acidic media. Empty circles: in alkaline media

RuO_2 and IrO_2 possess the lowest overpotentials and optimized bond strengths, which means that oxygen atoms are easily adsorbed/desorbed on their surface.

Materials to the left of the volcano plot maximum feature a relatively weak metal-oxygen bond whereas materials to the right, for instance, Co_3O_4 and Fe_3O_4, are easily oxidized and strongly bound with oxygen. Hence the desorption of gaseous oxygen is kinetically limited. Trasatti establishes that oxygen evolution can only proceed when the electrode potential is higher than the potential of the metal/metal oxide couple.

A number of scientists have recently been focusing on the oxygen evolution reaction (OER) and the research of new OER catalysts. Electrocatalysts for OER are usually the noble metals (e.g. Pt, Au, Ir, Rh, Ru, Ag) whose oxides tend to be more active than the metals themselves. Pt is a relatively poor electrocatalyst for oxygen evolution. This is caused by the formation of a poorly conductive platinum monooxide layer during the OER. For example, Ru and Ir form conductive metallic oxides and thus have been used as OER electrocatalysts. Ru oxide is the best catalyst for oxygen evolution. Yet it is thermodynamically unstable due to a possible formation of higher valency Ru oxides. That is why Ru oxide forms corrosion products at high anodic potentials. Ir oxide exhibits strong resistance to corrosion during oxygen evolution but exhibits lower activity than Ru [14]. For the electrode stability, other metal oxides, e.g. ZnO, TiO_2, SnO_2, etc., are used as stable anodes for OER [16, 17]. The oxides of the first row transition metals, Ni and Co in particular, exhibit the desirable electrocatalytic activity for the OER. Co, Ni, Mn and Fe-based complex oxides and crystal structures improve the OER activity and stability in alkaline media [11, 17].

Recently, nanostructural catalysts have been studied for the OER. Lee et al. reported that rutile RuO_2 and Iridium (IV) oxide IrO_2 nanoparticles (~ 6 nm) show high intrinsic specific activity as well as OER mass activity in both acidic and alkaline media [18]. Esswein et al. reported the acitvity dependence on the size of cubic nanoparticles of Co_3O_4 in oxygen evolution reaction in alkaline media. An increase in the surface area of the catalyst due to the controlled particle size increases the OER activity [19]. Nocera et al. observed that Co-phosphate ($Co–P_i$) bulk catalysts electrodeposited in a cobalt nitrate/phosphate buffer solution demonstrates highly promising water oxidation activity in the neutral and mildly basic pH regimes [20, 21]. Thus $Co–P_i$ possesses a self-repair mechanism involving the dissolution/redeposition of the Co ion during the oxygen evolution. The Co-phosphate layer can be deposited on such semiconductor materials as ZnO [16, 22], TiO_2 [23], WO_3 [24] or mixed oxide films [17] and are extremely promising materials for photelectrochemical water splitting. The $Co–P_i$ catalyst layer can be formed in two fundamental ways:

- Electrochemically. Electrochemical deposition in 1 M phosphate buffer (pH=7) containing 0.5 mM Co^{2+} at 1.1 V constant potential [17, 21];
- Photochemically. Prepared photoanode is immersed in 0.1 M of phosphate buffer (pH=7) solution containing 0.5 mM Co^{2+} and is illuminated with an UV radiation source [16, 20].

Nocera and Surendranath [17] suggested a pathway for the OER by $Co–P_i$ as shown in Figure 1.7.

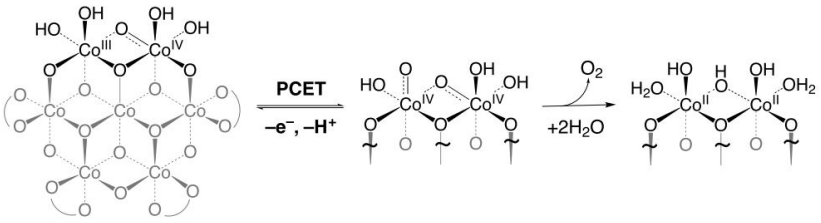

(1.18)

Fig. 1.7. Pathway for OER by Co–P_i. A Proton-coupled electron transfer (PCET) equilibrium proceeded by a turnover-limiting O—O bond forming step is consistent with the electrokinetic and spectroscopic data. The curved lines denote a phosphate, an OH_x terminal or bridging ligands [17].

Furthermore, Ni-borate catalysts deposited from the nickel/borate buffer solution were reported [25]. Nocera et al. suggests that these catalysts deposited on conducting substrates such as indium tin oxide (ITO) and fluorine-doped tin oxide (FTO) may be used under mild conditions and at current densities with a non-concentrated solar photovoltaic cell.

1.4. Zinc oxide properties, synthesis and application

1.4.1. Properties and application

Zinc oxide (ZnO) is well-known as an n-type semiconducting material with a room temperature band gap of ~3.37 eV and exciton binding energy of 60 meV [26]. It crystallizes predominantly in the hexagonal wurtzite-type structure: the Zn atoms are tetrahedrally coordinated to four O atoms where the Zn *d* electrons hybridize with the O *p* electrons. This material is characterized by specific optical, electrical and thermal properties that are very attractive for diverse industrial applications (catalysts, rubber and concrete additives, photovoltaics, pigments, chemical and gas sensors, mixed-oxide varistors, etc.) [26-30]. Some physical properties are outlined in Table 1.1. [26]:

Table 1.1. ZnO physical properties

Physical properties	Units
Density	5.65–5.68 g cm^{-3}
Refractive index	1.95–2.1
Melting point	2248 K
Heat capacity at 298 K	40.26 $J{\cdot}mol^{-1}{\cdot}K^{-1}$
Heat capacity at 373 K	44.37 $J{\cdot}mol^{-1}{\cdot}K^{-1}$
Thermal conductivity	25.2 $W{\cdot}m^{-1}{\cdot}K^{-1}$
Crystal structure	hexagonal, wurtzite
Mohs hardness	4–4.5

Therefore, ZnO and related materials can be potentially used in such photocatalytic processes as oxidation of organic compounds or water splitting into hydrogen and oxygen. In order to increase the photocatalytic efficiency of ZnO particles, they can be deposited on electroconductive substrates and biased positively by applying an external voltage. In this way, the rate of photoelectron and hole

recombination is significantly reduced; consequently, the rate of the surface reactions is increased.

1.4.2. Synthesis

ZnO possesses a highly beneficial feature as it can be grown at relatively low temperatures (to be more specific, below 773 K) and can be obtained in variously sized and shaped particles such as granular, needle-shaped, flower-shaped, nano-rods, wires, sheets, plates, rings, tubes, etc. [10]. ZnO synthesis may be roughly divided into two groups: bulk industrial production methods and laboratory methods.

1.4.2.1. Industrial Production

Nowadays, zinc oxide manufacturers mainly use residues and secondary zinc. Worldwide, ZnO is mostly produced industrially by pyrometallurgical methods (e.g., the indirect process (French), the direct process (American), or spray pyrolysis) or by hydrometallurgical methods [30]. Each of the above mentioned processes results in the production of ZnO grades with relatively different properties required for different applications. The formal specifications of the major types of ZnO available industrially are listed in Table 1.2. [29].

Table 1.2. Typical properties of various grades of zinc oxide according to ASTM D4295-89[a]

Property	ASTM method	American (direct) type	French (indirect) type			Secondary types		
			Class 1	Class 2	Class 3	Chemical	Metallurgical	
							Class 1	Class 2
ZnO (%)	D3280	99.0	99.5	99.5	99.5	95.0	99.0	99.0
Pb (%)	D4075	0.10	0.002	0.002	0.002	0.10	0.10	0.10
Cd (%)	D4075	0.05	0.005	0.005	0.005	0.05	0.05	0.05
S (%)	D3280	0.15	0.02	0.02	0.02	0.15	0.02	0.02
Heat loss at 378 K (%)	D280	0.25	0.03	0.025	0.025	0.50	0.25	0.25
Sieve residue, 45 μm (%)	D4315	0.10	0.05	0.05	0.05	0.10	0.25	0.25
Surface area $m^2 \cdot g^{-1}$	D3037	3.5	9.0	5.0	3.5	40.0	5.0	3.5
Manufacturing process	-	Pyrometal-lurgical reduction of ZnO	Combustion of pure Zn			Wet chemical reactions	Combustion of Zn dross and scrap	

[a]2005, Standard Classification for Rubber Compounding Materials – Zinc Oxide; copyright ASTM International, 100 Barr Harbor Drive, West Conshohocken, PA 19428

1.4.2.2. Laboratory methods

ZnO can be deposited by using a number of methods, specifically: chemical vapour deposition [31-34], radio frequency magnetron sputtering [29, 35], molecular beam epitaxy, sol-gel, hydrothermal synthesis, electrophoretic and electrochemical deposition [29, 30, 36-43].

1. *Chemical vapour deposition (CVD)* technology produces high-quality films and is also applicable in large-scale production. This technique is widely used in the fabrication of epitaxial films for various GaN-based optoelectronic devices, and it might be expected to serve for future applications of ZnO. CVD has several modifications depending on what kind of precursors is used. When metalorganic precursors are used, the technique is called MOCVD [31], metalorganic vapour-phase epitaxy (MOVPE) or OMVPE. When hydride or halide precursors are used, the techniques are named CVD and VPE respectively. The reactions take place in a reactor where the required temperature profile is created in the gas flow direction. ZnO may be obtained from:

a. halide (VPE). H_2 is used as the carrier gas at a pressure of < 133 Pa and the flow rate of 40 ml · min^{-1}. ZnO powder is obtained at a temperature of 1043 K. The ZnO coatings obtained by using this method possess excellent crystal, electrical, and luminescence properties [32].

b. hydride (CVD). O_2 is used as the carrier gas; the sources of Zn and O are Zn chloride ($ZnCl_2$) or Zn iodide (ZnI_2) while the substrate is sapphire (0001). The reaction takes place in the standard atmospheric pressure at the room temperature [33]. When the iodide system is used, ZnO layers exhibit superior optical and structural properties. The main advantage of this method is the prominently high growth rate.

c. OMVPE/MOVPE is used as a stable metalorganic source of zinc acetylacetonate in combination with oxygen and sapphire substrate in the standard atmospheric pressure. This yields high-quality ZnO films [34]. Otherwise, iso-propanol (i-PrOH), tertiary butanol (t-BuOH), acetone, N_2O and NO_2 may be used as O_2 precursor(s).

2. The earliest ZnO investigations saw sputtering (including direct current sputtering, radio frequency magnetron sputtering and reactive sputtering) as one of the most popular techniques. The structure and the optical properties of the ZnO coatings deposited by using *radio frequency magnetron sputtering (RFMS)* have been one of the major research topics. The structure and properties of films depend on the sputtering variables (the substrate temperature, the radio frequency power, the gas pressure and the composition) and on the substrates (specifically, sapphire, diamond, glass, Si substrates, etc.) that are used for variable device applications [29]. The major advantages of RFMS include the low cost, simplicity, low operating temperature as well as the reasonable quality of the film. In the process of using RFMS, usually the growth is carried out in an ambient of O_2/Ar+O_2 with the ratios ranging from 0 to 1 and the pressure of 10^{-3}–10^{-2} Torr. O_2 is used as the reactive gas while Ar serves as the sputtering enhancement gas. The synthesis temperature ranges from the room temperature to 673 K. Sapphire substrates are the most commonly used type because they possess a similar lattice structure and

are easily available [35]. While using this technique, high-quality ZnO film is obtained. It may thus be used for piezoelectricical devices.

3. When coatings deposited by using *molecular beam epitaxy (MBE)*, thin semiconductor heterostructures are obtained. The main advantage of MBE is the precise control over the growth parameters and *in situ* diagnostic capabilities. The disadvantages of MBE include the high price of the source and the expensiveness of the maintenance as well as the plasma source degradation because of the high reactivity of oxygen radicals, the increasing contamination of the film by source materials because of the sputtering source parts, etc. The typical growth rate is $\leq 1 \mu m h^{-1}$; the most commonly employed source materials include metallic Zn and O_2; the most popular substrates are the a-plane sapphire and GaN templates. For high-quality ZnO films, the growth temperature is in the range of 623–1023 K, and growth rate is in the range of 0.3–0.7 $mm h^{-1}$ [44, 45].

4. The usage of the *sol-gel* technique offers the possibility of preparing a small as well as large-area coating of ZnO thin films at a low cost for technological applications. Its core advantages include simplicity, reliability, repeatability, relatively mild conditions of synthesis and the low cost of the technique. The *sol-gel* synthesis may be performed from a colloidal sol, and a powder from the colloidal sol is transformed into a gel. By using various solvents (ethanol, propan-2-ol, monoethanolamine, etc.) and starting materials ($Zn(CH_3COO)_2 \cdot 2H_2O$, zinc 2-ethylhexanoate, etc.) various structures of ZnO can be obtained. Recently, Yue et al. prepared high-filling uniform ordered ZnO nanotubes into the ultrathin porous anodic aluminum oxide (AAO) membrane. The main advantage – the integration of the ultrathin AAO membranes with the sol-gel technique – may be used as a template for the growth of nanostructures [46].

5. *Hydrothermal synthesis* is a simpler and more environmentally friendly technique because neither organic solvents nor additional processing of the product (grinding and calcination) are used. The advantages of this method are as follows: synthesis is possible at low temperatures, the purity of the obtained material is high, the product is well crystallized with crystals of various shapes and dimensions being obtained (the product depends on the composition of the starting mixture, the temperature and the pressure). The reagents of the synthesis are zinc acetate, zinc acetate dehydrate, nitrate, and chloride, etc. A suitable hydroxide (NaOH, LiOH, KOH, and $NH_3 \cdot H_2O$) may or may not be used. The requirements for the synthesis are as follows: an autoclave or a microwave reactor, the temperature in the range of 373 – 673 K while the duration ranges from 1 hour to several days. When microwave reactors are employed for heating the solutions, the loss of energy required for heating the entire vessel is avoided. Schneider et al. used microwave reactors and obtained ZnO by heating zinc acetylacetonate and a zinc oxime complex in various alkoxyethanols (methoxy-, ethoxy- and butoxyethanol) [47]. It was shown that the morphology and aggregation of ZnO particles strongly depends on the employed precursor.

6. The *electrophoretic deposition (EPD)* is a cost-competitive technique for obtaining highly uniform films with the thickness from ranging within the nanometer-to-micrometer scale by altering the applied voltage and the deposition

time. The main advantages of the EPD method are as follows [48, 49]: it can be applied to any available solid material in the form of fine powder, rapid film deposition, low cost, simple instrumentation, minor restriction on the shape of substrates, good potential for the conservation of materials. EPD has been reported to be a highly beneficial technique for the preparation of nanostructured ZnO films [49-61]. Both aqueous and non-aqueous ZnO suspensions have been used for the coating of various substrates (transparent conductive oxide glass, anodic alumina membranes, steel and nickel). Methanol, ethanol, propanol, isopropyl alcohol, etc. were used as solvents. Chen at el. deposited homogenous and smooth nanostructured ZnO coating on ITO-PEN (plastic substrate) film at room temperature [56]. Such a film is used for the photoanode of a dye-sensitized solar cell.

7. When compared to other methods, *electrochemical deposition (ECD)* has several advantages and is widely used in industry for the surface protection against corrosion and for the synthesis of various catalysts. The most important advantages of ECD are its low cost, the possibility of large-scale operations, the low temperature processing and the direct control over the resulting film thickness [62, 63]. The final morphology and texture of the electrodeposited material depend on the electrolyte composition, temperature, electrode potential or current density as well as on the duration of the electrodeposition process and the nature of the electrode substrate [64]. Very thin layers with specific composition, morphology and good adhesion between the deposited film and the substrate of a complex shape can be prepared by using electrochemical techniques. However, this method of deposition also has several drawbacks: oxide coatings are generally amorphous; therefore they should be additionally thermally treated whereas the obtained coatings are not homogenous, either.

Recently, the importance of several electrochemical methods in the synthesis of various semiconductor nanostructures was reviewed by Wu et al. [63]. Peulon and Lincot were the first to demonstrate that the direct electrodeposition of ZnO films of good quality from aqueous solutions is possible [65]. This work has received great interest; hence intensive research is being carried out in this field.

Conventional electrolyte baths for the electrodeposition of bare zinc oxide films typically contain chlorides, nitrates or, rarely, acetates. The presence of various organic molecules (e.g., glucose, fructose, citric acid, tartrate, polyelectrolytes, etc.) in the electrodeposition bath is known to highly influence the structure, morphology and properties of zinc (hydr)oxide films. Usually, ZnO electrochemical deposition takes place in a three-electrode electrochemical cell: silver chloride or calomel electrode are used as the reference electrode; the counter electrode is a platinum wire or plate, a graphite rod or a zinc plate; the working electrode commonly uses glass plates coated with ITO (SnO_2 doped with In), FTO (SnO_2 doped with F) or, rarely, stainless steel; the deposition conditions are galvanostatic or potentiostatic; specific temperature; various deposition times. ZnO coatings deposited at room or $\leq$ 333 K temperature are unstable whereas low quality though stable and high quality coatings are obtained only at higher (> 333 K) temperatures; especially, annealing at 673 K or 873 K temperatures increases the quality of coatings.

ZnO deposition conditions from various electrolytes:

- *0.1 or 0.05 M $Zn(NO_3)_2$ electrolyte*. ZnO coatings are deposited under potentiostatic (deposition potential -0.9 ÷ -1.2 V, duration time 5 min till 1h, temperature 293 – 353 K) and galvanostatic (current density 1, 5, 10, 20 $mA \cdot cm^{-2}$, temperature 293 – 353 K, duration time 3 min till 4h) conditions [66-72].
- *5 mM $ZnCl_2$ electrolyte*. ZnO coatings are deposited under potentiostatic (deposition potential -0.6 ÷ -1.4 V, duration time 10 min till 1h, temperature 293 – 353 K) and galvanostatic (current density 0.05, 0.1, 0.15, 0.32 $mA \cdot cm^{-2}$, temperature 293 – 353 K, duration time 30 min till 1h) conditions [73-83].
- *0.05 M $Zn(CH_3COO)_2$ electrolyte*. ZnO coatings are deposited under potentiostatic (deposition potential -0.9, -1.0 and -1.1 V, duration time 10 min till 1h, temperature 333 K) conditions [84].

Depending on the obtained electrochemically deposited ZnO structure, such coatings can be used in piezoelectric and optoelectronic devices, energy storage applications, solar cells and functional materials applicable for water photo-splitting, etc.

1.5. Zinc–cobalt oxide films

Oxides have been widely studied due to their good electrocatalytic activity for many electrode reactions such as oxygen evolution, oxygen reduction, hydrogen formation and organic electrosynthesis [15]. Mixed metal oxides have a general formula AB_2O_4, in which the A-site is tetrahedrally coordinated and usually occupied by divalent cations (Mg, Mn, Ni, Zn) whereas the B-site is octahedrally coordinated and occupied by trivalent cations (Al, Cr, Co, Fe). Mixed metal oxides show a novel set of physicochemical properties that are completely changed from those of the individual metal oxides. Particularly, cobalt (hydr)oxide is one of the most promising electroactive materials for high-performance electrochemical capacitors [85]. ZnO is an important n-type semiconducting material possessing a wide band gap (3.37 eV) and is used in various industrial applications, such as catalysts, rubber and concrete additives, photovoltaics, pigments, gas sensors and mixed-oxide varistors [27]. Recent research has been focused on the improvement of ZnO optical, ferromagnetic and catalytic properties by doping 3d transition metal ions into a metal oxide lattice, mixing two or more metal oxides while applying such chemical or physical methods as plasma exchanged (PECVD) [86] chemical vapour deposition (CVD) [87], co-precipitation method [88], atomic layer deposition [89], low-temperature mechanosynthesis [90], low-temperature solid-state pyrolitic reaction [91], template-free one-pot solvothermal reaction [92], spray pyrolysis [93, 94], electrophoretic deposition [95, 96], hydrothermal synthesis [97, 98], liquid ceramic method [99], pulsed laser deposition [100, 101], magnetron sputtering [102, 103], molecular beam epitaxy [104, 105], sol-gel [106, 107] and electrochemical deposition [108-111]. For example, spinel structure $ZnCo_2O_4$ is a promising catalyst for CO and H_2 mixture oxidation. $Zn_xCo_{3-x}O_4$ is a solid solution that, at low temperatures, is an excellent H_2S absorbent [108, 112].

Only a few works, however, are available in the field of the electrodeposition of mixed Zn-Co oxide films. El-Manouni and Tortosa [108] reported the effect of

annealing in the atmospheric air at 673 K on the structural and optical properties of $Zn_{1-x}Co_xO$ thin films ($1\% \leq x \leq 17\%$) grown by cathodic electrodeposition technique on ITO substrate. It was concluded that thermal annealing improves the crystal quality and produces an increase of the intensity of the Co^{2+} related absorption bands thus revealing that a higher amount of Co atoms are occupying Zn sites. Cao et al. [109] performed ferromagnetism analysis of Zn-Co oxide films synthesized while using electrodeposition. After the plasma treatment, the series of Zn-Co oxide samples exhibited ferromagnetism at room temperature, and the origination of ferromagnetism was thought to be due to the mediation through the p-d exchange interactions between holes and Co atoms. Jaramillo and McFarland [110] prepared a library of 120 samples containing 27 different compositions ($0 \leq x \leq 0.068$) of $Zn_{1-x}Co_xO$ films by employing automated serial electrochemical synthesis. They discovered that all the researched films exhibited the wurtzite structure while Co^{2+} was observed to be a substitutional dopant. Its moderate concentrations (~2−5 mol %) led to a large increase in the photocurrent obtained using visible-illumination, with $Zn_{0.956}Co_{0.044}O$ exhibiting four times the photocurrent of pure ZnO. Wang et al. [111] also studied the ferromagnetism of as-prepared Co-doped ZnO films by using electrochemical deposition. The results showed that ZnO had the wurtzite structure when doped up to 5% with cobalt, and the doped samples showed a ferromagnetic behaviour at room temperature. Kim et al. [113] prepared spinel-type $ZnCo_2O_4$ and Co_3O_4 thin films as electrocatalysts for the oxygen evolution reaction (OER). It was determined that $ZnCo_2O_4$ electrodes are stable and can be a more economical and environmentally benign replacement for Co_3O_4 as an OER catalyst.

To the best of our knowledge, there is no scholarly literature data concerning electrochemical deposition of mixed Zn-Co oxides on stainless steel and electroconductive glass substrates obtained while using the acetate electrolysis bath. Stainless steel can serve as a practical scalable substrate that can be manufactured of any shape and size. Our interest in Zn-Co oxide coatings deposition stems from the search for new functional materials suitable for water photo-splitting and energy storage applications. Thus the aim of the present thesis was to synthesize cobalt-zinc oxide coatings on the stainless steel and electroconductive glass substrates with enhanced electrochemical performance and to evaluate the scope of their further use in aqueous electrochemical systems.

2. MATERIALS AND METHODS

2.1. Materials

All reagents used in the experiments were chemically or analytically pure commercial reagents.

2.1.1. Formation of ZnO coatings by electrophoretic deposition

Zinc acetate dihydrate ($Zn(CH_3COO)_2 \cdot 2H_2O$, > 97% purity) obtained from Reachim (Russia) served as the precursor for the synthesis of bare ZnO powder. 0.5 g of the precursor was placed in a porcelain crucible, covered by an aluminum lid, and heat-treated at 673 K for 1 hour in atmospheric air [114].

AISI 304 type stainless steel plates 0.5 mm thick were used as an electroconductive support. According to the manufacturer, the composition of stainless steel is as follows (wt. %): C, 0.08; Cr, 18–20; Ni, 8–10.5; Mn, 2.0; Si, 1.0; P, 0.045; S, 0.03; Fe, the balance.

The suspension for the electrophoretic deposition (EPD) was prepared by dispersing 2 g of the prepared ZnO powder in 100 mL of methanol (CH_3OH, Lachema, Czech Republic, 99.5% purity). A homogenous suspension was achieved under vigorous stirring for 10 min. Two stainless steel plates (5 x 1 cm each) were immersed into the prepared suspension of ZnO. The distance between the anode and the cathode was 2 cm. EPD synthesis was performed under constant voltage (10–40 V) and was controlled using a DC power supply B5-49 (MNIPI Inc., Russia). The deposition time varied in the range of 0.5 – 40 min. The formation of ZnO coatings took place on the cathode. In order to achieve better adhesion of ZnO particles on the stainless steel substrate, all the samples were thermally treated at 673 K for 1 hour in the atmospheric air.

2.1.2. Synthesis of ZnO coatings by electrodeposition

Zinc oxide coatings on stainless steel were prepared by electrochemical deposition under galvanostatic conditions. The synthesis was performed by using 0.05 M $Zn(CH_3COO)_2$ + 0.1 M KNO_3 + 0.001 M HNO_3 electrolyte (initial pH 5.8). In order to form ZnO coatings on the steel substrate, the current density was varied in the range of 0.10 – 1.5 $mA \cdot cm^{-2}$. AISI 304 stainless 0.5 mm thick steel plates were used as a support. Only freshly prepared solutions were used for the synthesis. All the prepared solutions were not deaerated during the experimental runs. The electrochemical deposition was carried out at 293 – 343 K for 2 – 30 min. The as-deposited samples were thoroughly washed with distilled water and dried to the constant weight at room temperature. The prepared samples were thermally treated under the atmospheric air conditions at 673 K for 1 h.

The experiment results showed that the most uniform and stable coatings were prepared under the following experimental conditions: the cathodic current density of 1 $mA \cdot cm^{-2}$, the electrolysis duration of 10 min, and the electrolyte temperature of 343 K.

2.1.3. Electrodeposition of mixed Zn-Co oxide coatings

The coatings (throughout the paper they are denoted as *ZnCoO*) were prepared by using electrochemical deposition under potentiostatic conditions as shown in Table 2.1. AISI 304 type stainless steel (5 x 1 cm each) and TEC 15 glass plates (3.5 x 1 cm each) were used as the working electrode substrates. TEC 15 represents fluorine tin oxide (FTO) coated glass plates with the nominal FTO film thickness of <200 nm. Initially, glass substrates were cleaned for 10 min in acetone, then for 10 s in 0.1 M sodium hydroxide, next, for 10 s in concentrated sulphuric acid and finally rinsed in distilled water following the procedure described in [113]. Zinc acetate ($Zn(CH_3COO)_2 \cdot 2H_2O$, > 97% purity), cobalt acetate ($Co(CH_3COO)_2 \cdot 4H_2O$, 97% purity) and potassium nitrate (KNO_3, > 99% purity) were obtained from Reachim (Russia) and used as received. Only freshly prepared solutions were used for the synthesis. Solutions were not deaerated during the experimental runs. The electrochemical deposition was carried out at 293 or 343 K temperature under slow stirring. The electrolysis time was varied in the range of 1 – 20 min.

The as-deposited samples were thoroughly washed with distilled water and dried to the constant weight at room temperature. The as-prepared samples were thermally treated under the atmospheric air at 673 K for 1 h. In addition, the coatings of bare zinc oxide and cobalt hydroxide were electrodeposited on AISI 304 stainless steel and TEC 15 glass under similar experimental conditions (Table 2.1), except for the electrolysis potential for $Co(OH)_2$ deposition. The most stable $Co(OH)_2$ coatings were found to be formed at –0.9 V.

Table 2.1. Composition of electrolyte bath used for the synthesis of mixed Zn-Co oxide coatings at –1.15 V

Sample notation	Concentration of electrolyte bath components, M			pH
	$Zn(CH_3COO)_2$	$Co(CH_3COO)_2$	KNO_3	
ZnCoO1	0.04	0.01	0.1	6.6
ZnCoO2	0.03	0.02		6.6
ZnCoO3	0.02	0.03		6.7
ZnCoO4	0.01	0.04		6.7
ZnO	0.05	-		6.4
$Co(OH)_2$[a]	-	0.05		7.2

[a] electrodeposition potential –0.9 V

2.2. Analytical techniques

2.2.1. Structural characterization

2.2.1.1. Differential scanning calorimetry and thermogravimetry (DSC–TG) analysis was performed on a *Netzsch STA 409 PC Luxx* (Netzsch GmbH, Germany) simultaneous thermal analyzer. Analytical parameters: the rate of temperature increase was $15° \cdot min^{-1}$; the temperature range was set at 303 – 773 K; blank Pt / Rh crucible was used; the heating was carried out in the atmospheric air.

2.2.1.2. Fourier transform infrared (FT-IR) spectra were obtained on a *Perkin Elmer FT-IR Spectrum X System* while using KBr pellets. 1 mg of the substance was mixed with 200 mg of KBr, and these pellets were pressed in vacuum environment. The scanning range was 400–4000 cm^{-1} whereas the resolution was 1 cm^{-1}.

2.2.1.3. Micro-Raman spectroscopy was performed with *Raman Nicolet Almega XR Spectrometer*, Thermo Scientific. A 532 nm laser (10 mW power, 0.6 µm spot size, 15 seconds scan time with 4 scans per point) and a CCD detector were used.

2.2.1.4. Scanning electron microscopy (SEM) images for the coatings on AISI 304 stainless steel were acquired by using the *Hitachi S-4800* scanning electron microscope (Hitachi High Technologies America Inc., Schaumberg) equipped with a cold field emitter operating at 2 kV accelerating voltage and a working distance of 10 mm. Samples were imaged without any conductive coating. No specific sample preparation was performed before imaging.

The surface morphology and the composition of coatings on TEC 15 glass and ZnO powder were investigated with a *Qanta FEG 200* (FEI) high resolution scanning electron microscope (SEM). The images were obtained at 20 – 30 kV, the pressure in the chamber was set at 80 Pa, up to ×150 000 magnification was employed depending on the sample. The samples were imaged without any conductive coating. SEM was equipped with *Bruker XFlash® 4030* detector (Bruker AXS) for high resolution energy dispersive X-ray spectroscopy (EDX).

2.2.1.5. X-ray powder diffraction (XRD) data were collected with *DRON-6* (Bourevestnik Inc., Russia) powder diffractometer equipped with Bragg-Brentano geometry and using Ni-filtered CuK_α radiation and graphite monochromator for coatings deposited on AISI 304 steel. For the thin coatings deposited on TEC 15 glass, XRD analysis was performed on a *D8 Advance* diffractometer (Bruker AXS GmbH, Karlsruhe, Germany) operating at the tube voltage of 40 kV and the tube current of 40 mA. Freshly prepared samples were mounted on low background quartz sample holders. The X-ray beam was filtered with a Ni 0.02 mm filter in order to select the CuK_α wavelength. Diffraction patterns were recorded in a Bragg-Brentano geometry by using a fast counting detector Bruker LynxEye based on the silicon strip technology. The specimens were scanned over the range $2\theta = 3 – 70°$ at a scanning speed of $6° \cdot min^{-1}$ by using the coupled two theta/theta scan type. The crystallite size D_{hkl} was calculated from the line broadening using the Scherrer's equation [115]:

$$D_{hkl} = \frac{k \cdot \lambda}{B_{hkl} \cdot \cos\theta}; \qquad (2.1)$$

where λ is the wavelength of the CuK_α radiation ($1.54056 \cdot 10^{-10}$ m), θ is Bragg diffraction angle, B_{hkl} is the full width at the half-maximum intensity of the characteristic reflection peak ($2\theta = 31.66^o$, 34.38^o, 36.26^o for ZnO while $2\theta = 36.86^o$ for Co_3O_4). k here is the constant (the value of 0.94 was used in this study).

2.2.1.6. A custom-designed *Kratos Axis Ultra X-ray photoelectron spectroscopy (XPS)* system was used to determine the elemental composition of the obtained coatings. As it outlined in [116]: the surface analysis chamber was

equipped with monochromatic radiation at 1486.6 eV from an aluminum K_α source using a 500 mm Rowland circle silicon single crystal monochromator. The X-ray gun was operated by using a 15 mA emission current at an accelerating voltage of 15 kV. Low energy electrons were used for charge compensation to neutralize the sample. Survey scans were collected by employing the following instrument parameters: the energy scan range of 1200 to −5 eV; the pass energy of 160 eV; the step size of 1 eV; the dwell time of 200 ms and the X-ray spot size of 700 · 300 μm. High resolution spectra were acquired in the region of interest by using the following experimental parameters: the 20-to-40 eV energy window; the pass energy of 20 eV; the step size of 0.1 eV and the dwell time of 1000 ms. One sweep mode was used to acquire all the regions. The absolute energy scale was calibrated to the Cu $2p_{2/3}$ peak binding energy of 932.6 eV by using an etched copper plate. All the spectra were calibrated by using C1s peak at 285.0 eV. A Shirley-type background was subtracted from each spectrum to account for inelastically scattered electrons contributing to the broad background. CasaXPS software was employed for processing the XPS data. Transmission corrected relative sensitivity factor (RSF) values from the Kratos library were used for elemental quantification. An error margin of ±0.2 eV is reported for all the peak binding energies.

2.2.1.7. The reflectance spectra of the samples were recorded on a *Lambda 35* UV–Vis spectrophotometer (Perkin Elmer Instruments Co. Ltd., USA) equipped with a 50-mm machined Spectralon® integrating sphere. A $BaSO_4$ disc was employed as a reference, i.e. as a white standard. The scan ranged from 200 to 800 nm. Optical band-gaps were calculated from the reflectance spectra by using the relation [117]:

$$E_g = \frac{1.24}{\lambda}; \qquad (2.2)$$

where E_g is the band-gap energy in eV, and λ is the absorption edge in μm.

2.2.1.8. Atomic absorption spectroscopy (AAS) analysis was performed with a *Perkin Elmer 403* spectrometer. The radiation source was a hollow cathode lamp. The atomization was carried out in a flame by using the acetylene-air mixture. The coatings were scraped and dissolved in 50 mL of 0.1 M HNO_3. The content of zinc and cobalt in the coatings was determined by measuring the absorption at 213.86 and 240.73 nm, respectively.

The pH was measured by using a *673 M* pH meter.

2.2.2. Photoelectrochemical techniques

2.2.2.1. The electrochemical measurements were performed by computer-controlled *Autolab PGSTAT12* (Ecochemie, The Netherlands) potentiostat/galvanostat using a standard three electrode cell (volume 100 mL). The GPES® 4.9 software was used for the collection and treatment of the experimental data. All the potentials are referred to the Ag, $AgCl \mid KCl_{(sat)}$ reference electrode. Throughout the thesis, all the potentials are referred to this electrode. The cathodic compartment housed a platinum wire (geometric area about 15 cm^2) as a counter electrode. The working electrode was AISI 304 stainless steel or electrically conductive glass TEC 15.

2.2.2.2. *The photoelectrochemical activity* of the prepared electrodes was investigated by employing photovoltammetry measurement methods. A photoelectrochemical quartz cell was employed (Fig. 2.1). 0.1 M Na_2SO_4 (> 99%, Reachim, Russia), 0.1 M NaOH (> 98%, Reachim, Russia) or phosphate buffer solutions were used as the supporting electrolytes. A phosphate buffer of pH 7 was prepared by using the following procedure: 61.5 ml of K_2HPO_4 (> 98 %, Reachim, Russia) and 38.5 ml KH_2PO_4 (> 98 %, Reachim, Russia) of 1 M stock solutions were combined and then diluted to obtain 1 litre solution; distilled water was added. A phosphate buffer of pH 11.5 was prepared by using the following procedure: 100 ml of 0.05 M K_2HPO_4 (> 98 %, Reachim, Russia) and 22.2 ml 0.1 M NaOH (> 98 %, Reachim, Russia) stock solutions were combined and then diluted to 200 mL with the addition of distilled water. Solutions were not stirred during all the photoelectrochemical activity measurements.

In the case of the stainless steel substrate, the back side of the working electrode was insulated with epoxy resin in order to eliminate its contribution to the dark current. The coated area of the electrode was carefully positioned in the path of the UV irradiation. A General Electric *F8W/BLB* lamp (λ_{max} = 366 nm, the average power density being 1.8 mW·cm^{-2} [118]) was placed at a distance of 2 cm from the working electrode and was used as an UV radiation source.

The incident photon-to-current efficiency (IPCE) value of the photoelectrode was calculated by using the following relation [119]:

$$\mathrm{IPCE}(\%) = 100\frac{1240 \cdot j_{ph}}{\lambda \cdot P}, \tag{2.3}$$

where j_{ph} is the photocurrent density in mA·cm^{-2}, λ is the wavelength of the incident light in nanometers (the value used in this study was 366 nm), and P is the incident light intensity in mW·cm^{-2}.

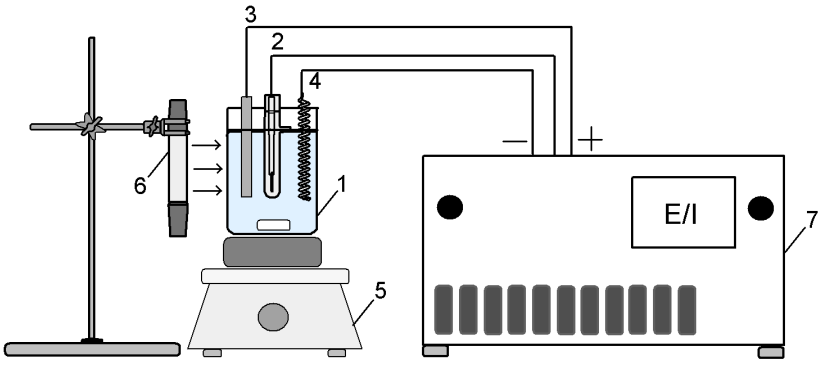

Fig. 2.1. Experimental set-up for photoelectrochemical measurements:
1– photoelectrochemical quartz cell; 2 – reference electrode; 3 – working electrode; 4 – platinum wire as a counter electrode; 5 – electromagnetic stirrer; 6 – UV irradiation lamp; 7 – potentiostat/galvanostat

2.2.2.3. *Photochemical deposition of Co-P_i catalyst*. Experimental runs were performed by using the photochemical reactor shown in Figure 2.2. The prepared photoanode (ZnO on stainless steel) was immersed in 50 mL of mixture containing 0.1 M phosphate buffer (pH 7) and 0.5 mM cobalt nitrate ($Co(NO_3)_2 \cdot 6H_2O$, > 99 %, Chempur, Poland). The mixture was vigorously stirred at 298 K and was irradiated with a 400 W *HPA 400/30S* (Philips, The Netherlands) high pressure metal halogen lamp up to 40 min. The lamp was held at 2 cm from the reactor. An emission spectrum of this lamp is characterized by its high radiation intensities in the 300 – 400 nm wavelength range (the maximum intensity of the lamp radiation is $9.03 \cdot 10^{18}$ photons$\cdot s^{-1}$) [118].

The photocurrent of the coatings modified with Co-Pi were measured in a three-electrode setup (Fig. 2.2) by using 0.1 M potassium phosphate electrolyte (pH 11.5). A pH 11.5 medium was chosen because the ZnO electrode is chemically and photochemically the most stable at pH ~12 [16].

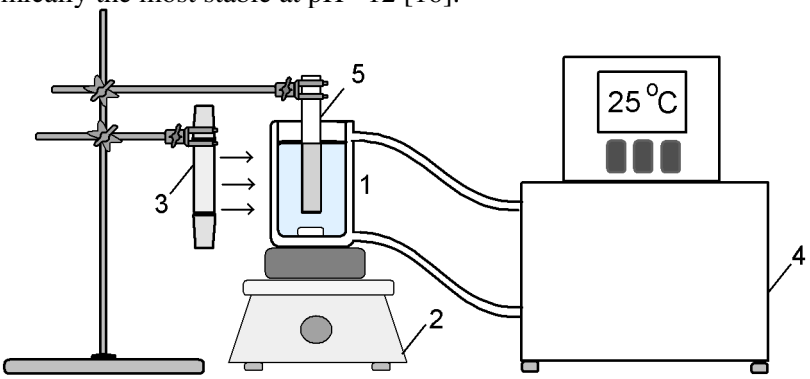

Fig. 2.2. Scheme of the photochemical reactor: 1 – quartz cell (thermostated); 2 – electromagnetic stirrer; 3 – UV lamp; 4 – thermostat; 5 – ZnO coating on steel

2.2.2.4. *Pseudocapacity measurements.* To evaluate the specific capacitance of the coatings, all the cyclic scans were repeated at least ten times. The anodic charge value of the 10th cycle was used in calculations. The capacitive behaviour of the electrodes was estimated by referring to the cyclic voltammetry (CV). 0.1 M NaOH solution was used as a supporting electrolyte. The specific capacitance (C) based on CV was calculated as follows [120]:

$$C = \frac{Q}{\Delta E \cdot m}; \qquad (2.4)$$

where Q is the anodic charge in coulombs, ΔE is the potential range in volts and m is the mass of the active material measured in grams.

2.2.3. Statistical analysis of experimental data

The processing of the experimental data was performed by Microsoft® Excel 2010 and OriginLab Corporation® OriginPro 8.5 software.

3. RESULTS AND DISCUSSION

3.1. Structure and photoelectrochemical activity of ZnO coatings on stainless steel

The research of scholarly writings showed that the nature of the starting material and synthesis conditions are important for the ZnO photocatalyst activity. Depending on the ZnO treatment conditions the coatings of various structures, morphology, composition and photoactivity may be obtained. To the best of our knowledge, there is no published data concerning the electrophoretic deposition of ZnO on the stainless steel substrate when using thermally decomposed zinc acetate dehydrate. Due to the reasons outlined above, the initial stage of the thesis was to prepare ZnO coatings on stainless steel by using the EPD method and to determine their photoelectrochemical activity in aqueous solution(s).

3.1.1. ZnO coatings prepared by electrophoretic deposition

3.1.1.1. Structural characterization

The synthesis of bare ZnO powder was carried out according to the procedure described in Section 2.2.1. Thermogravimetric (TG) and differential scanning calorimetry (DSC) analyses were performed in order to determine the thermal effects during the decomposition of zinc acetate in the atmospheric air (Fig. 3.1).

The first mass loss of 14.19 % prior to reaching the temperature of up to 400 K was accompanied by an endothermic peak at 373 K. This corresponds to the theoretical value of the thermal dehydration of two water molecules (16.41%) [114, 121]:

$$Zn(CH_3COO)_2 \cdot 2H_2O\ (s) \rightarrow Zn(CH_3COO)_2\ (s) + 2H_2O\ (g).$$

After dehydration, the mass loss was 43.15 % and it can be assigned to the decomposition of anhydrous $Zn(CH_3COO)_2$ into ZnO. The endothermic peak value at 519 K is close to the melting point of anhydrous zinc acetate and has a shoulder at 527 K. Consequently, it is suggested [114] that two different compounds coexisted in the specimen when heated at rapid heating rate conditions. During the decomposition of zinc acetate, anhydrous zinc acetate is believed to oligomerize on sublimation and to form basic zinc acetate, $ZnO_4(CH_3COO)_6$, which is a favourable precursor for the formation of ZnO coatings [114, 121]:

$$4Zn(CH_3COO)_2\ (s) \rightarrow Zn_4O(CH_3COO)_6\ (s) + (CH_3CO)_2O\ (g);$$

$$Zn_4O(CH_3COO)_6\ (s) \rightarrow 4\ ZnO\ (s) + 3\ CH_3COCH_3\ (g) + 3\ CO_2\ (g).$$

The total mass loss reaches 57.34 %, and ZnO was found to be the main residue.

The DSC curve indicated one exothermic peak at 620 K with a shoulder at 585 K; thus it may be related to the removal of residual organics (acetate, CO_2) [114, 121].

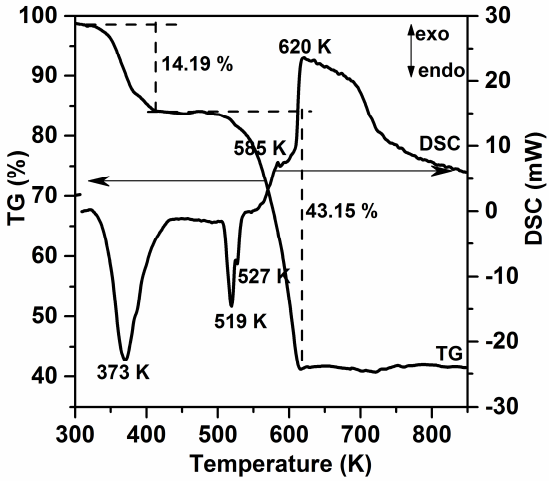

Fig. 3.1. TG-DSC pattern of zinc acetate

XRD analysis reveals the diffraction peaks at 2θ = 31.78°, 34.44° and 36.24° (Fig. 3.2) which correspond to the well-crystallized wurtzite-type ZnO (PDF 04-004-4120). According to the Scherrer's equation (2.1), the average ZnO crystallite size was calculated to be 35.3 nm.

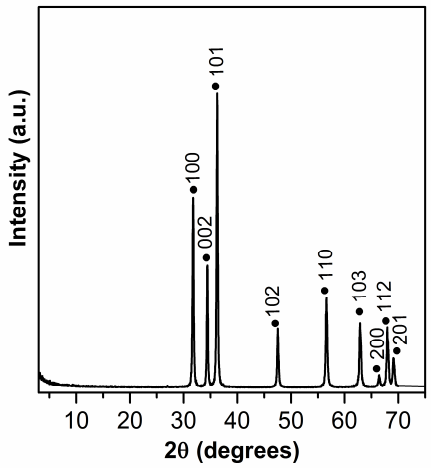

Fig. 3.2. XRD pattern of ZnO obtained by thermal decomposition of zinc acetate dihydrate at 673 K

ZnO powder was also investigated by infrared absorption analysis (Figure 3.3). The large absorption band centered at 3447 cm^{-1} can be assigned to the stretches of hydroxy groups. The peaks observed at 2945, 2355, 1589, 1340 can be attributed to the impurities derived from the industrial production of zinc acetate dihydrate. The peak observed at 2945 cm^{-1} represents the C–H bond thus indicating aliphatic hydrocarbon asymmetrical stretching [122]. The other distinct peak at the wave number of 2355 cm^{-1} indicates –COO. 1589 cm^{-1} can be attributed to the

asymmetrical stretching vibrations of the acetate ions and is associated with the C=O bond. Other peaks at 1340 cm^{-1} show the presence of CH_3 groups [123]. The band at 880 cm^{-1} corresponds to the carbonate ion vibration. A broad band centered at 495 cm^{-1} corresponds to the characteristic stretching of the Zn–O bond, and it can be used for the identification of zinc (white pigment) in the IR spectra of real paint sample layers [124].

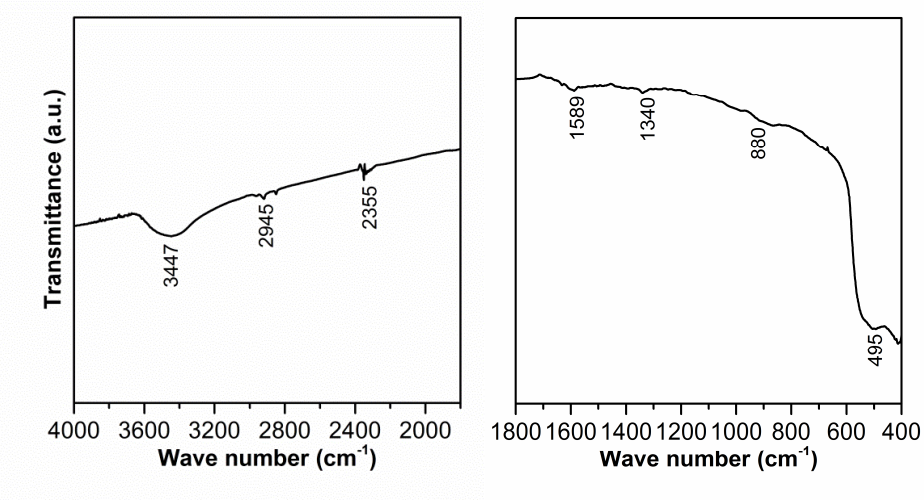

Fig. 3.3. FT-IR spectrum of ZnO obtained by thermal decomposition of zinc acetate dihydrate at 673 K

Figure 3.4 presents the morphological characteristics of the prepared ZnO powder. It is seen that the flower-like structure is formed, which consists of a variety of building blocks, mainly rods. These results are in agreement with those presented in [114].

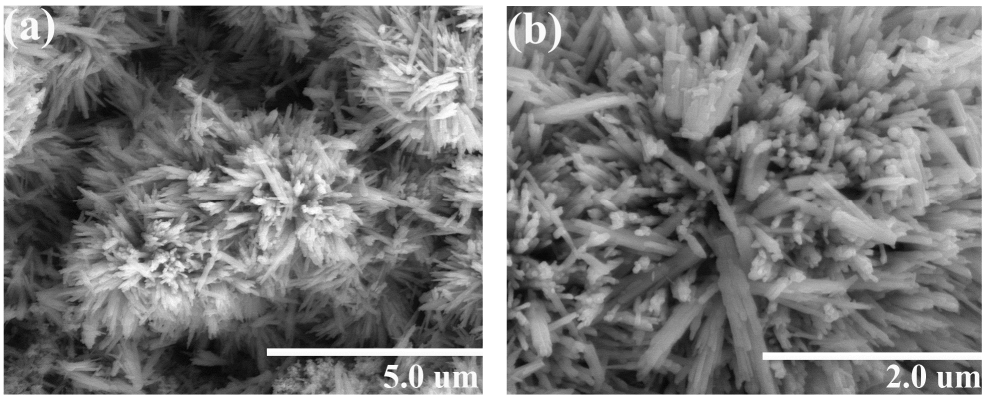

Fig. 3.4. SEM images of ZnO obtained by thermal decomposition of zinc acetate dihydrate at 673 K at various magnifications: (a) × 20 000, (b) × 50 000

The formation of ZnO coatings on AISI 304 type stainless steel substrate was implemented by electrophoretic deposition according to the procedure outlined in Section 2.1.1. The preliminary experimental runs revealed that the most uniform and

stable ZnO coatings are obtained when the applied potential between electrodes is 30 V. Figure 3.5 shows the experimental results of the deposited ZnO weight as a function of electrophoresis time. It is prominent that the amount of the deposited ZnO increases almost linearly with the increase in deposition time. Moreover, it was observed that the rate of ZnO deposit formation increases together with the increase in the applied voltage. However, it is well documented [125] that the quick formation of particulate coatings on the electrode can result in poorer deposit quality as the accumulation rate of the particles greatly influences their packing behaviour in coatings.

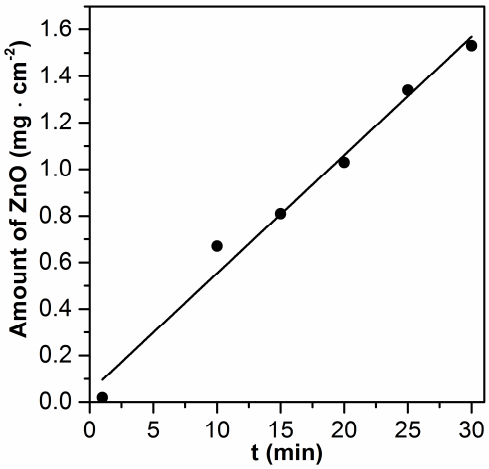

Fig. 3.5. The amount of immobilized ZnO as a function of electrophoretic deposition time *t*

3.1.1.2. Photoelectrochemical characterization of ZnO coatings

Photocatalytic measurements were carried out by using the experimental set-up showed in Figure 2.1. The photoelectrochemical behavior of ZnO electrode (30V, deposition time 20 min) was determined from the current-potential curves obtained in 0.1 M Na_2SO_4 solutions both in the dark and under UV irradiation (Fig. 3.6). The potential was swept from –0.3 V to + 1.0 V at 10 $mV \cdot s^{-1}$. It is evident that the UV irradiation caused a significant increase in the observed current. Such a behaviour is characteristic of *n-type* semiconducting materials and is related to photogenerated electron diffusion through the catalyst coating towards the cathode [126]. The observed anodic photocurrent can be related to the generation of hydroxyl radicals ($HO^{\bullet}$) and other oxidation products (e. g., H_2O_2) at the surface of the ZnO electrode. The presence of $HO^{\bullet}$ radicals at the interface of the ZnO/aqueous solution was confirmed with the help of the radical-trapping technique. Hydrogen peroxide is formed as a result of the interaction of generated hydroxyl radicals [127]:

$$ZnO + h\nu \rightarrow e^- + h^+ \quad (3.1)$$

$$h^+ + HO^- \rightarrow HO^{\bullet} \quad (3.2)$$

$$h^+ + H_2O \rightarrow H^+ + HO^\bullet \quad (3.3)$$

$$e^- + O^2 \rightarrow O_2^{\bullet -} \quad (3.4)$$

$$O_2^- + H^+ \rightarrow HO_2^\bullet \quad (3.5)$$

$$2\ HO_2^\bullet \rightarrow O_2^{\bullet -} + H_2O_2 \quad (3.6)$$

$$H_2O_2 + O_2^{\bullet -} \rightarrow HO^\bullet + HO^- + O_2 \quad (3.7)$$

The rate of hydrogen peroxide formation in aerated ZnO aqueous suspensions is highly dependent on the presence of various organic and inorganic species [127]. It should be emphasized that at the same time the photodissolution (photocorrosion) of ZnO takes place to some extent due to the self-oxidation through photohole generation [128].

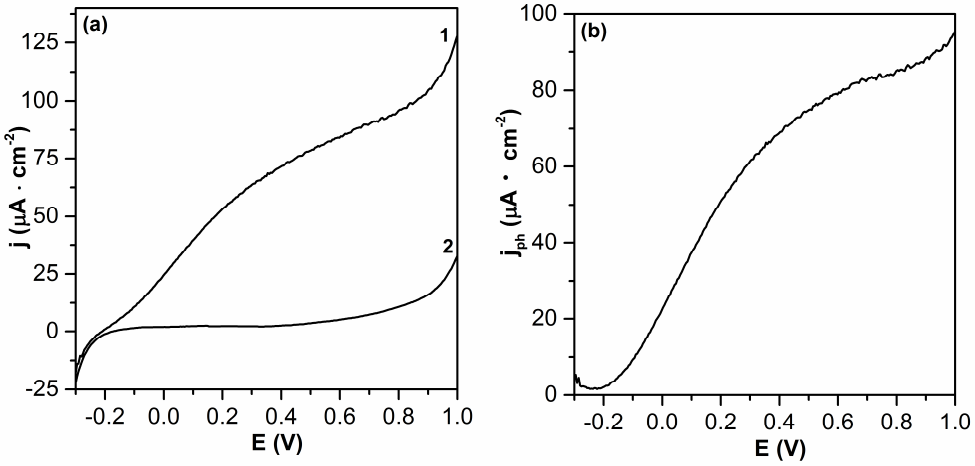

Fig. 3.6. (a) characteristic voltammograms in the dark (2) and under UV illumination (1) of the ZnO electrode. The potential scan rate v = 10 mV·s^{-1}, 0.1 M Na_2SO_4; the supporting electrolyte at 291 K. (b) plot of the photocurrent density, j_{ph}, with respect to the applied potential, E

The time dependence of the electrode potential and the current density in the dark and under UV irradiation for the ZnO electrode is presented in Figure 3.7. When the light was switched on, the observed potential jumped to –0.24 V. The observed decrease in the potential can be explained by the fact that the photoholes react rapidly with water molecules while the photoelectrons accumulate on the surface of ZnO particles and charge them negatively. Under UV irradiation, the observed current jumped to about 87 μA · cm^{-2} (Fig. 3.7 b). When the light was switched off, the current of the ZnO electrode decreased and equalled its initial value.

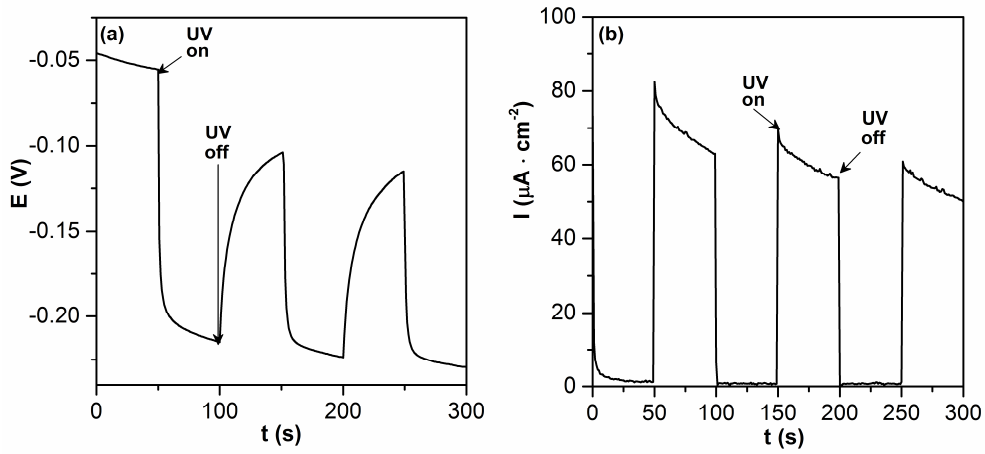

Fig. 3.7. Variation of the open circuit potential (a) and the current density at +0.6 V (b) for ZnO electrode in 0.1 M Na_2SO_4 solution in the dark and under UV illumination

The results presented in Table 3.1 confirmed that the photoelectrochemical activity of the prepared electrodes is dependent on the amount of immobilized ZnO. The incident photon-to-current efficiency (IPCE) value of a photoelectrode was evaluated by using equation 2.3. Photocurrent densities are calculated for the +0.6 V potential because at higher potential values the current increase may be associated with stainless steel dissolution and oxygen evolution [129].

The obtained results show that the 1.03 mg·cm^{-2} loading of ZnO gives the largest photocurrent and, consequently, the highest IPCE value. At a higher ZnO loading the photocurrent tends to decrease. Such dependence is a result of the interplay of various parameters, for instance, the intensity of incident irradiation and the interconnection of ZnO particles in the coating. It is known [130] that there is an optimal layer of thickness if the potentially highest IPCE values are required to be reached. At higher oxide loadings, only the part of the semiconductor layer can be efficiently irradiated with UV light. It means that the nonactive layers of the semiconductor can exist near the surface of the electrode. This layer can act as a recombination zone for the photogenerated charge carriers.

It should be pointed out that in this thesis efforts were made in order to optimize the thickness of the ZnO coatings in terms of their photoactivity. It was discovered that the highest photocurrent (up to 100 μA·cm^{-2}) can be generated in a case of thin coatings (~0.18 μm). However, the formation of very thin uniform and reproducible coatings when using electrophoretic deposition presents some technical difficulties. In addition, electrochemical measurements revealed that the photostability of such ZnO coatings is rather poor. For these reasons, the next step of this work was the synthesis of ZnO coatings by using electrochemical deposition.

Table 3.1. Influence of the amount of ZnO on the photoelectrochemical activity of the prepared electrodes

Deposition time, min	Amount of the deposited ZnO, mg·cm^{-2}	Average thickness of the ZnO layer, μm	Photocurrent density j_{ph} at + 0.6 V, μA·cm^{-2}	IPCE, %
10	0.77	0.41	41.5	7.8
15	0.81	0.45	43.0	8.1
20	1.03	0.57	77.9	14.6
25	1.34	0.70	43.1	8.1
30	1.53	0.82	46.4	8.7

3.1.2. ZnO coatings prepared by electrodeposition

3.1.2.1. Voltammetric behaviour of stainless steel in zinc(II) acetate electrolyte

ZnO thin coatings were synthesized according to the procedure outlined in Section 2.1.2.

The voltammetric behaviour of AISI 304 type stainless steel electrode in 0.05 M $Zn(CH_3COO)_2$, 0.1 M KNO_3 and 0.001 M HNO_3 electrolyte is shown in Figure 3.8. Sweeping negatively from an initial potential of –0.28 V, a reductive peak (labelled C_1) is observed.

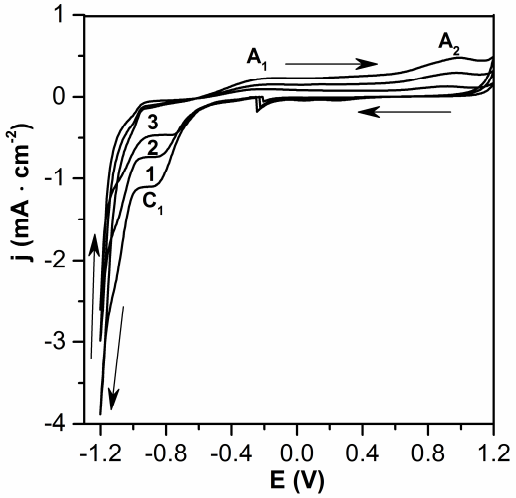

Fig. 3.8. Voltammetric behaviour of AISI 304 type steel in 0.05 M $Zn(CH_3COO)_2$ + 0.1 M KNO_3 + 0.001 M HNO_3 electrolyte at 293 K and various potential scan rates (mV·s^{-1}): 1 – 50; 2 – 25; 3 – 10

The increase in the cathodic current was observed at a negative potential of – 0.65 V. This peak can be related to the reduction of nitrate ions and the formation of hydroxide ions [64]:

$$NO_3^-(aq) + H_2O(l) + 2e^- \rightarrow NO_2^-(aq) + 2OH^-(aq)\ ; \qquad (3.8)$$

A further increase in the observed currents at a negative potential of –0.98 V can be mainly associated with water decomposition releasing molecular hydrogen and hydroxide ions:

$$2H_2O(l) + 2e^- \rightarrow H_2(g) + 2OH^-(aq); \quad (3.9)$$

As a result of these processes, the pH of the electrolyte close to the electrode increases. In addition, a part of the ions can be supplied through hydrolysis as follows [131]:

$$CH_3COO^-(aq) + H_2O(l) \rightarrow CH_3COOH(l) + OH^-(aq); \quad (3.10)$$

Hydroxide ions formed via electrochemical reduction are expected to react with Zn(II) ions present in the electrolyte. Thus zinc oxide gets deposited on the electrodes according to the reaction (3.1):

$$Zn^{2+}(aq) + 2OH^-(aq) \rightarrow Zn(OH)_2(s) \rightarrow ZnO(s) + H_2O(l); \quad (3.11)$$

This is a highly generalized mechanism of cathodic electrodeposition of ZnO coatings while using nitrate solutions. Other processes – such as the deposition of metallic zinc – can take place and play an important role in the nucleation [132-134].

It can be assumed that zinc oxide electrodeposition in the nitrate bath follows an EC (electrochemical reaction followed by an irreversible chemical reaction) mechanism. As stated in [64], the relative importance of (3.8) and (3.9) reactions in the electrogeneration of a base is not well-established. Some experimental evidence shows that hydrogen evolution reactions are as important as nitrate reduction reactions in the process of electrodeposition of (hydro)oxides [64].

When the potential was reversed at –1.2 V and scanned towards the positive values, an increase of the anodic current was observed at the potentials above –0.3 V

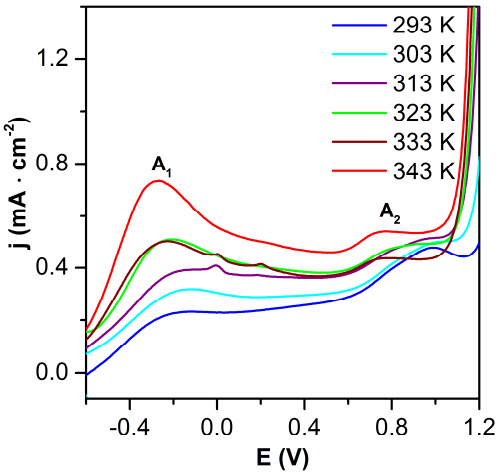

Fig. 3.9. Voltammetric behaviour of AISI 304 type steel electrode in 0.05 M $Zn(CH_3COO)_2$ + 0.1 M KNO_3 + 0.001 M HNO_3 electrolyte at 50 $mV \cdot s^{-1}$ scan rate and various temperatures

It was observed that the peak A_1 increases with an increase of electrolyte temperature (Figure 3.9) and this can be mainly associated with the oxidation of unidentified electrodeposited compounds.

The increase of the anodic current at the potentials above 0.8 V (A_2 peak) can be related to the evolution of oxygen and the oxidation of the stainless steel substrate. It was shown [129] that the transpassive dissolution of stainless steel occurs due to the release of soluble Cr(VI) and Fe(III) species into the electrolyte.

In order to form zinc oxide coatings, the galvanostatic method was used. The current density of electrodeposition was varied in the range of 0.10 – 1.5 mA·cm^{-2} and the duration of electrolysis from 2 to 30 min. The characteristic chronopotentiograms are shown in Figure 3.10. It is evident that ZnO nucleation time decreases with the increase in the current density. The minimum time for ZnO nucleation is when the current density is 1 mA·cm^{-2}; therefore, the ZnO layer on the electrode is deposited faster and becomes more even. The ZnO coatings deposited at higher current densities are thicker, uneven and they peel off.

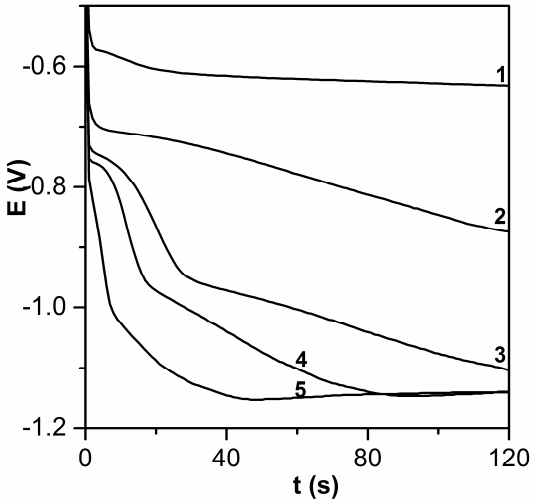

Fig. 3.10. Voltammetric chronopotentiograms at 343 K and different current densities (mA·cm^{-2}): 1 – 0.10; 2 – 0.25; 3 – 0.50; 4 – 0.75; 5 – 1

Preliminary electrolysis experiments revealed that the most stable coatings are obtained at 1 mA·cm^{-2}. At higher current densities, the rapid thickening and flaking of the deposits was observed. Thus during the following experiments we used the zinc oxide electrode prepared under the experimentally determined optimal conditions: the cathodic current density set at 1 mA·cm^{-2}, the electrolysis duration of 10 min, the electrolyte temperature of 343 K, the amount of the coating of 0.4 mg·cm^{-2}, and the layer thickness equalling 0.7 μm.

The electrolyte temperature influence on the ZnO coating deposition process is shown in Figure 3.11. The experimental data clearly shows that the deposition is highly accelerated upon the increase in the electrolyte temperature.

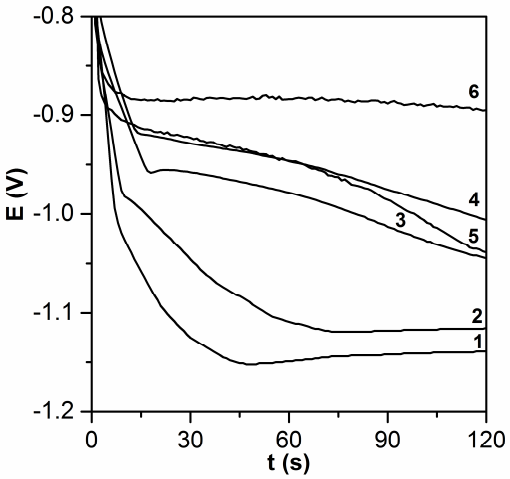

Fig. 3. 11. Voltammetric chronopotentiograms at 1 mA·cm^{-2} current density and various temperatures (K): 1 – 293; 2 – 303; 3 – 313; 4 – 323; 5 – 333; 6 – 343

3.1.2.2. Structural characterization

XRD analysis of samples deposited at 343 K showed three peaks at 2θ = 31.66, 34.38 and 36.26° thus suggesting the crystalline ZnO structure (Fig. 3.12). The strong low-angle reflection peak at 2θ≈7° can be associated with the acetate group (PDF 00-056-0569) intercalated into zinc oxide structure.

After the heat-treatment at 673 K for 1 h, the XRD analysis reveals diffraction peaks corresponding to the well-crystallized ZnO. According to the Scherrer's equation (2.1), the average ZnO crystallite size was calculated to be 29 nm.

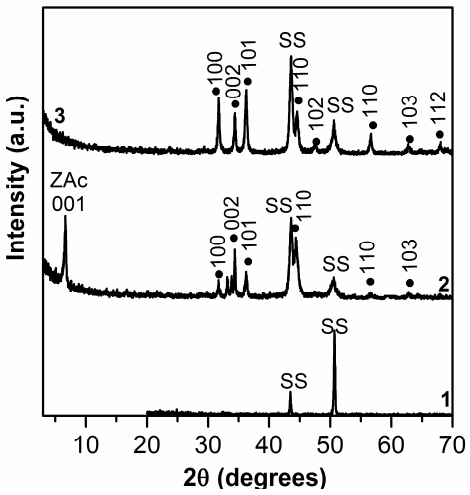

Fig. 3.12. XRD pattern of AISI 304 stainless steel (1), as-deposited (2) and heat-treated at 673 K (3) ZnO electrode. Abbreviations:
SS – stainless steel, ZAc – $Zn(CH_3COO)_2$, ●– ZnO

SEM images of as-deposited and heat-treated zinc oxide coatings are shown in Fig. 3.13. The as-deposited (Fig. 3.13 a) ZnO coating is lamellar.

It is evident that the annealing at 673 K for 1 h considerably changes the surface structure to granular (Fig. 3.13 b). The diameters of grains are between 30 nm and 110 nm.

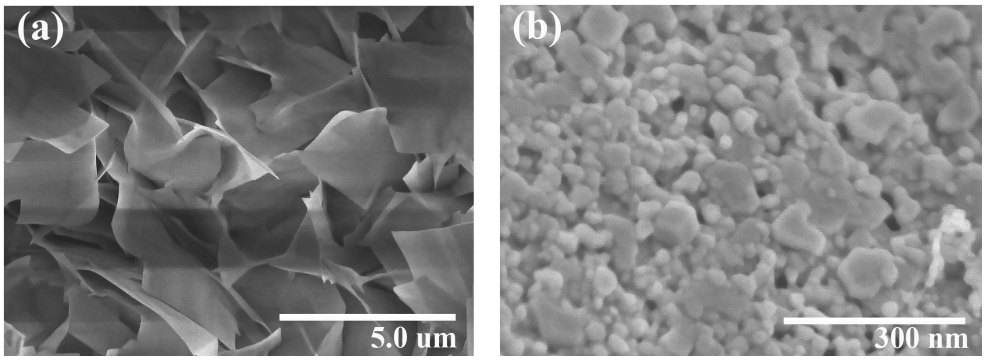

Fig. 3.13. Representative SEM images of as-deposited (a) and heat-treated at 673 K (b) ZnO coatings

The incorporation of acetate ions into as-prepared zinc oxide coatings is confirmed by infrared absorption analysis as well (Fig. 3.14.). It demonstrates the IR absorption not only in the low (600–400 cm^{-1}) wave number region as it would be expected for pure ZnO [131] but also in the intermediate (1600–800 cm^{-1}) and high (3300–3700 cm^{-1}) wave number region as well due to vibrations of impurity ions. The large absorption band centered at 3476 cm^{-1} can be assigned to the stretches of hydroxy groups.

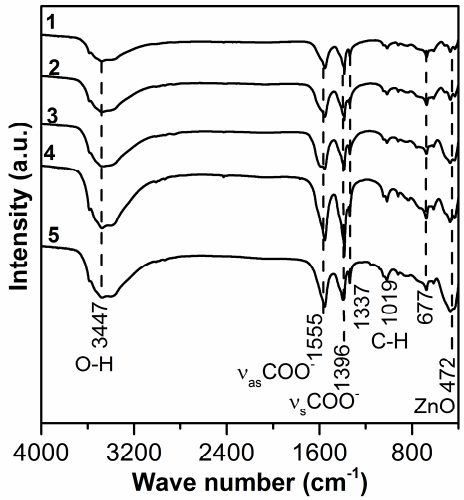

Fig. 3.14. FT-IR spectra of as-deposited ZnO obtained using 0.05 M $Zn(CH_3COO)_2$ + 0.1 M KNO_3 + 0.001 M HNO_3 electrolyte at various electrochemical deposition temperatures (K): 1 – 303, 2 – 313, 3 – 323, 4 – 333, 5 – 343

The peaks observed at 1555 cm^{-1} and 1396 cm^{-1} can be attributed to the asymmetrical and symmetrical stretching vibrations of the acetate ions, respectively. Other peaks at 1337, 1019 and 677 cm^{-1} show the presence of CH_3 groups [123]. A broad band centered at 472 cm^{-1} corresponds to the characteristic stretching frequency of the Zn–O bond and it can be used for the identification of the zinc white pigment in the IR spectra of real paint sample layers [124]. The obtained experimental results show that this characteristic band becomes more intense with the increase in the heat-treatment temperature of the as-deposited sample (Fig. 3.15.).

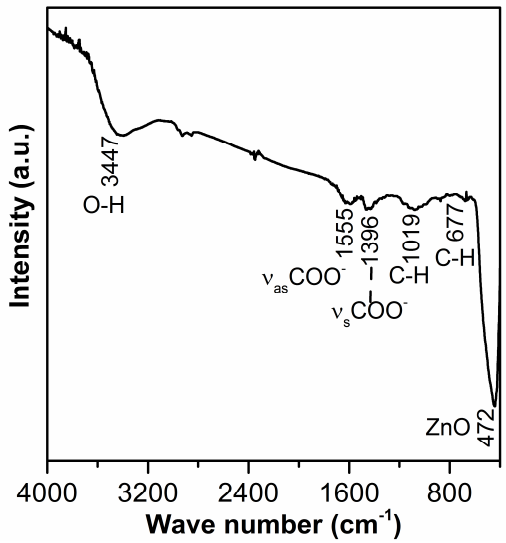

Fig. 3.15. FT-IR pattern of ZnO heat-treated at 673 K for 1 h

3.1.2.3. Photoelectrochemical characterization

The photoelectrochemical behaviour of the ZnO electrode was determined from the current-potential curves obtained in 0.1 M Na_2SO_4 solutions both in the dark and under UV irradiation (Fig. 3.16.).The potential was swept from –0.3 V to +1.0 V at 10 $mV \cdot s^{-1}$.

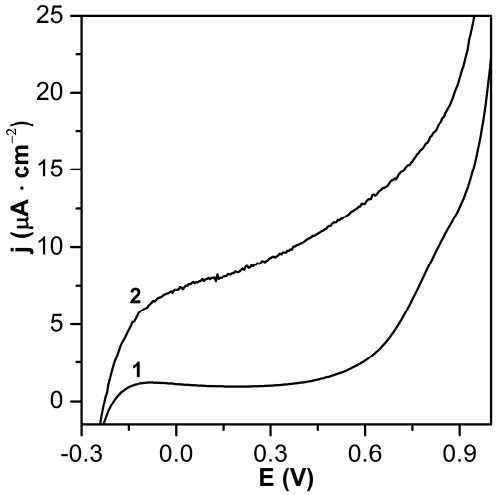

Fig. 3.16. Characteristic voltammograms in the dark (1) and under UV illumination (2) of the ZnO electrode deposited at 343 K. The potential scan rate v = 10 mV·s^{-1}, 0.1 M Na_2SO_4 solution at 293 K

Experimental data showed (Fig. 3.17 a) that at potentials higher than + 0.5 V the photocurrent reached its maximum value. The maximum current reflects the photoelectrochemical activity of ZnO that is caused by such multiple factors as the catalyst structure, the particle size and shape and the electrical conductivity [126]. An external electric field improves the transfer of the photogenerated electrons in the ZnO nano-layer coatings. The limiting photocurrent is reached when the electron transfer rate in the coating is close to the rate of the reactions of the photogenerated holes on the ZnO surface. Photocurrent has a tendency to decrease in higher than + 0.65 V potential region and this can be associated with the degradation of the ZnO coatings.

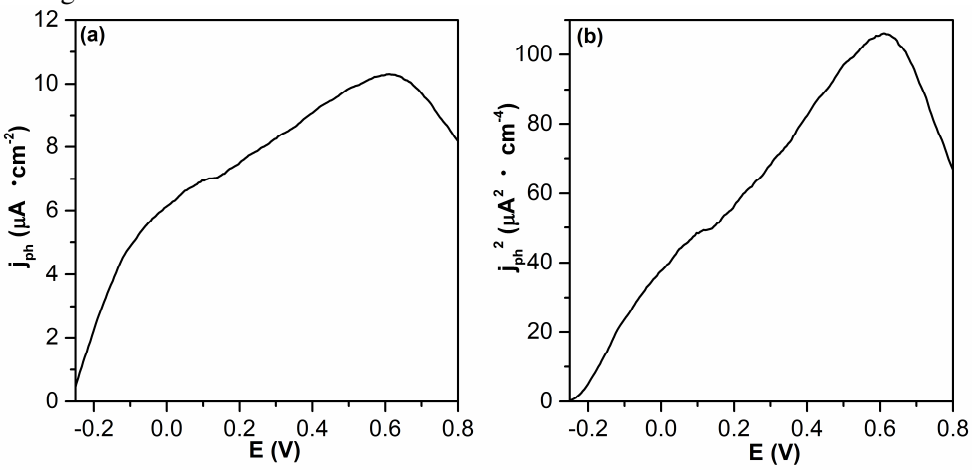

Fig. 3.17. (a) plot of the photocurrent density, j_{ph} with respect to the applied potential, E. (b) plot of the square of the photocurrent density, j_{ph}^2, with respect to the applied potential, E

For an n-type semiconductor, the photocurrent is due to the diffusion or the migration of the charge carriers depending on whether the semiconductor coating is particulate or continuous, respectively. In the case of thick and continuous coating, a depletion layer can be developed upon a contact with the electrolyte thus facilitating the separation of the photogenerated holes and electrons. According to Gartner-Butler model [135], the presence of the depletion layer can be determined by plotting the square of the photocurrent density, j_{ph}^2 with respect to the applied potential E. Figure 3.17 b shows that the plots j_{ph}^2 versus E are linear in the rising parts of the photovoltammograms thus confirming the formation of the depletion layer in the prepared coatings.

Based on the photocurrent measurements, the incident photon-to-current efficiency (IPCE) (equation 2.3) values of the ZnO photoelectrode were calculated and shown in Figure 3.18. It was found that these values are comparable to those for Degussa P25 TiO_2 electrode data measured under identical experimental conditions [118]. For as-deposited ZnO coatings, IPCE is at 1.95 % while for heat-treated coatings it is ~2 times higher (3.9 %). However, the values are lower if compared to those obtained for electrophoretically prepared ZnO coatings (Table 3.1).

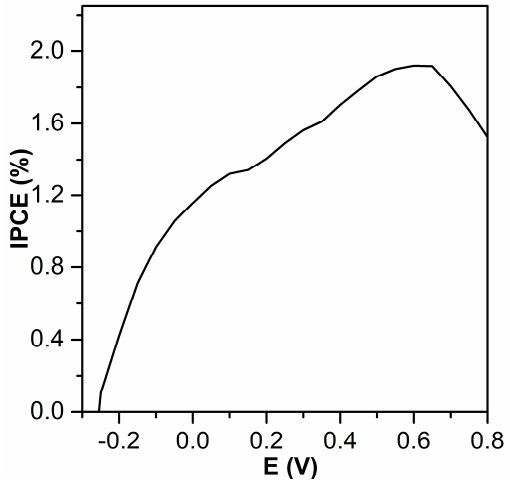

Fig. 3.18. The incident photon-to-current efficiency (IPCE) values for ZnO in the 0.1 M Na_2SO_4 electrolyte

The time dependence of the electrode current in the dark and under UV irradiation for the ZnO electrode is presented in Figure 3.19. In the case of as-deposited ZnO sample when the light was switched on, the observed current jumped to about +0.04 A and reached a steady-state value.

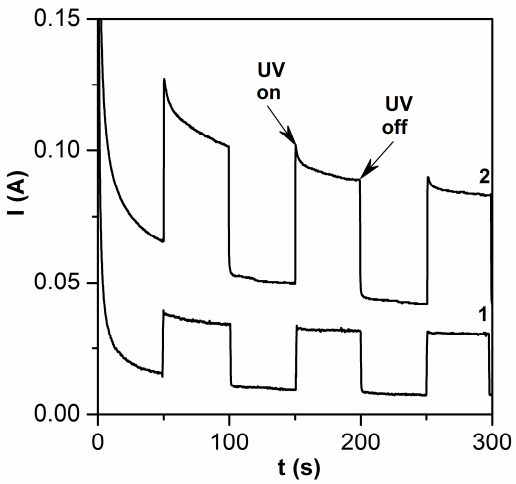

Fig. 3.19. Chronoamperometry curves of the ZnO electrode (1) and the ZnO electrode heat-treated at 673 K for 1 hour (2) in 0.1 M Na_2SO_4 solution in the dark and under UV illumination

When the light was switched off, the current of the ZnO decreased and returned to its initial value. The presented results show that the photocurrents increase upon the heat-treatment at 673 K.

The results presented in Figure 3.20 demonstrate that the steady state photocurrent increases with the increase in methanol concentration. It was stated [136] that the increase in the observed photocurrent is due to the interaction of the formed compounds and their partially-degraded intermediates with the oxide surface which does not inhibit the photohole capture process.

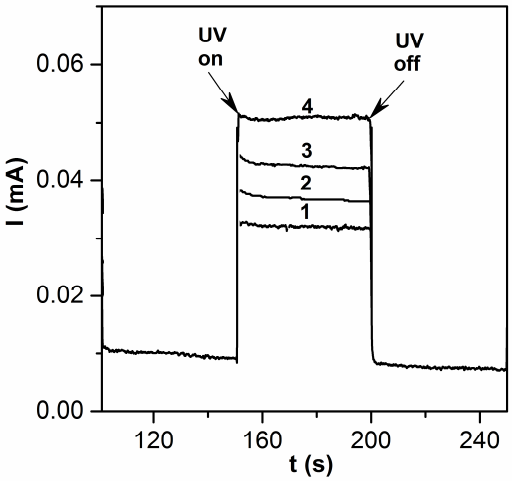

Fig. 3.20. Chronoamperometry curves of the ZnO electrode deposited at 343 K in the dark and under UV illumination in 0.1 M Na_2SO_4 solution and various methanol concentrations (mM): 1 – 0; 2 – 1; 3 – 2; 4 – 3

In order to establish the mechanism of the photoelectrochemical oxidation of the water-dissolved pollutants, a kinetic model was developed [137]. It was demonstrated that methanol oxidation mainly proceeds through an indirect hole transfer mechanism via surface-bound hydroxyl radicals followed by the so-called current-doubling effect [138]:

$$HO^{\bullet} + CH_3OH \rightarrow CH_2^{\bullet}OH + H_2O; \quad (3.12)$$

The radicals react further, according to the reaction:

$$CH_2^{\bullet}OH \rightarrow CH_2O + H^+ + e^-, \quad (3.13)$$

It is generally assumed [138, 139] that methanol molecules interact weakly with the oxide surface; they are not specifically adsorbed and do not compete with water molecules to be adsorbed on the oxide surface. On the contrary, strong and specific adsorption seems to be a necessary precondition for the direct hole mechanism [138].

During the (3.5, 3.6) reaction, one molecule of formaldehyde (CH_2O) and one electrone are formed. This means that one absorbed light quantum can initiate the formation of a pair of electrons, i.e., quantum efficiency is equal to two. However, such theoretical quantum efficiency is rarely achieved in practice due to the presence of impurities, crystal defects, etc. In addition, free $HO^{\bullet}$ radicals react with methanol molecules. Then, $CH_3O^{\bullet}$ can be formed:

$$HO^{\bullet} + CH_3OH \rightarrow CH_3O^{\bullet} + H_2O. \quad (3.14)$$

It is considered that the $CH_3O^{\bullet}$ radical does not affect the phenomenon of current doubling because it tends to dimerize:

$$2\ CH_3O^{\bullet} \rightarrow CH_3O{-}OCH_3. \quad (3.15)$$

3.1.3. Influence of Co–P_i catalyst on photoelectrochemical properties of ZnO

The literature research revealed (Sections 1.3) that the photoelectrochemical performance of oxide semiconductors can be enhanced by coupling them with a cobalt-based oxygen-evolving catalyst (termed Co–P_i) in phosphate electrolytes. That is why in the present thesis the influence of the Co–P_i catalyst on the photoelectrochemical activity of the prepared ZnO electrodes was tested. Both electrophoretically and electrochemically deposited ZnO coatings on AISI 304 steel were used as a support for the Co–P_i catalyst. The photoelectrochemical characterization of ZnO/Co–P_i coatings was carried out by using pH 11.5 phosphate solutions also taking into account the fact that ZnO was established to be the most photochemically stable substance in this pH [16].

The Co–P_i catalyst was deposited photochemically by immersing the ZnO electrode in the 0.1 M phosphate buffer (pH 7) with 0.5 mM cobalt nitrate and by irradiating the sample with UV light for various periods of time. The proposed mechanism [16, 20] demonstrated that the photogenerated holes possess sufficient overpotential to oxidize Co^{2+} to Co^{3+} ions in order to form the Co–P_i catalyst. During the process of photodeposition, the generated photoelectrons are consumed by the reduction of water or by the dissolved oxygen.

The linear sweep voltammetry in the dark and under UV irradiation was used to evaluate the influence of the Co–P_i catalyst on the photoelectrochemical performance of the ZnO coatings. The obtained experimental results are summarized in Figure 3.21. It was established that the presence of the Co–P_i catalyst on the surface of ZnO results in the decrease of photogenerated currents if compared to bare ZnO. It is suggested [16, 20, 22] that Co^{2+}/Co^{3+} ions can act as recombination centers for the photogenerated charge carriers thus reducing the overall performance of electrodes.

It should be pointed out that, similarly to the WO_3/Co–P_i electrode [140], ZnO/Co–P_i showed an enhanced electrocatalytic activity in the dark, which increased with the increase in Co–P_i photodeposition time. However, the highest activity of the Co–P_i catalyst can be achieved at a potential which is more positive than 1 V. Under these conditions, the dissolution of stainless steel takes place, and for this reason, more stable ZnO/Co–P_i support, for example, electroconductive glass should be employed.

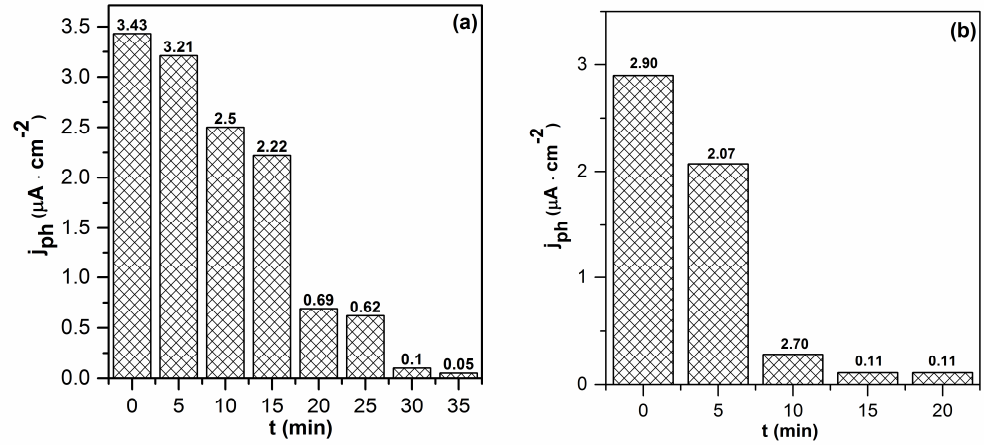

Fig. 3.21. Influence of the Co–P_i photodeposition time *t* on the photogenerated current of electrophoretically (a) and electrochemically (b) deposited ZnO coatings. *E* = +0.2 V, pH 11.5 phosphate electrolyte

3.2. Activity and structure of ZnCoO catalysts on AISI 304 stainless steel

3.2.1. Voltammetric behaviour of stainless steel in deposition electrolytes

Synthesis of mixed Zn-Co oxide coatings was carried out according to the procedure presented in Section 2.1.3.

Characteristic voltammetric behaviour of AISI 304 type stainless steel electrode in 0.1 M KNO_3 supporting electrolyte containing zinc and cobalt acetates is shown in Figure 3.22. It is similar to the pattern presented in Figures 3.8 and 3.9 and can be interpreted in terms of processes described by equations (3.8 – 3.11).

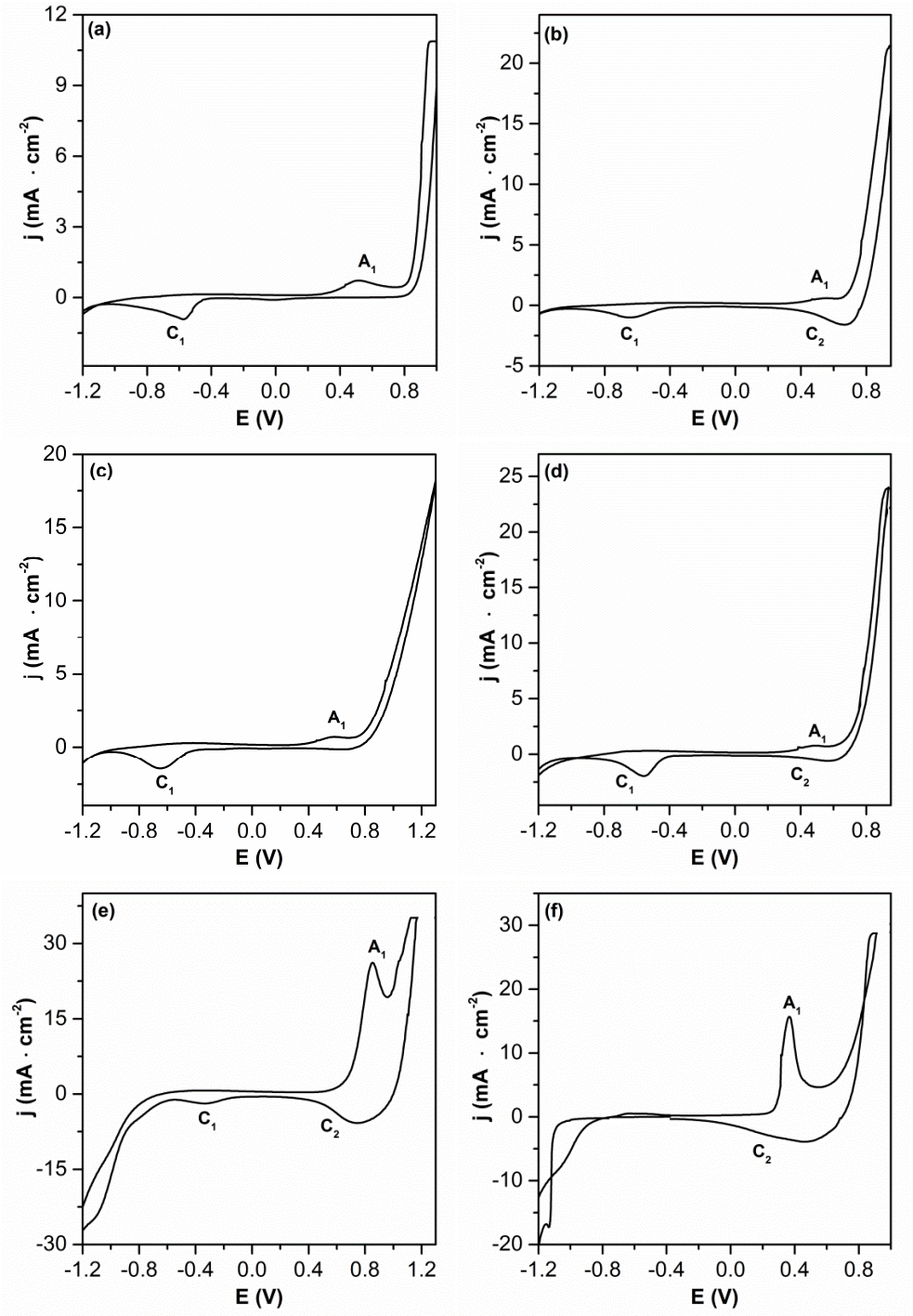

Fig. 3.22. Cyclic voltammograms of stainless steel in various electrolytes used for the synthesis for ZnO (a), ZnCoO1 (b), ZnCoO2 (c), ZnCoO3 (d), ZnCoO4 (e), $Co(OH)_2$ (f) coatings at 343 K. The potential scan rate is 50 $mV \cdot s^{-1}$

In this case additionally the formation of cobalt (hydr)oxide takes place according to the reaction:

$$Co^{2+}(aq) + 2OH^{-}(aq) \rightarrow Co(OH)_2(s) \quad (3.16)$$

When the potential was reversed at –1.2 V and scanned towards the positive values, an increase in the anodic current was observed at the potentials above 0.6 V. The peak A_1 at +0.8 V can be mainly associated with the oxidation of the electrodeposited compounds while the increase of the anodic current at the potentials above 0.9 V can be related to the evolution of oxygen and the oxidation of the stainless steel substrate.

3.2.2. Structural characterization

Atomic absorption spectroscopy revealed the varying ratio of Zn:Co in ZnCoO coatings (Table 3.2). It was discovered that with the increase in the cobalt concentration in the electrolyte bath, its amount in the prepared coatings increases as well.

Table 3.2 Ratio *Zn:Co* in the starting electrolyte and in the solid ZnCoO coating as measured by AAS

Sample notation	**Ratio *Zn:Co* in ZnCoO coating**	**Ratio *Zn:Co* in the starting electrolyte**
ZnCoO1	1:0.21	1:0.25
ZnCoO2	1:0.44	1:0.67
ZnCoO3	0.80:1	0.67:1
ZnCoO4	0.28:1	0.25:1

SEM images of as-deposited and heat-treated zinc-cobalt oxide coatings are shown in Figure 3.23.

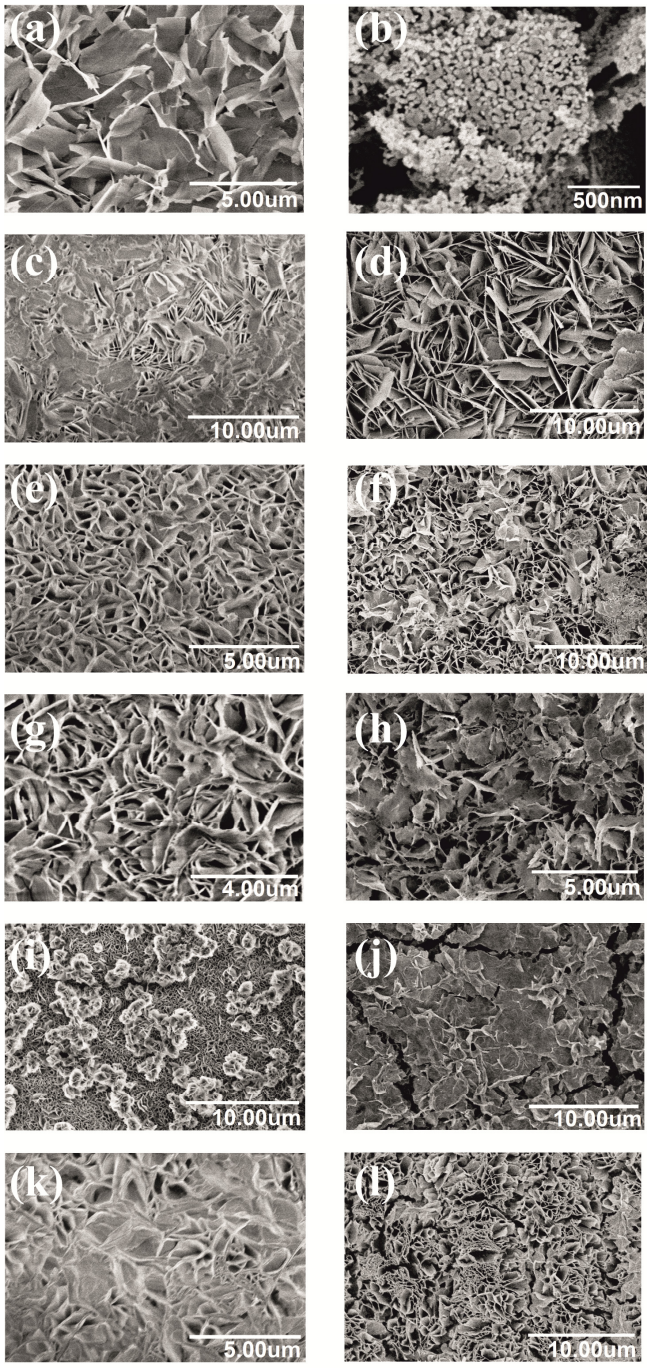

Fig. 3.23. Representative SEM images of as-deposited and heat-treated at 673 K for 1 h various coatings: a, b – ZnO; c, d – ZnCoO1; e, f – ZnCoO2; g, h – ZnCoO3; i, j – ZnCoO4; k – $Co(OH)_2$; l – Co_3O_4

The as-deposited (Fig. 3.23 a, c, e, g, i, k) coatings are lamellar, possibly with intercalated acetate ions. It is seen that the annealing at 673 K for 1 h considerably changed only the ZnO coating surface to the granular structure (Fig. 3.23 b) whereas ZnCoO or Co_3O_4 coatings (Fig. 3.23 d, f, h, j, l) retained the same porous lamellar morphology.

XRD analysis of as-deposited samples of bare zinc oxide showed three peaks at 2θ of 31.66, 34.38 and 36.26° thus suggesting a crystalline ZnO structure (Fig.3.24. 3a; curve 1) (PDF 04-004-4120). The strong low-angle reflection peak at 2θ of 6.65° can be associated with the acetate groups intercalated into the zinc oxide structure [115, 131] (PDF 00-056-0569). After the heat-treatment at 673 K for 1 h, the XRD analysis revealed diffraction peaks corresponding to the well-crystallized ZnO (Fig. 3.24. 3b, curve 1). According to the Scherrer's equation (2.1), the average ZnO crystallite size was calculated to be 30 nm. The presence of cobalt acetate in the electrolyte bath leads to poorly crystallized deposits of zinc-cobalt hydroxides (Fig. 3.24. 3a, curves 2 and 3). The crystallinity of the samples is greatly improved upon the heat-treatment at 673 K (Fig. 3.24. 3b, curves 2 and 3).

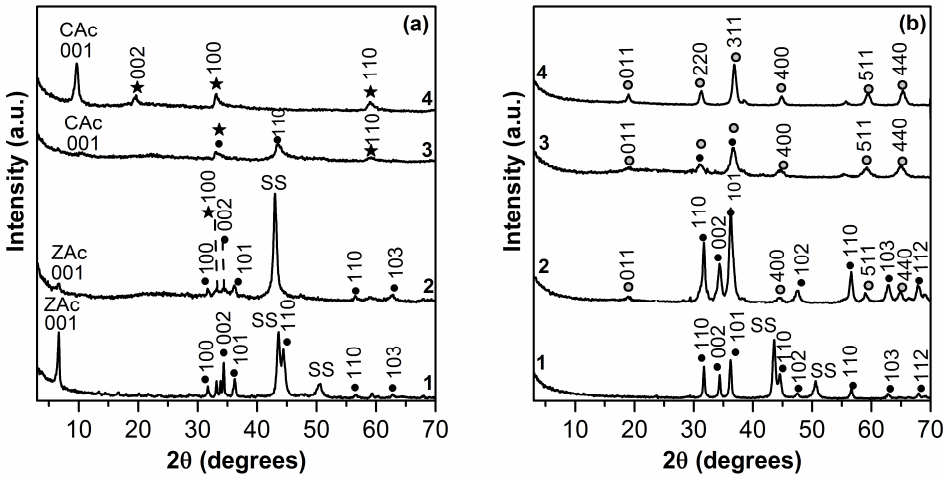

Fig. 3.24. XRD patterns of as-deposited (a) and heat-treated (b) coatings: 1 – ZnO; 2 – ZnCoO1; 3 – ZnCoO3; 4 – $Co(OH)_2/Co_3O_4$. Abbreviations: CAc – $Co(CH_3COO)_2$; SS – stainless steel; ZAc – $Zn(CH_3COO)_2$; ★– $Co(OH)_2$; ○ – Co_3O_4; ● – ZnO

The XRD pattern of as-prepared cobalt hydroxide reveals diffraction peaks at 19.66, 33.16 and 59.28° corresponding to cobalt hydroxide (Fig. 3.23, 3a, curve 4). The small number of reflection peaks is an indication of poorly ordered samples for $Co(OH)_2$ and ZnCoO3. On the basis of the obtained results it can be assumed that the hydroxide synthesized here is of a mixed phase showing reflections characteristic of both α- and β-modifications. The strong low-angle reflection peak at 9.76° can be found with d-spacing of 9.05 Å. This can be associated with acetate groups intercalated (PDF 00-056-0568) into the hydrotalcite-like α-cobalt hydroxide structure (PDF 00-002-0925). This value is intermediate if compared to those

reported in scholarly literature for acetate intercalated α-cobalt hydroxide, specifically, 8.36 Å in [141] and 12.65 Å in [142].

The presence of a diffraction peak at 19.66° (Fig. 3.24. 3a, 4) can be related to the formation of β-modification (PDF 00-030-0443). The diffraction peaks at 33.16 and 59.28° exhibit an asymmetry on the higher angle side. This feature indicates the presence of turbostratic materials in which the stacked layers are randomly oriented relative to the principal crystallographic axis [120]. The corresponding XRD pattern of thermally treated samples (Fig. 3.24. 3b, curve 4) reveals diffraction peaks which can be readily attributed to the cubic phase of Co_3O_4 (PDF 01-078-5634)[143]. According to the Scherrer's equation, the average Co_3O_4 crystallite size was calculated to be 29 nm. The instrumental broadening was not considered for the calculation of crystallite size.

The Raman analysis for Co rich samples shows peaks at 191, 479, 514, 604 and 674 cm^{-1}. This is typical of spinel structure compounds with the $Co^{2+}(Co_2^{3+}O_4)$ configuration in Co_3O_4 [143]. This shows that the bulk structure within the analysis volume of the Raman signal (~1 mm) is comprised of the oxide phase whereas ~3nm surface layers, as obtained from the XPS analysis, are comprised of $Co(OH)_2$. As-deposited ZnO (Fig. 3.25, 4a, curve 1) exhibits peaks at 410, 439 and 666 cm^{-1} due to the ZnO. Peaks at 330, 410 and 439 cm^{-1} are typical of wurtzite ZnO [144]. Peaks at 945 and 1046 cm^{-1} can be assigned to other impurities present in the sample, presumably due to the hydrocarbons, as evidenced from the FT-IR data.

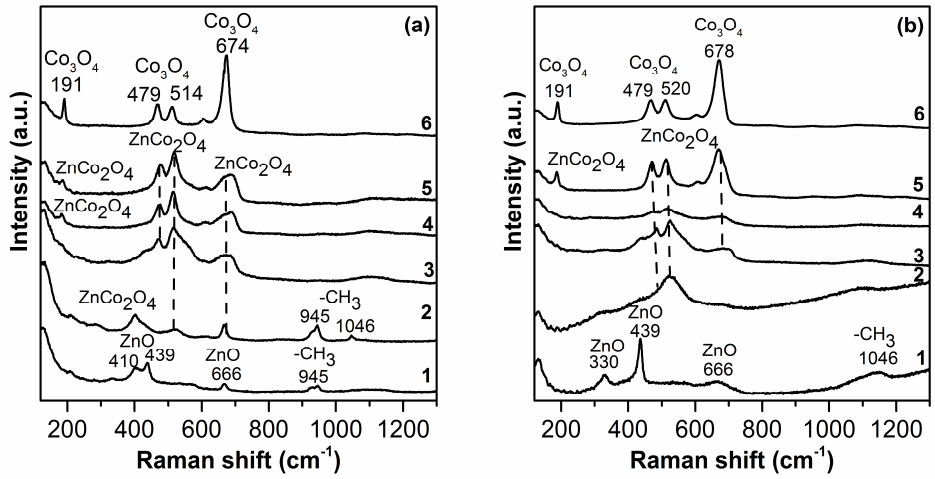

Fig. 3.25. Raman spectra of as-deposited (a) and heat-treated at 673 K (b) coatings: 1 – ZnO; 2 – ZnCoO1; 3 – ZnCoO2; 4 – ZnCoO3; 5 – ZnCoO4; 6 – $Co(OH)_2$/ Co_3O_4

In as-deposited ZnCoO (Fig. 3.25, 4a; curves 2 – 4), a broad region between 650 and 690 cm^{-1} is due to the octahedral oxygen motion [145]. It is lower in energy than the peak of pure Co_3O_4 due to the local disorder in the spinel crystal lattice with the substitution of the Zn atom [145]. Broad features centered around 514 and 475 cm^{-1} are due to the combined vibrations of tetrahedral and octahedral oxygen ion motions in ZnCoO4 [146]. The weakening of these bands is much faster in

heated samples where they are already absent in ZnCoO1 (Fig. 3.25, 4b; curve 2) and are related to the decreasing concentration of the Co octahedral unit. The broad peak at 520 cm^{-1} present in ZnCoO1 and only slightly discernible in ZnCoO1 (Fig. 3.25. 4a, curve 2) is due to the modes related to shallow donor defects bound to the tetrahedral Co sites or due to the internal d-d* transition in Co^{2+} [145].

Overall, the Raman data shows a gradual transition of the lattice substituted ZnO into a crystalline Co_3O_4 with the peak at 674 cm^{-1} diminishing in intensity in ZnCoO4, when compared to the pure cobalt oxide phase. Since it is associated with the octahedrally coordinated Co^{3+}, some interstitial substitution can be present, consistent with the fact that the peak at 674 cm^{-1} is lower in intensity before, rather than after the heat treatment. Collectively, the Raman data shows that the spinel crystal structure is obtained, especially in the cases involving heat-treated higher Co concentrations (Fig. 3.25, 4b; curve 5).

The experimental results of the FT-IR analysis are presented in Figure 3.26. and summarized in Table 3.3.

Table 3.3 The results of FT-IR analysis

Wave number, cm^{-1}	**Assignments**	**Literature**
as-deposited samples		
3303 – 3347	ν H–O (–OH)	[123]
1556 – 1579	ν_{as} COO^- (CH_3COOH)	[123]
1375 – 1399	ν_s COO^- (CH_3COOH)	[123]
1337 – 1345	δ_{as} C–H (–CH_3)	[123]
1019 – 1024	δ_s C–H (–CH_3)	[123]
662	Co–O ($Co(OH)_2$)	[147]
462	Zn–O	[124]
Wave number, cm^{-1}	**Assignments**	**Literature**
heat-treated samples		
2800 – 3600	ν H–O (–OH)	[123]
574	Co–O (Co_3O_4)	[147]
666	Co–O ($Co(OH)_2$)	[147]
432	Zn–O	[124]

As-deposited ZnCoO coatings reveal (Fig. 3.26. 5a, curves 2–4) the high intensity absorption peak at 667 cm^{-1} which corresponds to Co–O bond [147] where Co^{2+} ions are situated in tetrahedral position. The obtained experimental results show that this characteristic band becomes more intense with the decrease of zinc concentration. It can be concluded that the asymmetrical and symmetrical stretching vibrations of the acetate ions intensity decreases when the coatings are heat-treated. With an increase of the cobalt concentration peaks at 666 cm^{-1}, the intensity increases as well.

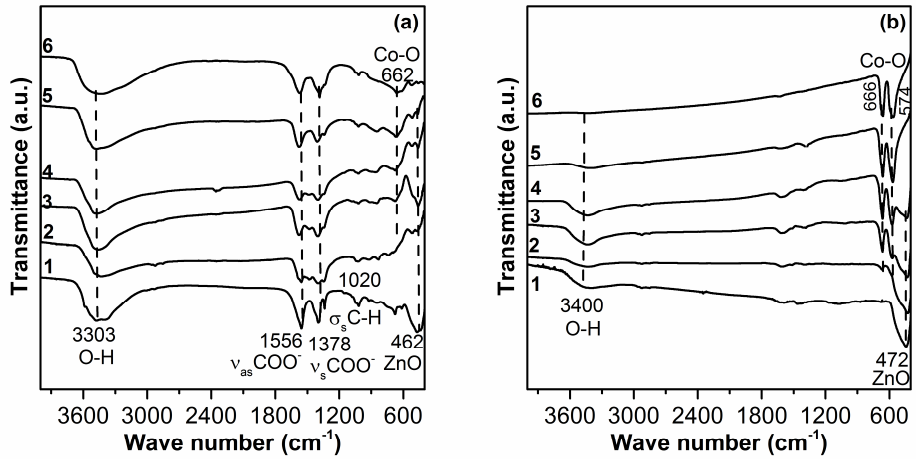

Fig. 3.26. FT-IR spectra of as-deposited (a) and heat-treated at 673K (b) coatings: 1 – ZnO; 2 – ZnCoO1; 3 – ZnCoO2; 4 – ZnCoO3; 5 – ZnCoO4; 6 – $Co(OH)_2/Co_3O_4$

A new peak at 574 cm^{-1} appears and gradually becomes more prominent. This peak described above is associated with Co^{3+} ions situated in the octahedral position in the spinel-type Co_3O_4 crystal lattice (Fig. 3.26.5, b, curves 2–4). The notable disappearance of the peaks in the $-CH_3$ bending and -COOH stretching region between 1200 and 1600 cm^{-1} is due to the elimination of the organic residue during the thermal treatment.

In order to analyze the surface composition of the samples, XPS analysis was performed, and the obtained high resolution spectra of Zn2p, Co2p, O1s and valence band regions are shown in Figures 3.27. and 3.28. for the as-deposited and heat-treated at 673 K samples, respectively.

Two distinct doublets are present in the Zn2p region between the samples. First, in the as-deposited samples (Fig. 3.27 a), only one doublet is present with the $Zn2p_{1/2}$ at 1045 eV and $Zn2p_{3/2}$ peak at 1021.9 eV due to the Zn^{2+}-O bonds. The second component of the $Zn2p_{3/2}$ peak at 1021.0 eV was only apparent in heat-treated ZnCoO samples shown in Figure 3.28 a. The presence of the second component is only clear when comparing the $Zn2p_{3/2}$ peak FWHM of as-deposited and heat-treated samples at 1.72 and 2.45 eV, respectively. The peak at 1021 eV may be caused by the metallic Zn bonds formed via heating. Alternatively, bonds involving Zn and Co metals due to their substoichiometric spinel composition can be formed at high temperatures.

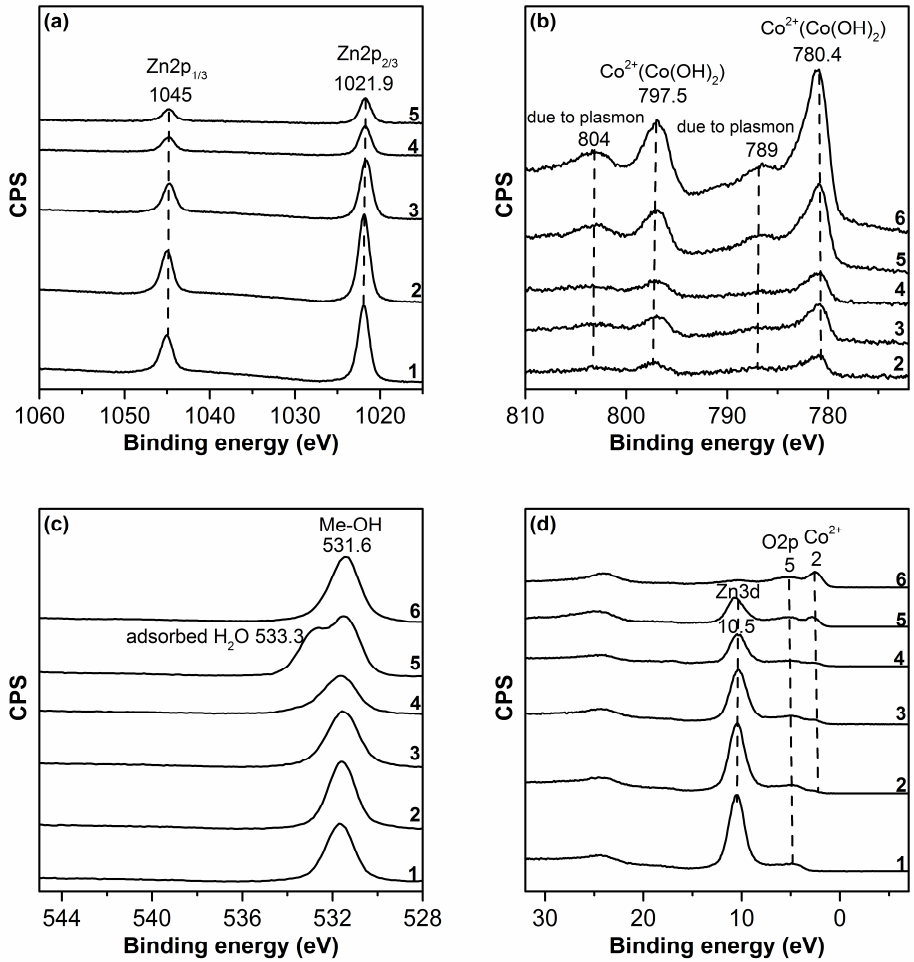

Fig. 3.27. XPS spectra of Zn2p (a), Co2p (b), O1s (c) and valence band (d) of as-deposited coatings: 1 – ZnO; 2 – ZnCoO1; 3 – ZnCoO2; 4 – ZnCoO3; 5 – ZnCoO4; 6 – $Co(OH)_2$

Figure 3.27 b shows peaks at 797.5 and 780.4 eV for as-deposited samples assigned to $Co2p_{1/2}$ and Co $2p_{3/2}$ lines of $Co(OH)_2$ [148]. $Co(OH)_2$ can be formed in humid environment on the top of the sample surface and be detected due to the small electron inelastic mean free path employed in the XPS analysis. The peaks at 786.0 and 804.0 eV in Fig. 3.27 b are due to the plasmon excitations. Figure 3.28 b shows two strong asymmetric peaks due to the spin-orbit splitting with the binding energies of 795.5 eV and 779.8 eV for the $Co2p_{1/2}$ and Co $2p_{3/2}$ lines thus confirming the Co^{2+} and Co^{3+} oxidation states of Co_3O_4 for heat-treated samples.

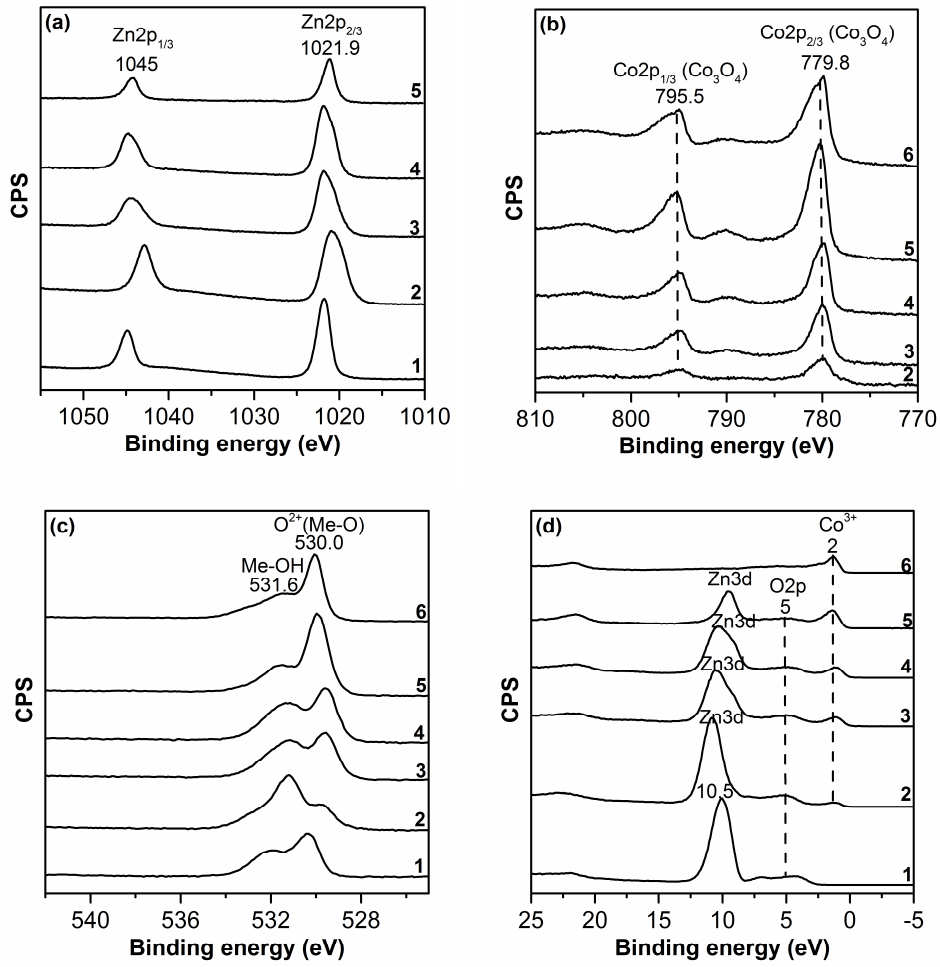

Fig. 3.28. The XPS spectra of Zn2p (a), Co2p (b), O1s (c) and the valence band (d) of the coatings heat-treated at 673 K: 1 – ZnO; 2 – ZnCoO1; 3 – ZnCoO2; 4 – ZnCoO3; 5 – ZnCoO4; 6 – Co_3O_4

O1s regions in the as-deposited samples yielded a peak at 531.6 eV due to the surface hydroxyl groups of $Co(OH)_2$ and $Zn(OH)_2$. The heat-treated samples presented a peak at 530.0 eV due to the metal-oxygen bonds in ZnO and Co_3O_4 mixture as well as the 531.6 eV peak, typical for metal hydroxides [149, 150]. Some coatings exhibited a shoulder at 533.3 eV due to the adsorbed or trapped water molecules [116].

Finally, valence band regions shown for ZnO, Co_3O_4 and ZnCoO1 throughout the ZnCoO4 samples before and after the heating showed a prominent gradual shift of the valence band edge towards the vacuum level. This can be used as a measure of the valence band maximum position [151]. In Zn-rich samples, the peak at 10.5 eV is due to the Zn3d bands whereas that at ~5eV is due to O2p bands [152]. An increase in the peak intensity at ~2eV in Co-rich samples is due to the complex

structure assigned to Co^{3+} and Co^{2+} ion valence bands [153]. This is consistent with the fact that the Co_3O_4 band gap is much smaller than that of ZnO (1.5 to 2.5 versus 3.2 eV, respectively) [153]. It is important to observe that even at low cobalt amounts, the band gap transition and the corresponding electronic properties will be dominated by the cobalt oxide frontier crystalline bands.

Elemental quantification performed by using XPS spectra is shown in Table 3.4.

Table 3.4 The results of XPS elemental analysis

Sample	Co:Zn	O:Zn	Co:Zn	O:Zn
	as-deposited samples		heat-treated samples	
ZnCoO1	0.16	2.40	0.15	1.34
ZnCoO2	0.35	3.11	0.33	1.77
ZnCoO3	0.41	4.90	0.41	1.88
ZnCoO4	1.77	11.73	1.70	4.40

It can be seen that the amount of Co increases in the as-deposited as well as heat-treated samples parallelly with the increase of the corresponding oxygen amount. While the Co:Zn ratio is almost the same in both as-deposited and heat-treated samples, the O:Zn ratio is much higher in the as-deposited samples. This is due to the adsorbed hydroxyl and carbonate groups on the surface which are degassed upon annealing.

3.2.3. Electrochemical characterization

The photoelectrochemical behaviour of the zinc-cobalt oxide electrode was determined from the current-potential curves obtained in 0.1 M Na_2SO_4 or 0.1 M NaOH solutions both in the dark and under UV irradiation. During these experimental runs, the electrode potential was swept from – 0.3 V to + 0.8 V at 10 $mV \cdot s^{-1}$ scan rate. The Zn-Co oxide coatings were polarized in the 0.1 M NaOH solution because they are more stable in the alkaline media; water anodic oxidation in the alkaline media is a much faster process than in the neutral media. From the data provided in Figures 3.29 and 3.30 it is evident that UV illumination caused an increase in the observed currents. The increase in the observed currents in the 0.1 M Na_2SO_4 electrolyte is associated with the AISI 304 stainless steel dissolution and the oxygen evolution. As in the case of the 0.1 M NaOH electrolyte, the increase in the observed currents is for the same reason as Na_2SO_4, only the electrolyte is alkaline and the oxygen evolution starts earlier, specifically, at above 0.45 V. Also, ZnO and Zn-Co oxide coatings are stable at alkaline electrolyte. The annealing of the ZnO coatings at 673 K significantly improved the photoelectrochemical performance of the electrode.

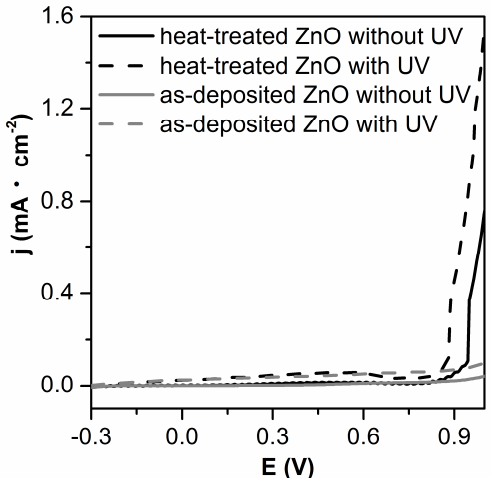

Fig. 3.29. Characteristic voltammograms in the dark and under UV illumination of ZnO electrodes in 0.1 M Na_2SO_4 electrolyte at 10 $mV \cdot s^{-1}$ potential scan rate

It can be stated that the observed currents both in the dark and under UV illumination are ≈ 10 times stronger in NaOH solution than in Na_2SO_4.

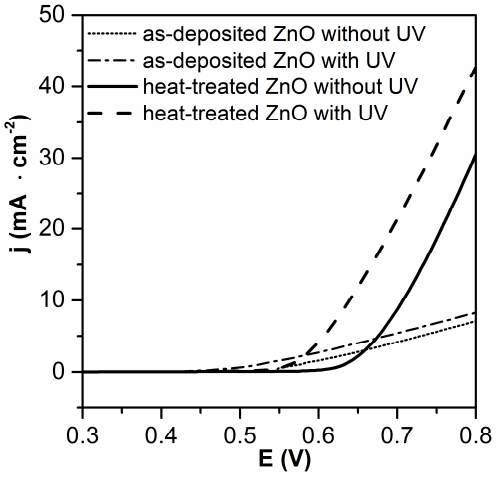

Fig. 3.30. Characteristic voltammograms in the dark and under UV illumination of ZnO electrodes in 0.1 M NaOH electrolyte at 10 $mV \cdot s^{-1}$ potential scan rate

Therefore, photoelectrochemical behaviour of ZnO and mixed Zn-Co oxide coatings in alkaline 0.1 M NaOH (pH=13.1) electrolyte were measured. The results presented in Figure 3.31. highlight the dependence of the photocurrent density as a function of the applied bias for various Zn-Co oxide electrodes heat-treated at 673 K. The measurements demonstrate that the onset potential for the photocurrent of as-deposited ZnO is about 0.5 V. In the case of ZnCoO1 coatings, the photocurrent onset potential was shifted by approximately 0.2 V; however, the

presence of cobalt oxide results in the decrease of the observed photocurrents. At a higher cobalt content, the photoactivity of ZnCoO coatings is suppressed.

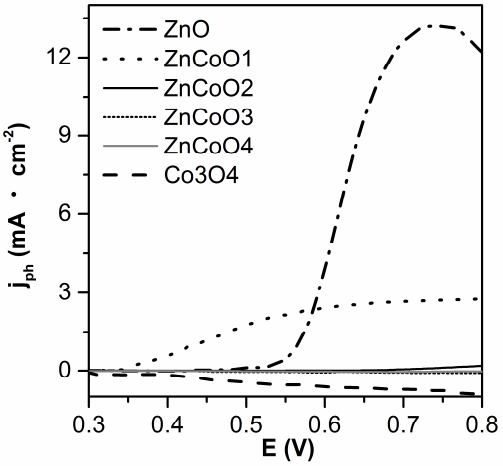

Fig. 3.31. The photocurrent density (j_{ph}) with respect to the applied potential for various electrodes in 0.1 M NaOH electrolyte at 10 mV·s^{-1} potential scan rate

In order to investigate the pseudocapacitive properties of the prepared Zn-Co oxide coatings, a set of electrochemical measurements was carried out by using 0.1 M NaOH solution in the dark. Figures 3.32. and 3.33. show the cyclic voltammetric curves of the as-deposited and heat-treated ZnCoO electrodes, respectively.

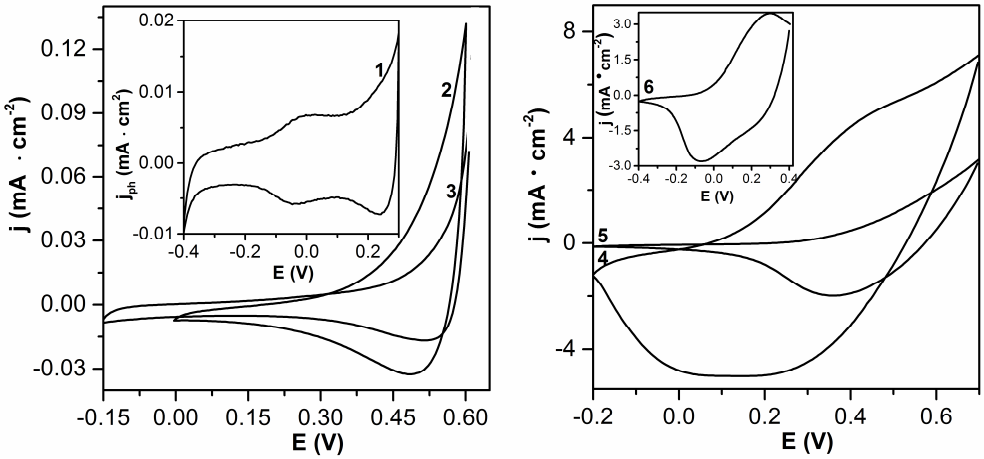

Fig. 3.32. 10th cycle of cyclic voltammograms of the as-deposited catalysts in 0.1 M NaOH electrolyte: 1 – ZnO, 2 – ZnCoO1, 3 – ZnCoO2, 4 – ZnCoO3, 5 – ZnCoO4, 6 – $Co(OH)_2$. The potential scan rate is at 50 mV·s^{-1}

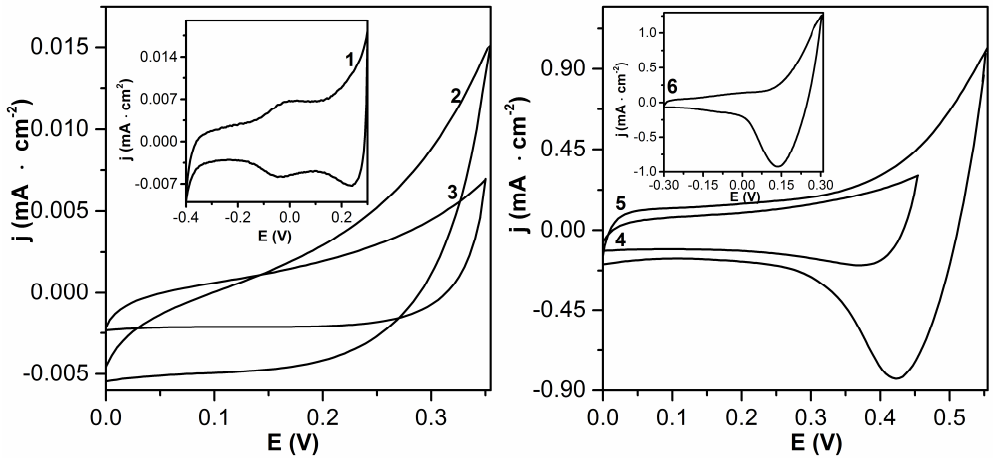

Fig. 3.33. 10th cycle of cyclic voltammograms of heat-treated catalysts in the 0.1 M NaOH electrolyte: 1 – ZnO; 2 – ZnCoO1; 3 – ZnCoO2; 4 – ZnCoO3; 5 – ZnCoO4; 6 – Co_3O_4. The potential scan rate is at 50 $mV \cdot s^{-1}$

By using equation (2.4), the values of specific capacitance were calculated. The results are summarized in Table 3.5. The experiment results revealed that bare ZnO is characterized by very low specific capacitance. The presence of cobalt (hydr)oxide significantly improves the pseudocapacitive properties.

Table 3.5 Pseudocapacity values for various coatings

Sample	Specific capacitance, $F \cdot g^{-1}$	
	as-deposited	heat-treated
ZnO	0.5	0.3
ZnCoO1	0.8	0.2
ZnCoO2	3	0.3
ZnCoO3	60	18
ZnCoO4	194	21
$Co(OH)_2$/ Co_3O_4	119	87

It can thus be assumed that the energy storage mechanism of the prepared mixed oxide coatings mainly originates from faradaic redox reactions assigned to the $Co(OH)_2$/CoOOH redox couple [120, 154]:

$$Co(OH)_2 + OH^- \rightarrow CoOOH + H_2O + e^-; \quad (3.16)$$

$$CoOOH + H_2O + e^- \rightarrow Co(OH)_2 + OH^-; \quad (3.17)$$

It was observed that sweeping the potential in anodic area results in all the ZnCoO coatings becoming darker; this especially concerns ZnCoO3 and ZnCoO4, which become black. This shows a probable formation of CoOOH, as reported previously [155].

According to the experimental results, the as-deposited coatings are characterized by higher pseudocapacity if compared to heat-treated coatings. In addition, it was determined that with the increase in the cobalt content in the prepared coatings, their pseudocapacity increases as well. However, bare $Co(OH)_2$ coatings were found to have a lower specific capacitance in comparison with the researched ZnCoO4 sample. This can be explained by the fact that the pseudocapacity is strongly influenced by the electrode layer structure, the amount of electroactive material and the electron and ion transfer rates within the layer [156]. In summary, it can be concluded that as-deposited coatings are characterized by a higher surface area and a larger amount of electroactive material.

3.3. ZnCoO coatings on TEC15 type glass

3.3.1. Characterization of bare zinc and cobalt oxides

The coatings were prepared according to the procedure presented in Section 2.1.3. In order to test the influence of electrolysis bath temperature on structure and properties of the coatings, they were electrodeposited at 293 and 343 K.

XRD analysis of as-deposited samples at 293 K and 343 K of bare ZnO showed zinc acetate group peaks at 2θ of 6.75° (Fig. 3.34. (a) curve 1), and 6.5°, 13.35°, 20.05° (Fig. 3.35. (a) curve 1). The strongest diffraction peak at 2 θ = 6.5° – 6.75°corresponds to an interlayer d-spacing of zinc acetate (the 001 diffraction of layered structure); the peaks at 13.35° and 20.05° can be attributed to the second and third order diffraction of (00l) plane of $Zn(OH)_x(CH_3COO)_y \cdot zH_2O$ (PDF 00-056-0569), respectively [157]. After the heat-treatment at 673 K and 873 K for 1 h there is no acetate groups intercalated into zinc oxide structure (Fig. 3.34. and 3.35. (a) curve 2 and 3). In as-deposited at 293 K bare ZnO XRD spectra is seen only one characteristic peak at 2θ of 33.45° and two peaks that has low intensity at 2θ of 61.61°, 65.58°(Fig. 3.34. (a) curve 1). Whereas in as-deposited at 343 K ZnO XRD spectra is seen three characteristic peaks at 2θ of 31.76°, 34.40°, 36.25° and four lower intensity peaks at 2θ of 56.62°, 62.85°, 65.55°, 68.0°(Fig. 3.35. (a) curve 1) and it can be stated that under these conditions ZnO (PDF 04-004-4120) is well-crystallized and is in wurtzite structure. It can be concluded that ZnO as-deposited at 343 K is high-quality wurtzite than ZnO as-deposited at 293 K. The heat-treatment increases the intensity of the peaks especially heat-treatment at 873 K improves coatings quality and crystalinitty. According to the Scherrer's equation the average ZnO crystallite size was calculated and is showed in Table 3.6. It is seen that annealing increases crystallite size except for as-deposited at 343 K and heat-treated at 873 K ZnO coating.

Table 3.6 The average ZnO crystallite size calculated according to the Scherrer's equation

Sample	Crystallite size, nm
ZnO as-deposited at 293 K	7.2
ZnO as-deposited at 293 K and heat-treated at 673 K	27.6
ZnO as-deposited at 293 K and heat-treated at 873 K	35.7
ZnO as-deposited at 343 K	40.3
ZnO as-deposited at 343 K and heat-treated at 673 K	45.8
ZnO as-deposited at 343 K and heat-treated at 873 K	30.0

The incorporation of acetate impurities in as-prepared ZnO coatings is confirmed by infrared absorption analysis as well (Fig. 3.34 and 3.35; curves 2 and 3). It is noticeable that the peaks at 1556–1560 cm^{-1} and 1385–1398 cm^{-1} are of lower intensity while the peaks at 677 cm^{-1}, 1018 cm^{-1} and 1339 cm^{-1} disappear when the coatings are heat-treated, especially at 873 K temperature. As well as in the case above, the heat-treatment reduces the intensity of hydroxy groups' peaks at 3439–3445 cm^{-1} and increases the intensity of the Zn–O group stretch at 472 cm^{-1}. Besides, the as-deposited at 293 K ZnO coating IR absorption of the Zn–O group is of lower intensity than as-deposited at 343 K ZnO which is more clearly visible (Fig. 3.34 and 3.35; curve 1).

The optical characterization of the prepared ZnO coatings was carried out by UV-vis diffuse reflectance spectroscopy (UV-vis DRS). All the spectra were taken in the range of 200 – 800 nm. Figures 3.34 c and 3.35 c show the diffuse reflectance spectra R as a function of the wavelength for various ZnO samples. The absorption in the UV region for as-deposited sample can be attributed to the presence of impurities as it is confirmed by XRD and FTIR analysis. The band gap of the heat-treated ZnO samples was estimated from diffuse reflectance spectra by plotting the square of the modified Kubelka–Munk function as a function of energy. The Kubelka–Munk function $F(R)$ is expressed by the relation [158]

$$F(R) = \frac{(1-R)^2}{2R} \tag{3.18}$$

where R is the magnitude of reflectance.

In order to calculate the band gap, the slope of the $F(R)^2$ curve is extrapolated until it intersects the energy axis at $F(R)^2 = 0$.

The band gap energies are determined to be in the range of 3.31 – 3.35 eV. Similar values were obtained by taking the absorption edge and using (2.2) equation. The calculated values of the band gap of the heat-treated ZnO samples are summarized in Table 3.7. These results are in good agreement with the data of previously described researches [159].

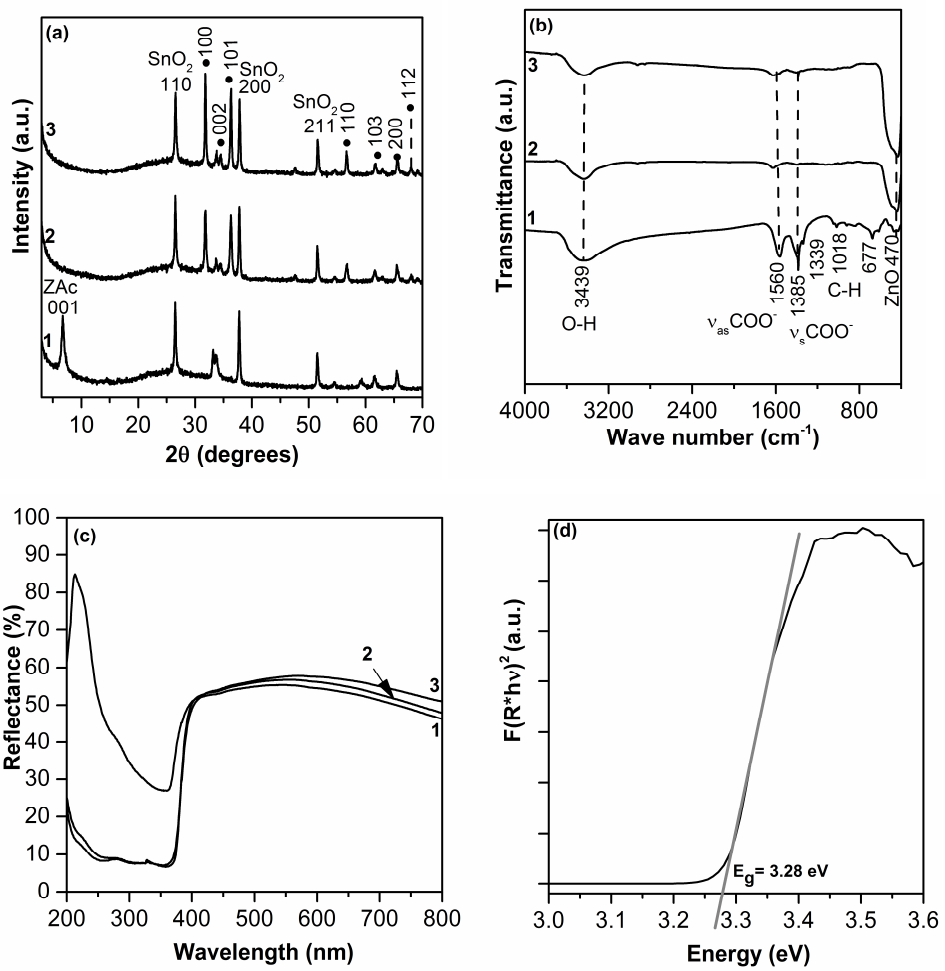

Fig. 3.34. XRD (a), FT-IR (b), UV-vis DRS spectra (c) and the DRS results according to the K.-M. function (d) of ZnO coatings: 1 – as-deposited at 293 K; 2 – heat-treated at 673 K for 1h; 3 – heat-treated at 873 K for 1 h.
Abbreviations: ZAc – $Zn(CH_3COO)_2$; ● – ZnO

Table 3.7 ZnO coatings bang-gap energy values calculated from 2.2 equation

Sample	Absorption edge λ, nm	E_g, eV
ZnO as-deposited at 293 K and heat-treated at 673 K	375	3.31
ZnO as-deposited at 293 K and heat-treated at 873 K	370	3.35
ZnO as-deposited at 343 K	340	3.65
ZnO as-deposited at 343 K and heat-treated at 673 K	371	3.34
ZnO as-deposited at 343 K and heat-treated at 873 K	370	3.35

It is generally accepted that the estimation of E_g when using Kubelka–Munk plot is more accurate (than that calculated from 3.11 equation) and is shown for as-deposited at 293 and 343 K ZnO coatings that are heat-treated at 673 k for 1 h (Fig. 3.34–3.35 d).

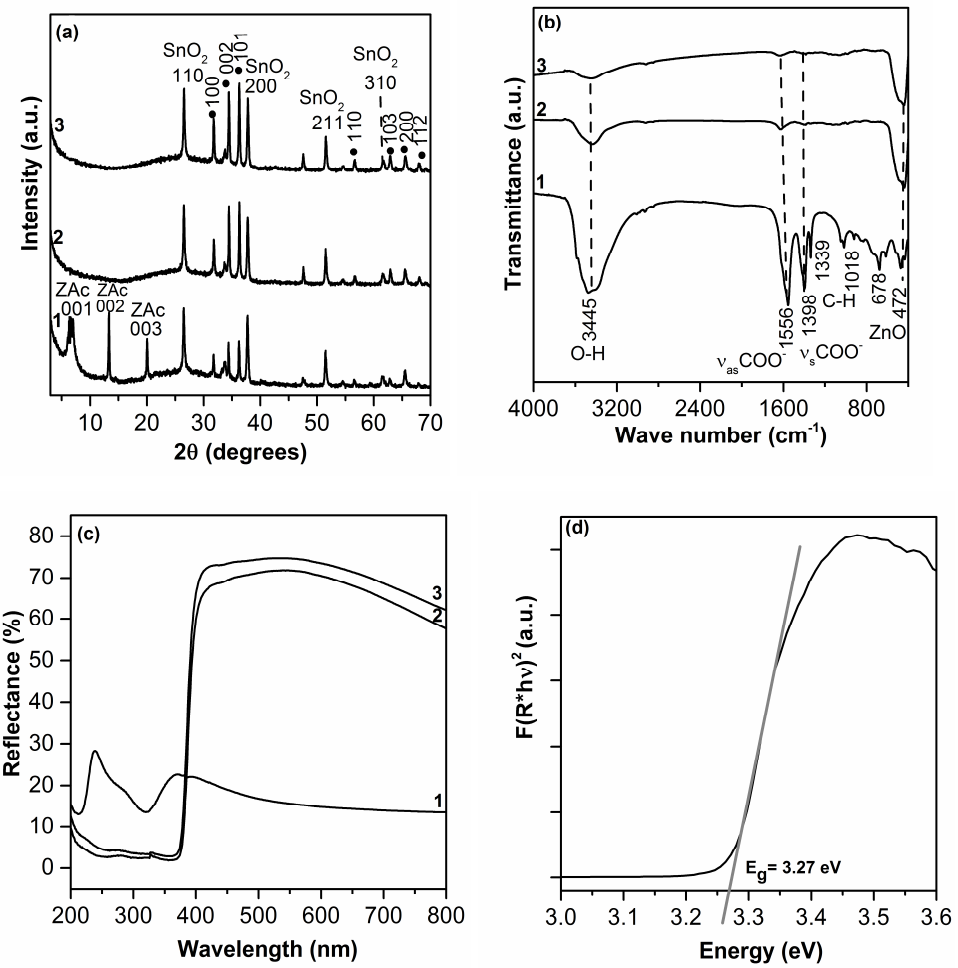

Fig. 3.35. XRD (a), FT-IR (b), UV-vis DRS spectra (c) and DRS results according to K.-M. function (d) of ZnO coatings: 1 – as-deposited at 343 K; 2 – heat-treated at 673 K for 1h; 3 – heat-treated at 873 K for 1 h. Abbreviations: ZAc – $Zn(CH_3COO)_2$; ● – ZnO

Figure 3.36. (a) shows the SEM image of the as-deposited at 343 K and heat-treated at 873 K ZnO coating. It is to be noticed that thin nanosheet structures growing vertically on the substrate are obtained. The obtained EDS elemental map is shown in Figure 3.36. (b). The O and Zn exhibit the same spatial distribution in the elemental map. This indicates a relatively uniform distribution of the elements in the synthesized products and demonstrates that the ZnO coating is homogenous.

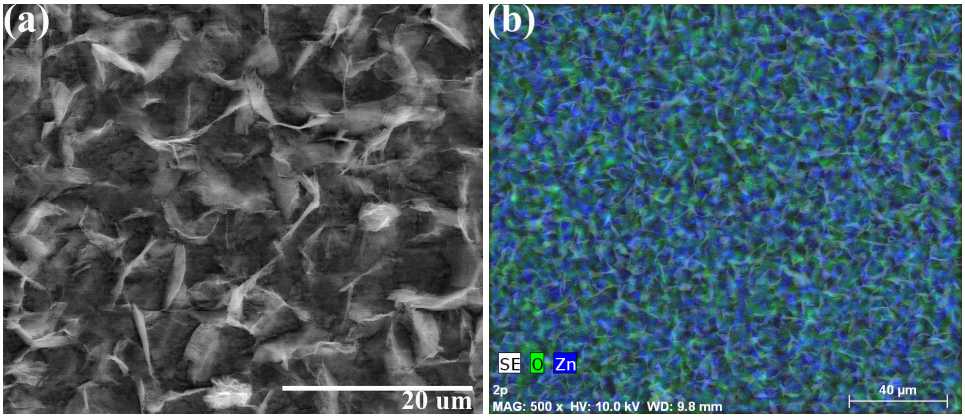

Fig. 3.36. SEM image at × 5000 magnification (a) and EDS map (b) of as-deposited 343 K and heat-treated at 873 K ZnO

Figure 3.37 presents the results of photovoltammetry characterization of ZnO coatings in the phosphate buffer solution (pH 11.5) because it positively affected the alkaline media for the water anodic oxidation and for the ZnO film stability. The obtained results confirm that the heat-treatment highly improves the photoelectrochemical activity of the as-deposited specimens. It is to note that the coatings electrodeposited at 343 K are characterized by higher photoactivity (more than 3 times) if compared to those prepared at 293 K. TEC 15 glass absorbs shorter than 300 nm light. Only negligible photocurrent was found to be generated by the SnO_2 layer under experimental conditions used in this thesis.

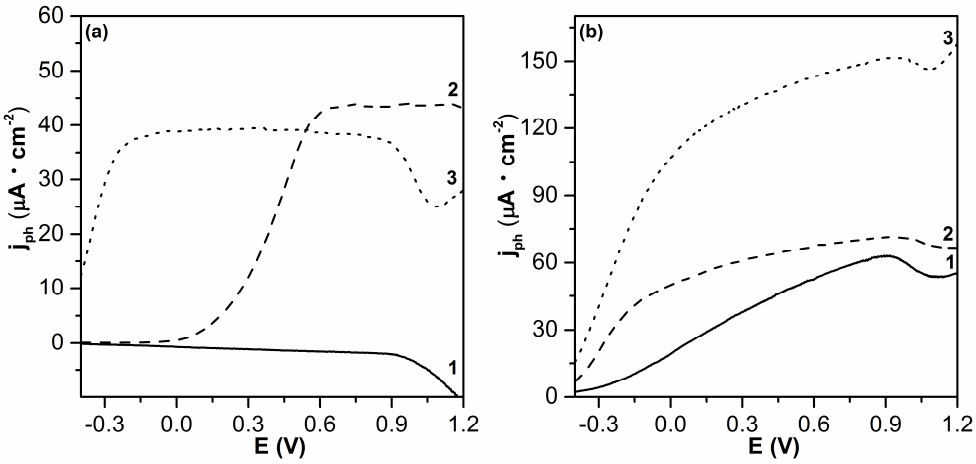

Fig. 3.37. Influence of heat-treatment on the generated current in the phosphate buffer solution (pH 11.5) of ZnO electrodeposited at 293 K (a) and 343 K (b): 1 – as-deposited; 2 – heat-treated at 673 K; 3 – heat-treated at 873 K

The results of the XRD analysis for Co coatings at 343 K with or without heat-treatment are shown in Figure 3.38 (a). The diffraction peaks in the as-deposited at 343 K sample (Fig. 3.38.(a); curve1) at 2θ of 33.06° and 59.06° are indexed to α-$Co(OH)_2$ (PDF 00-002-0925) and at 2θ of 19.66° related to β-modification (PDF 00-030-0443). After the heat treatment at 673 K and 873 K, more diffraction peaks were revealed: 2θ at 19.08°, 31.44°, 36.86°, 44.80°, 61.86° and 65.50° (Fig. 3.38. (a) curves 2 – 3). All the diffraction peaks in Figure 3.39. (a) 2 and 3 spectra are attributed to the spinel Co_3O_4 phase (PDF 01-078-5634) thus indicating that the crystalline Co_3O_4 was formed after the annealing treatment [160].

As-deposited at 343 K Co_3O_4 FT-IR spectra as well as in the case of ZnO, the data shows that acetate impurities stemming from the precursor are incorporated in the as-prepared coating structure (Fig. 3.38. (b); curve 1). After annealing at 673 K and 873 K (Fig. 3.38. (b); curves 2 – 3), the bands of the cobalt acetate precursor almost completely disappear (1 peak at 1385 cm^{-1} belonging to $\nu_s COO^-$ remains only) while two very strong peaks centered at 661 and 565 cm^{-1} characteristic of spinel Co_3O_4 are noticed. This is consistent with the XRD results. Heat-treatment at 873 K for 1 hour increases the Co_3O_4 peak intensity; therefore the cubic Co_3O_4 coating deposited under these conditions is of high-quality and well-crystallized.

The results of UV-vis diffuse reflectance spectroscopy (Fig. 3.39) also support the assumption that the as-deposited cobalt hydroxide is composed of both α and β phases. The presence of α phase is confirmed by the occurrence of the absorption band at around 490 nm [161]. The strong absorption peaks centered at 592 and 638 nm can be assigned to the presence of the β phase [161].

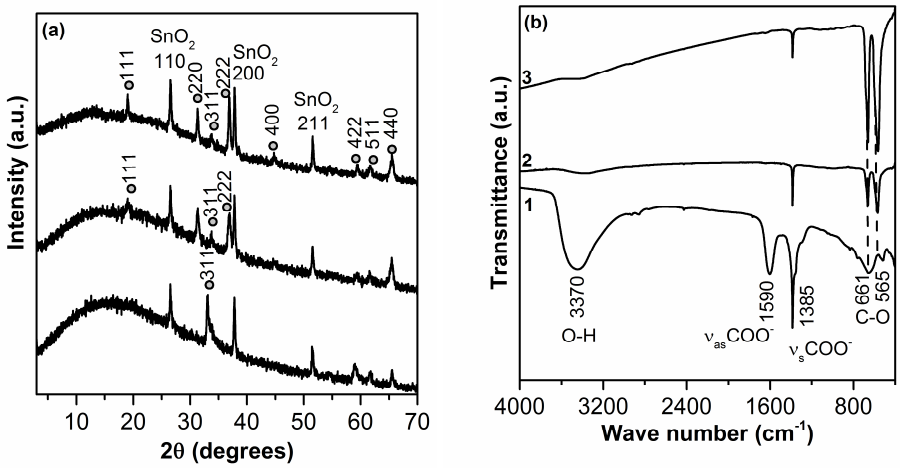

Fig. 3.38. XRD (a) and FT-IR (b) spectra of cobalt (hydr)oxide coatings: 1 – as-deposited at 343 K; 2 – heat-treated at 673 K for 1h; 3 – heat-treated at 873 K for 1 h.
Abbreviations: ○ –Co_3O_4; ★– $Co(OH)_2$

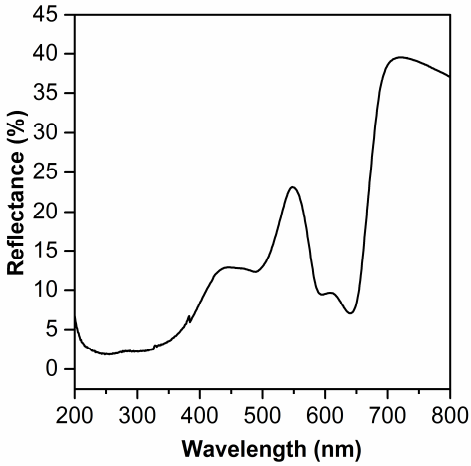

Fig. 3.39. UV-vis diffuse reflectance spectra of as-deposited cobalt hydroxide

Figure 3.40. (a) shows the SEM image of the as-deposited at 343 K and heat-treated at 873 K Co_3O_4 coating. The Co_3O_4 coating is formed from uniform cross-linked nanowalls standing vertically relative to the substrate. The EDS elemental map is shown in Figure 3.40. (b). The O and Co exhibit the same spatial distribution in the elemental map. As well as in the case of ZnO, it can be concluded that the Co_3O_4 coating is uniform and homogenous.

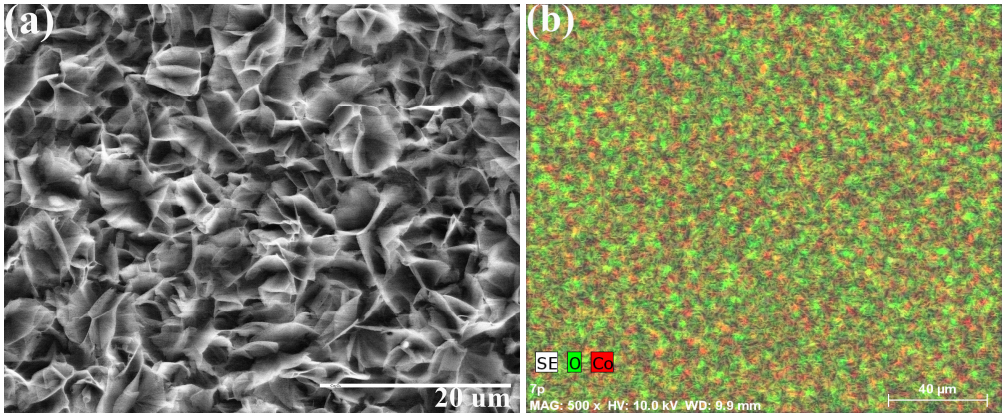

Fig. 3.40. SEM image at × 5000 magnification (a) and EDS map (b) of Co_3O_4 heat-treated at 873 K

3.3.2. Structure and properties of mixed Zn-Co oxide coatings

3.3.2.1. Structural and morphological characterization

Summarized XRD analysis results are described in Sections 3.2.1 and 3.3.1. On the grounds of the processed data it can be concluded that as-deposited at 293 K and 343 K Zn-Co oxide coatings contain intercalated impurities from zinc (PDF 00-056-0569) and cobalt (PDF 00-056-0568) acetates precursors (Fig. 3.41; curve 1). The heat-treatment at 673 K and 873 K eliminated the impurity peaks, increased the

product peak intensity and improved the quality of the coatings. On the grounds of the experimental results it can be stated that ZnO-$ZnCo_2O_4$ structure is formed in ZnCoO1, ZnCoO2 and ZnCoO3 coatings (Fig. 3.41. (a), (b), (c) curves 2 – 3) [162]. $ZnCo_2O_4$ structure (PDF 00-001-1149) is formed when zinc and cobalt concentration in the initial ZnCoO4 solution is 0.01 and 0.04 M (Fig. 3.41. (d); curves 2 – 3) [162, 163].

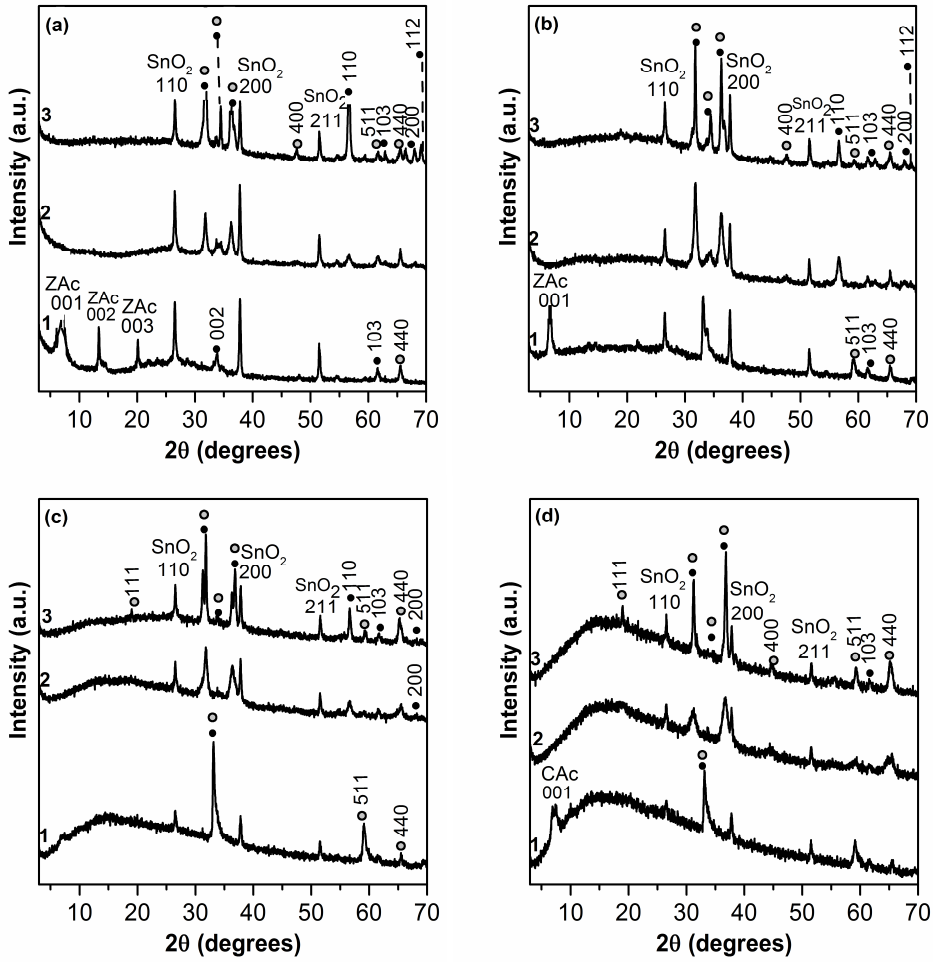

Fig. 3.41. XRD spectra of ZnCoO1 (a), ZnCoO2 (b), ZnCoO3 (c) and ZnCoO4 (d) coatings: 1 – as deposited at 343 K; 2 – heat-treated at 673 K for 1h; 3 – heat-treated at 873 K for 1 h. Abbreviations: CAc – $Co(CH_3COO)_2$; ZAc – $Zn(CH_3COO)_2$; ○ –Co_3O_4; ● – ZnO

FT-IR analysis confirmed that as-deposited at 293 K and 343 K Zn-Co oxide coatings structures contain intercalated impurities from the zinc and cobalt acetate precursors (Fig. 3.42.; curve 1) whereas the heat-treatment improves the quality of the coatings. Also, $ZnO\text{-}ZnCo_2O_4$ and $ZnCo_2O_4$ structure is confirmed by FT-IR analysis as well. In Figure 3.42., (a), (b), (c) FT-IR 2 and 3 spectra two peaks are seen at 455 cm^{-1} characteristic to ZnO and at 675 cm^{-1} characteristic to Co_3O_4. This indicates $ZnO\text{-}ZnCo_2O_4$ structure [162]. Figure 3.42. (d) presents curves 2 and 3 featuring characteristic spectra for the $ZnCo_2O_4$ structure [162, 163].

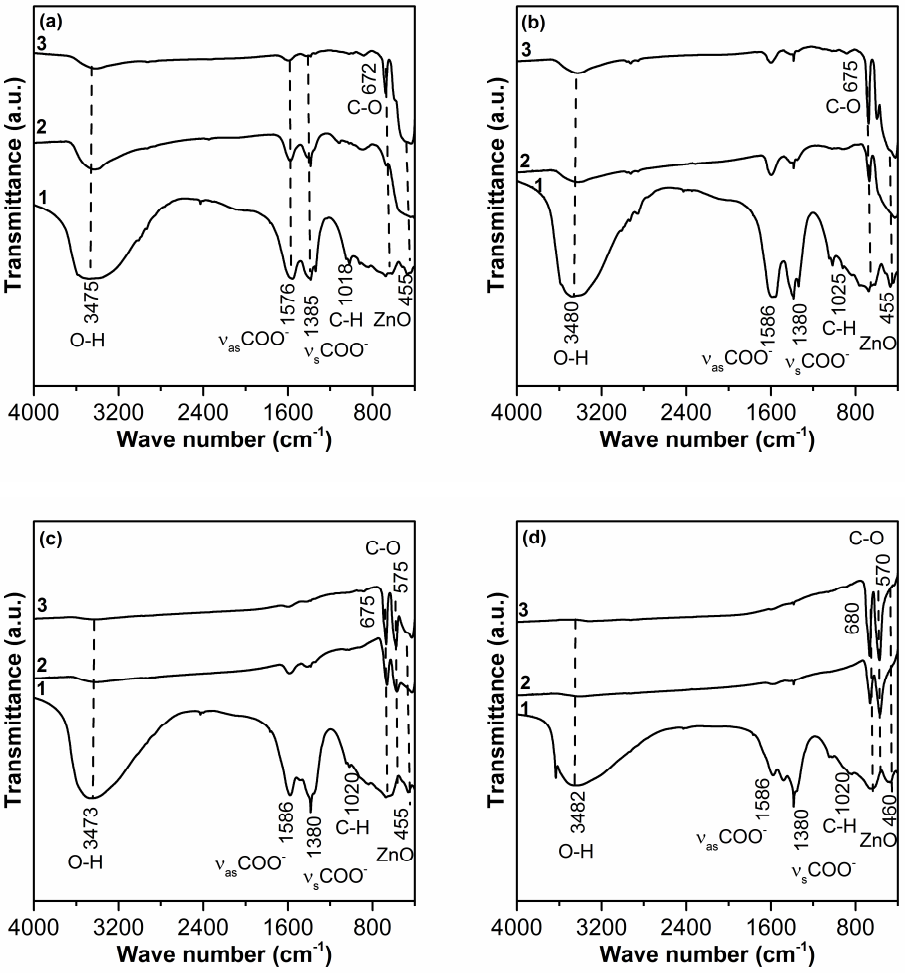

Fig. 3.42. FT-IR spectra of ZnCoO1 (a), ZnCoO2 (b), ZnCoO3 (c) and ZnCoO4 (d) coatings: 1 – as deposited at 343 K; 2 – heat-treated at 673 K for 1h; 3 – heat-treated at 873 K for 1 h

The results of UV-vis diffuse reflectance spectroscopy of as-deposited Zn-Co oxide coatings are presented in Figure 3.43. The absorption peak at ~319 nm for ZnCoO1 sample can be related to the presence of various impurities (e.g., acetate or nitrate) inserted into the coatings during the electrodeposition. In the visible region, the appearance of absorption peaks at around 488, 586 and 641 nm can be attributed to the transitions of Co^{2+} ions ($3d^7$) in tetrahedral coordination [164]. It is observed that the intensity of these peaks is increased with the increase of the cobalt content in the coatings.

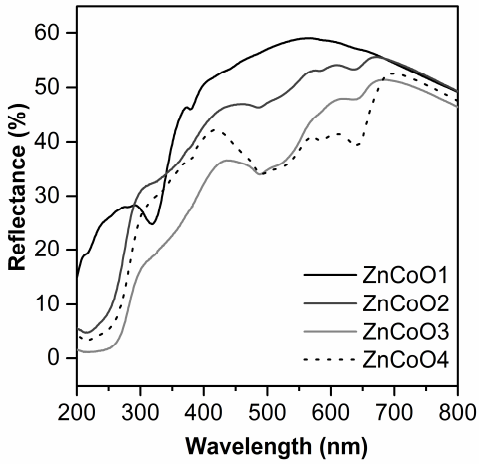

Fig. 3.43. UV-vis diffuse reflectance spectra of the coatings as-deposited at 343 K: 1 – ZnCoO1, 2 – ZnCoO2, 3 – ZnCoO3, 4 – ZnCoO4

Figure 3.44 presents the SEM images of as-deposited 343 K and heat-treated at 873 K Zn-Co oxide coatings. It shows that the ZnCoO1 coating is formed from tightly packed vertically oriented nanosheets. However, the cobalt concentration increase in the deposition electrolyte changes the structure of the coating: for ZnCoO1, ZnCoO2, ZnCoO3 coatings on vertically oriented ZnO nanosheets, $ZnCo_2O_4$ clusters are formed whereas for the ZnCoO4 coating, only $ZnCo_2O_4$ clusters are found. This data also is confirmed by XRD analysis (Fig. 3.41) and EDS mapping (Fig. 3.45).

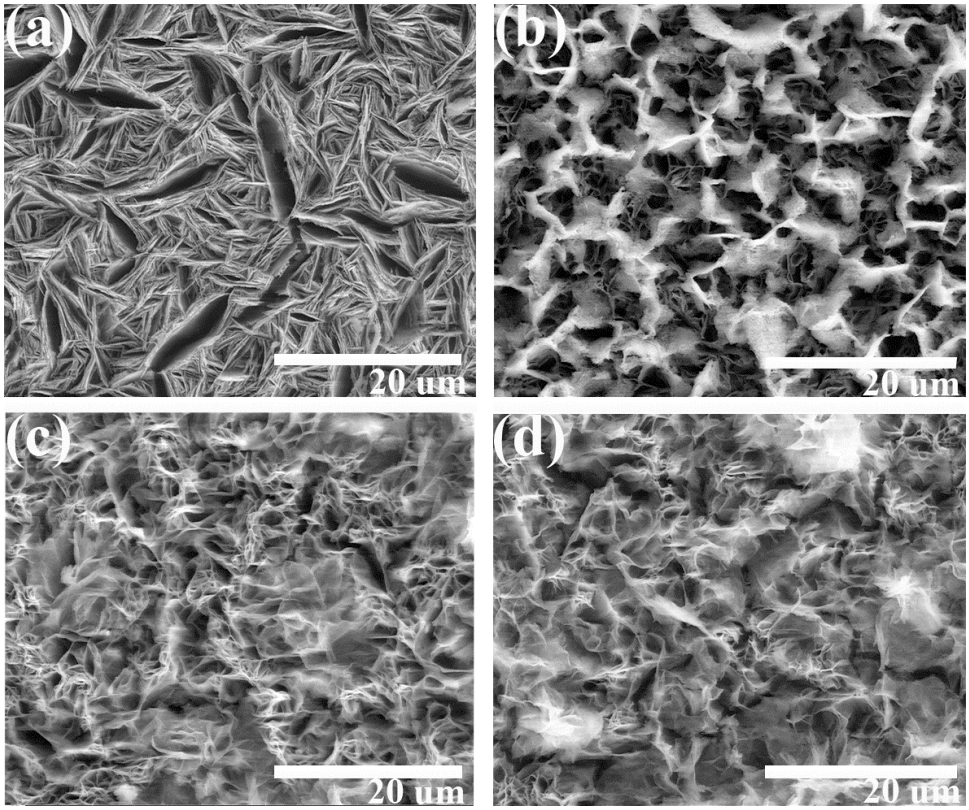

Fig. 3.44. SEM images at × 5000 magnification of coatings deposited at 343 K and heat-treated at 873 K: 1 – ZnCoO1, 2 – ZnCoO2, 3 – ZnCoO3, 4 – ZnCoO4

EDS spectra were used to evaluate the uniformity of the element distribution in mixed Zn-Co coatings. Figure3.45. shows the distribution of O, Zn, and Co, respectively. It is evident that both Co (on the surface) and Zn (in the inner layer of the coating) elements are distributed uniformly thus confirming that Co_3O_4 and ZnO are well-distributed in the nanocomposites, which will be beneficial for the charged carrier transfer between ZnO and Co_3O_4.

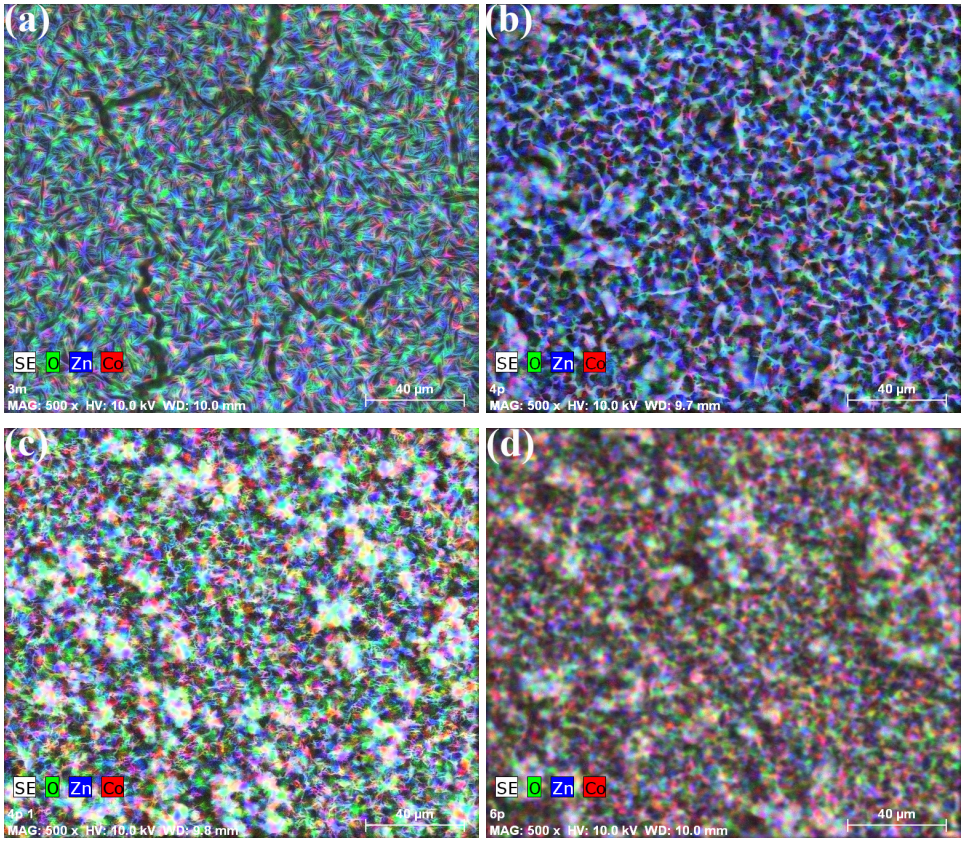

Fig. 3.45. EDS maps of coatings deposited at 343 K and heat-treated at 873 K: 1 – ZnCoO1, 2 – ZnCoO2, 3 – ZnCoO3, 4 – ZnCoO4

3.3.2.2. Electrochemical properties

The effect of the Zn/Co ratio on the photoelectrochemical properties of the prepared coatings was studied by measuring the current–potential characteristics under UV irradiation and in the dark. The photovoltammetry results showed that only as-deposited Zn-Co oxides are photoelectrochemically active (Fig. 3.46). The annealing of the coatings had a detrimental effect on their photoactivity, and the specimens heat-treated at 873 K were found to generate only negligible photocurrents (the results are not presented more explicitly here for the sake of brevity). The photocurrents are diminishing as the content of cobalt in the coatings is increasing. The strongest photocurrents are generated by ZnCoO1 coatings (up to 200 $\mu A \cdot cm^{-2}$ at 1 V potential). On the contrary, in the case of ZnCoO4 catalyst, the photoactivity is suppressed. In addition, the onset potential for the photocurrent is shifted to the positive direction if compared to bare ZnO coatings. These results suggest that the cobalt additive promotes the recombination of charge carriers reducing the observed photocurrents.

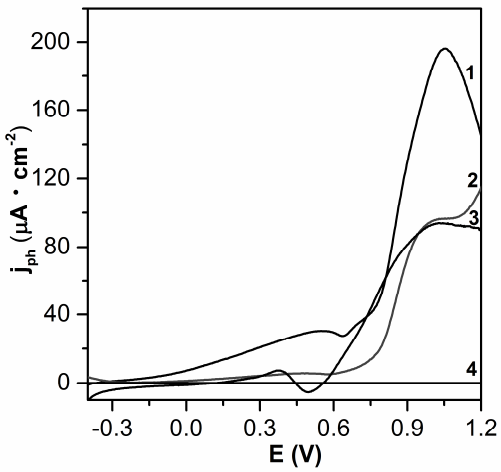

Fig. 3.46. Dependence of the photocurrent density j_{ph} on the applied potential E for as-deposited at 343 K mixed Zn-Co oxide in the phosphate buffer solution (pH 11.5): 1 – ZnCoO1, 2 – ZnCoO2, 3 – ZnCoO3, 4 – ZnCoO4.

In order to test the electrochemical performance of the coatings during the oxygen evolution reaction, the current-potential data was collected by conducting controlled potential electrolysis in the phosphate buffer solution (pH 11.5) with the application of various potentials. The electrolyte solution was continuously stirred, and the steady-state currents were measured at the applied potential which was being altered in 50 mV steps (Fig. 3.47.). After each measurement, the electrode was allowed to reach equilibrium with the electrolyte solution for at least 5 min at the open circuit potential. Only Zn-Co oxide samples thermally-treated at 873 K were used in the experiments due to their superior activity and stability. The collected current-potential data was used for the construction of Tafel plots (Fig. 3.49). The overpotential η was calculated according to the following equation:

$$\eta = E_{appl} - 0.35, \quad (3.19)$$

where E_{appl} is the applied potential (V) measured against Ag, AgCl | $KCl_{(sat)}$ reference electrode; 0.35 is the value of of the equilibrium potential against Ag, AgCl | $KCl_{(sat)}$ reference electrode for water oxidation at pH 11.5.

As it was pointed out in the review of the relevant scholarly writings (Section 1.3), the Tafel equation maintains fundamental importance in electrochemical kinetics for the formulation of quantitative relation between the current and the applied potential. The Tafel slope b is an indicative parameter of the electrode reaction mechanism.

The results presented in Figure 3.48 show that the increase in the cobalt content in the coatings results in the increase of their electrocatalytic activity due to the well-known electrocatalytic properties of cobalt oxides [16]. For example, the steady-state current for ZnCoO4 coating was found to be more than two times stronger if compared to the ZnCoO1 coating. In addition, the ZnCoO4 coating is

more active than Co_3O_4 which is known as an active electrocatalyst for water oxidation.

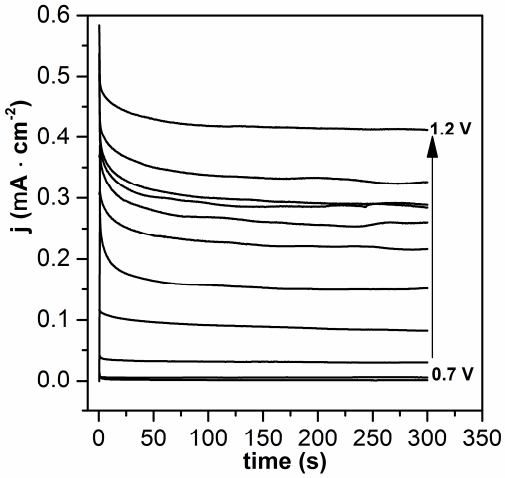

Fig. 3.47. Characteristic chronoamperograms obtained during the controlled potential electrolysis in the phosphate buffer solution (pH 11.5) using ZnCoO1 coating

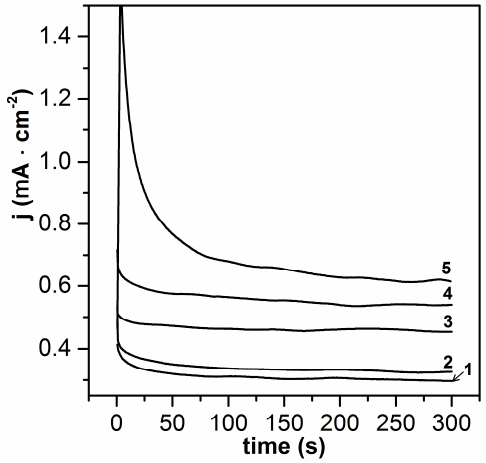

Fig. 3.48. Controlled potential electrolysis at 1.15 V of various coatings in the phosphate buffer solution (pH 11.5): 1 – ZnCoO1; 2 – ZnCoO2; 3 – ZnCoO3; 4 – Co_3O_4; 5 – ZnCoO4. All the coatings were heat-treated at 873 K for 1 h

Figure 3.49 presents the dependence of the overpotential as a function of logarithm of the current density for various electrodes. In all cases, an abrupt change of the Tafel slope is observed at overpotential values higher than 0.5 V. The switch of the Tafel slope can be considered as an indication of the change of the reaction mechanism. The following mechanism has been proposed for oxygen evolution reaction on oxide electrode materials [14]:

$$X + H_2O \rightarrow X\text{–}OH + H^+ + e^- \quad (3.20)$$

$$X\text{–}OH \rightarrow X\text{–}O + H^+ + e^- \quad (3.21)$$

$$2X\text{–}O \rightarrow 2X + O_2 \quad (3.22)$$

where X is the surface active site.

The first step is the discharge of either water (in an acid) or hydroxide (in a base); equation 3.20 corresponds to a Tafel slope of 120 mV. The second step involves electrochemical oxidation (eq. 3.21, 60 mV). Finally, oxygen is liberated from the reaction of two highly oxidized surface sites (eq. 3.22, 40 mV). Usually, two different Tafel slope values can be observed as a function of overpotential, namely, a lower slope (typically 40-60 mV) at low overpotentials, and a higher one (120 mV) at high overpotentials.

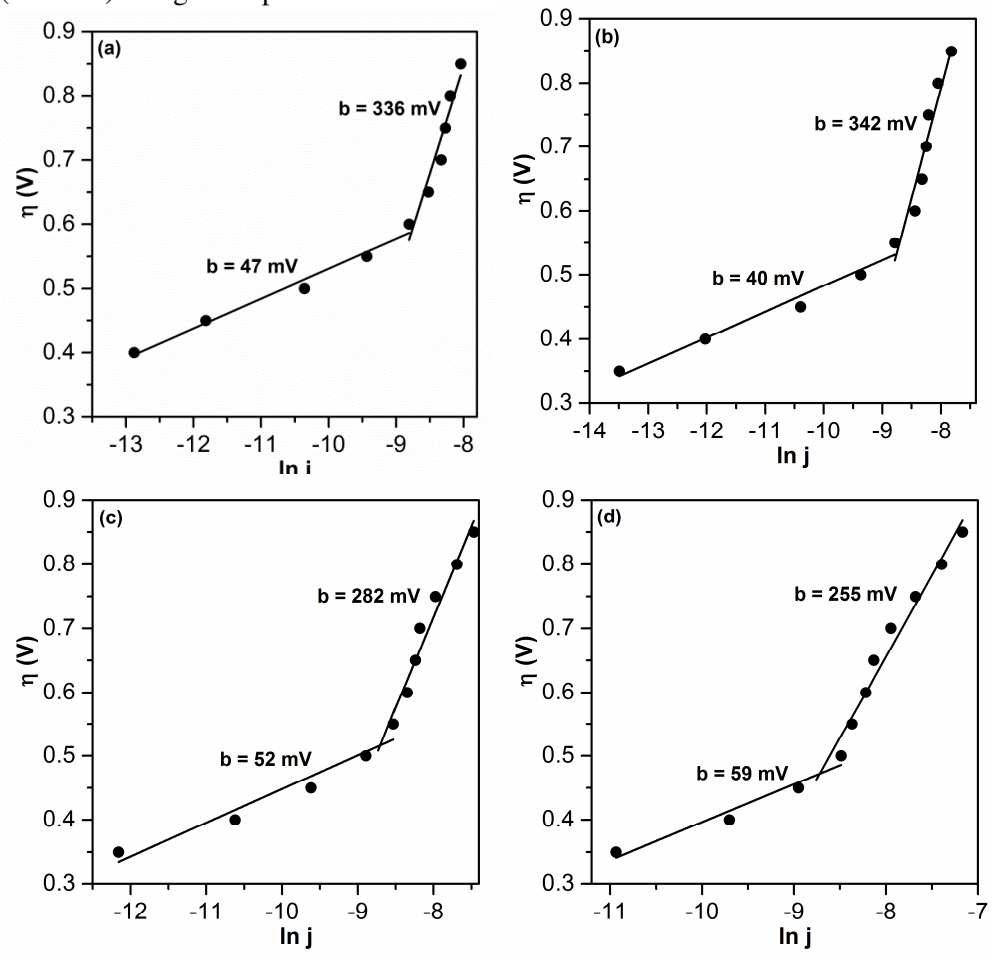

Fig. 3.49. Tafel plots for ZnCoO1 (a), ZnCoO2 (b), ZnCoO3 (c) and ZnCoO4 (d) coatings. The supporting electrolyte: 0.1 M phosphate buffer (pH 11.5). All the coatings were electrodeposited at 343 K and heat-treated at 873 K for 1 h

3.3.3. Influence of Co-P_i catalyst on electrochemical properties of ZnO and ZnCoO coatings

The results presented in Figures 3.48 and 3.49 revealed that the prepared ZnCoO coatings on TEC 15 glass are active electrocatalysts in the oxygen evolution reaction. On the other hand, the review of scholarly literature shows that the cobalt-phosphate (Co–P_i) compound is a very promising electrocatalyst of oxygen evolution. Taking into account these facts, the next step of this paper was the synthesis of ZnO/Co–P_i and ZnCoO/Co–P_i coatings.

Co–P_i catalyst was photochemically deposited according to the procedure presented in Section 2.2.2.3. ZnO and ZnCoO coatings heat-treated at 873 K were used as supports of the Co–P_i catalyst. SEM micrograph shows that the coating maintains a vertically orientated nanowall structure (Fig. 3.50. (a)). The Zn and Co–P_i structures exhibit the same spatial distribution in the elemental map, and Co–P_i profoundly interferes in the ZnO structure (Fig. 3.50. (b)).

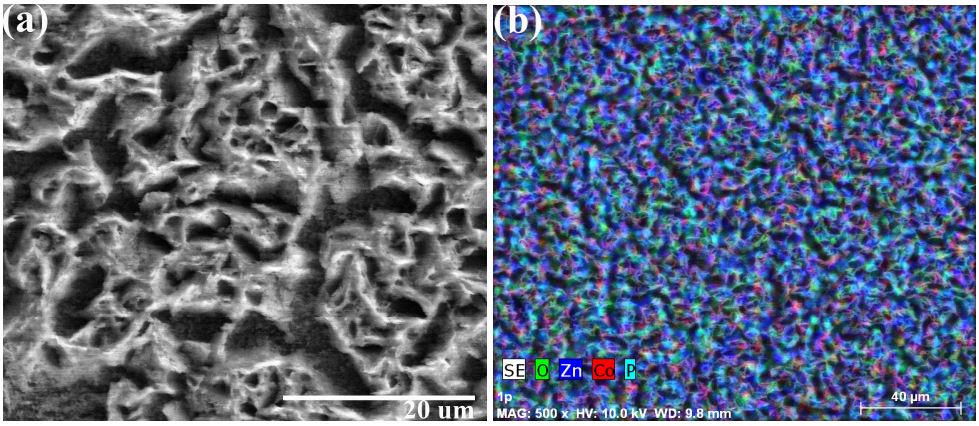

Fig. 3.50. SEM image at × 5000 magnification (a) and EDS map (b) of ZnO/ Co–P_i coating

Energy-dispersive X-ray analysis (EDX) identified that zinc, cobalt and oxygen are the main elemental components of the prepared coating (Fig. 3.51, Table 3.8.). In addition, phosphorus, carbon and potassium were also detected in the sample.

Table 3.8. Results of EDX characterization of ZnO/Co–P_i coating

Element	Quantity (at. %)
Carbon	1.01
Phosphorus	1.32
Potassium	3.22
Cobalt	12.68
Zinc	31.44
Oxygen	50.33

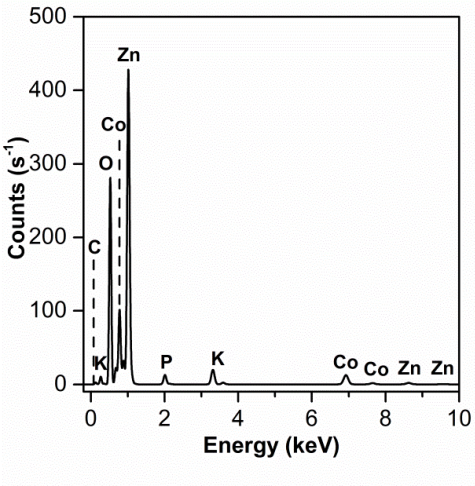

Fig. 3.51. Representative EDX spectrum of ZnO/Co–P_i catalyst

The voltammograms (Fig. 3.52) and the Tafel plots (Fig. 3.53) for the prepared ZnO/Co–P_i anodes confirmed that the presence of oxygen evolution catalyst greatly improves the activity of bare ZnO. The onset of the oxygen evolution reaction is shifted by about 0.3 V if compared to the ZnO anode. These results are in agreement with those presented in [22, 140].

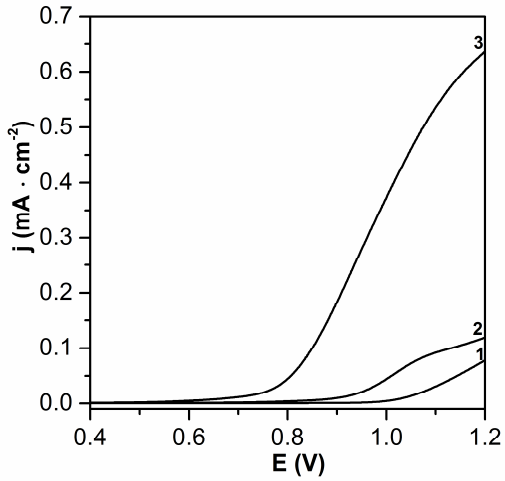

Fig. 3.52. Influence of the duration of photochemical deposition of Co–P_i on the electrochemical activity of ZnO in the phosphate buffer solution (pH 11.5) in the dark: 1 – 0 min; 2 – 5 min; 3 – 10 min. The potential scan rate is 10 mV · s^{-1}

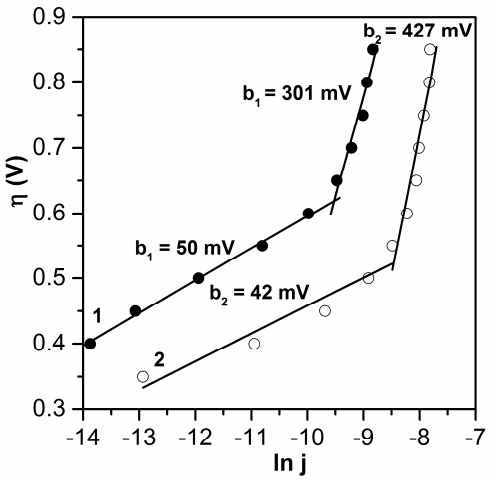

Fig. 3.53. Tafel plots for ZnO/Co–P_i coatings in the 0.1 M phosphate buffer (pH 11.5). The duration of the Co–P_i catalyst deposition (min): 1 – 5; 2 – 10

To the contrary, it was determined that the modification of mixed Zn-Co oxides with the Co–P_i catalyst does not lead to the enhancement of the observed currents. For example, in the case of ZnCoO1 catalyst, it was established that the increase in the Co–P_i amount results in the decrease of electroactivity (Fig. 3.54). Further studies including the detailed investigation of the contact $ZnCo_2O_4$/Co–P_i are needed in order to elucidate the observed phenomena.

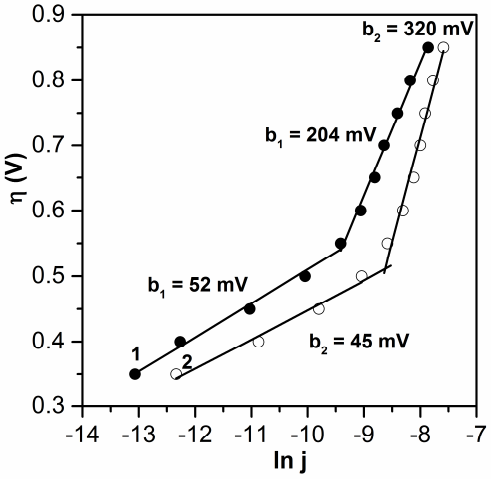

Fig. 3.54. Tafel plots for ZnCoO1/Co–P_i coatings in the 0.1 M phosphate buffer (pH 11.5). The duration of the Co–P_i catalyst deposition (min): 1 – 10 min; 2 – 5 min

CONCLUSIONS

1. Nanostructured ZnO coatings on AISI 304 stainless steel were formed by electrophoretic deposition. It was revealed that the highest stability and photoactivity in the 0.1 M Na_2SO_4 solution is characteristic for the coatings synthesized under the following conditions: the electrophoresis potential of 30 V, the deposition time of 10 min and the amount of immobilized ZnO is 1.03 $mg \cdot cm^{-2}$.
2. The electrochemical reduction of zinc(II) acetate on AISI 304 stainless steel results in the deposition of the wurtzite-type lamellar ZnO with the intercalated acetate ions. The heat-treatment at 673 K changes the ZnO coating morphology to the granular type and increases the photoactivity in the 0.1 M Na_2SO_4 electrolyte. It was confirmed that the presence of methanol increases the observed photocurrents.
3. It was determined that the potentiostatically deposited Zn-Co oxide coatings consist mainly of the lamellar ZnO and α-$Co(OH)_2$. After the heat-treatment at 673 K, Co_3O_4 and $ZnCo_2O_4$ spinel phases were identified to be formed.
4. The photoelectrochemical properties of the mixed Zn-Co oxide coatings depend on the Zn:Co ratio: the increase in the cobalt concentration decreases the observed photocurrents; yet it increases the specific capacitance.
5. The photoelectrochemical activity of the ZnO, Co_3O_4 and Zn-Co oxide coatings on the TEC 15 glass substrate for anodic water oxidation in 0.1 M phosphate buffer was compared. It was discovered that the highest electrocatalytic activity is exhibited by Zn-Co oxide samples at a ratio of Zn:Co = 0,28:1.
6. It was established that the increase in the amount of the Co–P_i catalyst decreases the observed photocurrent of the ZnO coatings; however it simultaneously increases the electrocatalytic activity of the anodic water oxidation. The Co–P_i catalyst exerts a small effect on the activity of mixed Zn–Co oxide coatings.

ACKNOWLEDGEMENTS

The writing of this dissertation is one of the most significant academic challenges I have ever had to face. Without the support, patience and guidance of my supervisor, the systematic help from my friends and maximum support from my family, this study would never have been completed. It is to them that I owe my deepest gratitude.

Firstly, I would like to express my sincere gratitude to prof. Eugenijus Valatka who undertook the duty of supervising my paper despite his countless academic and professional commitments. His wisdom, knowledge and devotion to the highest standards inspired and motivated me.

I would also like to thank a broad circle of my colleagues for their major contribution: Arūnas Baltušnikas for XRD spectra recording; Ina Liutvinienė for carrying out FT-IR spectra; Žaneta Rukuižienė for SEM and EDS analysis and Aurimas Urbutis for AAS analysis. My sincere thanks also go to Jonas Baltrušaitis for SEM, XPS and Raman analysis, for his help and support when contributing to the summarization of the results of the conducted analysis.

Special thanks are dedicated to my colleague and good friend Simona Ostachavičiūtė who has been with me whenever needed and managed to cool me down, to motivate me, to lift and boost my spirits to help me keep the work running. Thanks to my buddies Miglė Dagilienė and Sandra Kiseliovienė for all the 10 unforgettable years of friendship, assistance, encouragement and motivation. I also thank my fellow labmates Rasa Mardosaitė, Dovilė Sinkevičiūtė, Aurimas Urbutis and Nerita Žmuidzinavičienė for help, support and for all the fun we have been sharing in the last four years.

Last but not the least I would like to thank my family: my parents Janina Šulčienė and Algirdas Šulčius for bringing me up and for standing by me through the good and bad times not only while writing this thesis but also during all of my life in general. Thank You for always encouraging me and keeping faith in me.

Finally, I would like to thank my brother Mindaugas Šulčius and his wife Raminta Šulčienė. They were always right here cheering me up and supporting me spiritually throughout the process of writing this thesis and throughout my life in general.

A LIST OF REFERENCES

1. Pirkanniemi, K.; Sillanpää, M., Heterogeneous water phase catalysis as an environmental application: a review. *Chemosphere,* 2002, **48** (10), p. 1047-1060.
2. Al-Ekabi, H.; Serpone, N., Kinetics studies in heterogeneous photocatalysis. I. Photocatalytic degradation of chlorinated phenols in aerated aqueous solutions over titania supported on a glass matrix. *The Journal of Physical Chemistry,* 1988, **92** (20), p. 5726-5731.
3. Pouretedal, H. R.; Sabzevari, S., Photodegradation study of congo red, methyl orange, methyl red and methylene blue under simulated solar irradiation catalyzed by ZnS/CdS nanocomposite. *Desalination and Water Treatment,* 2011, **28** (1-3), p. 247-254.
4. Ohtani, B., Photocatalysis by inorganic solid materials: revisiting its definition, concepts, and experimental procedures. *Advances in Inorganic Chemistry,* 2011, **63**, p. 395-430.
5. van de Krol, R.; Grätzel, M., Photoelectrochemical Hydrogen Production. Boston, MA: Springer US, 2012, p. 321.
6. Tong, H.; Ouyang, S. X.; Bi, Y. P.; Umezawa, N.; Oshikiri, M.; Ye, J. H., Nano-photocatalytic materials: possibilities and challenges. *Advanced Materials,* 2012, **24** (2), p. 229-251.
7. Linsebigler, A. L.; Lu, G. Q.; Yates, J. T., Photocatalysis on TiO_2 surfaces - principles, mechanisms, and selected results. *Chemical Reviews,* 1995, **95** (3), p. 735-758.
8. Yerga, R. M. N.; Galvan, M. C. A.; del Valle, F.; de la Mano, J. A. V.; Fierro, J. L. G., Water splitting on semiconductor catalysts under visible-light irradiation. *Chemsuschem,* 2009, **2** (6), p. 471-485.
9. Yang, J.; Wang, D.; Han, H.; Li, C., Roles of cocatalysts in photocatalysis and photoelectrocatalysis. *Accounts of Chemical Research,* 2013, **46** (8), p. 1900-1909.
10. Kudo, A., Photocatalysis and solar hydrogen production. *Pure and Applied Chemistry,* 2007, **79** (11), p. 1917-1927.
11. Trotochaud, L.; Boettcher, S. W., Precise oxygen evolution catalysts: status and opportunities. *Scripta Materialia,* 2014, **74** (0), p. 25-32.
12. Rajeshwar, K.; McConnell, R.; Licht, S., Solar Hydrogen Generation: Toward a Renewable Energy Future. Springer, 2008, p. 338.
13. Albright's Chemical Engineering Handbook. Boca Raton: CRC Press, 2008, p. 1928.
14. Walter, M. G.; Warren, E. L.; McKone, J. R.; Boettcher, S. W.; Mi, Q. X.; Santori, E. A.; Lewis, N. S., Solar water splitting cells. *Chemical Reviews,* 2010, **110** (11), p. 6446-6473.
15. Trasatti, S., Transition metal oxides: versatile materials for electrocatalysis. Electrochemistry of novel materials. New York: VCH Publishers Inc, 1994, p. 88.
16. Steinmiller, E. M. P.; Choi, K.-S., Photochemical deposition of cobalt-based oxygen evolving catalyst on a semiconductor photoanode for solar oxygen production. *Proceedings of the National Academy of Sciences,* 2009, **106** (49), p. 20633-20636.
17. Surendranath, Y.; Nocera, D. G., Oxygen evolution reaction chemistry of oxide-based electrodes. Progress in Inorganic Chemistry, New York: John Wiley & Sons, Inc., 2011, p. 505-560.
18. Lee, Y.; Suntivich, J.; May, K. J.; Perry, E. E.; Shao-Horn, Y., Synthesis and activities of rutile IrO_2 and RuO_2 nanoparticles for oxygen evolution in acid and alkaline solutions. *The Journal of Physical Chemistry Letters,* 2012, **3** (3), p. 399-404.
19. Esswein, A. J.; McMurdo, M. J.; Ross, P. N.; Bell, A. T.; Tilley, T. D., Size-dependent activity of Co_3O_4 nanoparticle anodes for alkaline water electrolysis. *The Journal of Physical Chemistry C,* 2009, **113** (33), p. 15068-15072.
20. Kanan, M. W.; Nocera, D. G., In situ formation of an oxygen-evolving catalyst in neutral water containing phosphate and Co^{2+}. *Science,* 2008, **321** (5892), p. 1072-1075.

21. Surendranath, Y.; Kanan, M. W.; Nocera, D. G., Mechanistic studies of the oxygen evolution reaction by a cobalt-phosphate catalyst at neutral pH. *Journal of the American Chemical Society,* 2010, **132** (46), p. 16501-16509.
22. Wang, Y.; Wang, Y.; Jiang, R.; Xu, R., Cobalt phosphate–ZnO composite photocatalysts for oxygen evolution from photocatalytic water oxidation. *Industrial & Engineering Chemistry Research,* 2012, **51** (30), p. 9945-9951.
23. Khnayzer, R. S.; Mara, M. W.; Huang, J.; Shelby, M. L.; Chen, L. X.; Castellano, F. N., Structure and activity of photochemically deposited "CoPi" oxygen evolving catalyst on titania. *ACS Catalysis,* 2012, **2** (10), p. 2150-2160.
24. Seabold, J. A.; Choi, K.-S., Effect of a cobalt-based oxygen evolution catalyst on the sStability and the selectivity of photo-oxidation reactions of a WO_3 photoanode. *Chemistry of Materials,* 2011, **23** (5), p. 1105-1112.
25. Dinca, M.; Surendranath, Y.; Nocera, D. G., Nickel-borate oxygen-evolving catalyst that functions under benign conditions. *Proceedings of the National Academy of Sciences of the United States of America,* 2010, **107** (23), p. 10337-10341.
26. Morkoç, H.; Özgür, Ü., Zinc Oxide. Fundamentals, materials and device technology. Weinheim: WILEY-VCH Verlag GmbH & Co. KGaA, 2009, p. 488.
27. Klingshirn, C., ZnO: material, physics and applications. *Chemphyschem,* 2007, **8** (6), p. 782-803.
28. Özgür, Ü.; Alivov, Y. I.; Liu, C.; Teke, A.; Reshchikov, M. A.; Doğan, S.; Avrutin, V.; Cho, S. J.; Morkoç, H., A comprehensive review of ZnO materials and devices. *Journal of Applied Physics,* 2005, **98** (4), p. 041301-041404.
29. Moezzi, A.; McDonagh, A. M.; Cortie, M. B., Zinc oxide particles: synthesis, properties and applications. *Chemical Engineering Journal,* 2012, **185–186** (0), p. 1-22.
30. Kolodziejczak-Radzimska, A.; Jesionowski, T.; Maciejewska, M.; Zaborski, M., Modified and unmodified zinc oxide as coagent in elastomer compounds. *Polish Journal of Chemical Technology,* 2014, **16** (3), p. 63-68.
31. Liu, Y.; Gorla, C. R.; Liang, S.; Emanetoglu, N.; Lu, Y.; Shen, H.; Wraback, M., Ultraviolet detectors based on epitaxial ZnO films grown by MOCVD. *Journal of Electronic Materials,* 2000, **29** (1), p. 69-74.
32. Ataev, B. M.; Bagamadova, A. M.; Mamedov, V. V.; Omaev, A. K.; Rabadanov, M. R., Highly conductive and transparent thin ZnO films prepared in situ in a low pressure system. *Journal of Crystal Growth,* 1999, **198–199, Part 2** (0), p. 1222-1225.
33. Kaiya, K.; Omichi, K.; Takahashi, N.; Nakamura, T.; Okamoto, S.; Yamamoto, H., Epitaxial growth of ZnO thin films exhibiting room-temperature ultraviolet emission by atmospheric pressure chemical vapor deposition. *Thin Solid Films,* 2002, **409** (1), p. 116-119.
34. Kashiwaba, Y.; Haga, K.; Watanabe, H.; Zhang, B. P.; Segawa, Y.; Wakatsuki, K., Structures and photoluminescence properties of ZnO films epitaxially grown by atmospheric pressure MOCVD. *physica status solidi (b),* 2002, **229** (2), p. 921-924.
35. Kim, K.-K.; Song, J.-H.; Jung, H.-J.; Choi, W.-K.; Park, S.-J.; Song, J.-H., The grain size effects on the photoluminescence of ZnO/α-Al_2O_3 grown by radio-frequency magnetron sputtering. *Journal of Applied Physics,* 2000, **87** (7), p. 3573-3575.
36. Cheng, J. P.; Guo, R. Y.; Wang, Q. M., Zinc oxide single-crystal microtubes. *Applied Physics Letters,* 2004, **85** (22), p. 5140-5142.
37. Fouad, O. A.; Ismail, A. A.; Zaki, Z. I.; Mohamed, R. M., Zinc oxide thin films prepared by thermal evaporation deposition and its photocatalytic activity. *Applied Catalysis B: Environmental,* 2006, **62** (1–2), p. 144-149.
38. Barnes, T. M.; Leaf, J.; Fry, C.; Wolden, C. A., Room temperature chemical vapor deposition of c-axis ZnO. *Journal of Crystal Growth,* 2005, **274** (3-4), p. 412-417.

39. Lee, J.-H.; Ko, K.-H.; Park, B.-O., Electrical and optical properties of ZnO transparent conducting films by the sol–gel method. *Journal of Crystal Growth,* 2003, **247** (1–2), p. 119-125.
40. Escobedo Morales, A.; Herrera Zaldivar, M.; Pal, U., Indium doping in nanostructured ZnO through low-temperature hydrothermal process. *Optical Materials,* 2006, **29** (1), p. 100-104.
41. Yan, Z.; Song, Z. T.; Liu, W. L.; Wan, Q.; Zhang, F. M.; Feng, S. L., Optical and electrical properties of p-type zinc oxide thin films synthesized by ion beam assisted deposition. *Thin Solid Films,* 2005, **492** (1–2), p. 203-206.
42. Kim, H. Y.; Kim, J. H.; Park, M. O.; Im, S., Photoelectric, stoichiometric and structural properties of n-ZnO film on p-Si. *Thin Solid Films,* 2001, **398–399** (0), p. 93-98.
43. Fiddes, A. J. C.; Durose, K.; Brinkman, A. W.; Woods, J.; Coates, P. D.; Banister, A. J., Preparation of ZnO films by spray pyrolysis. *Journal of Crystal Growth,* 1996, **159** (1–4), p. 210-213.
44. Ohgaki, T.; Ohashi, N.; Kakemoto, H.; Wada, S.; Adachi, Y.; Haneda, H.; Tsurumi, T., Growth condition dependence of morphology and electric properties of ZnO films on sapphire substrates prepared by molecular beam epitaxy. *Journal of Applied Physics,* 2003, **93** (4), p. 1961-1965.
45. Nakahara, K.; Takasu, H.; Fons, P.; Iwata, K.; Yamada, A.; Matsubara, K.; Hunger, R.; Niki, S., Growth and characterization of undoped ZnO films for single crystal based device use by radical source molecular beam epitaxy (RS-MBE). *Journal of Crystal Growth,* 2001, **227–228** (0), p. 923-928.
46. Yue, S.; Yan, Z.; Shi, Y.; Ran, G., Synthesis of zinc oxide nanotubes within ultrathin anodic aluminum oxide membrane by sol–gel method. *Materials Letters,* 2013, **98** (0), p. 246-249.
47. Schneider, J. J.; Hoffmann, R. C.; Engstler, J.; Klyszcz, A.; Erdem, E.; Jakes, P.; Eichel, R.-A.; Pitta-Bauermann, L.; Bill, J., Synthesis, characterization, defect chemistry, and FET properties of microwave-derived nanoscaled zinc oxide. *Chemistry of Materials,* 2010, **22** (7), p. 2203-2212.
48. Corni, I.; Ryan, M. P.; Boccaccini, A. R., Electrophoretic deposition: from traditional ceramics to nanotechnology. *Journal of the European Ceramic Society,* 2008, **28** (7), p. 1353-1367.
49. Hara, Y.; Brownson, J. R. S.; Anderson, M. A., Fabrication of thin-films composed of ZnO nanorods using electrophoretic deposition. *International Journal of Applied Ceramic Technology,* 2012, **9** (1), p. 115-123.
50. Wong, E. M.; Searson, P. C., Kinetics of electrophoretic deposition of zinc oxide quantum particle thin films. *Chemistry of Materials,* 1999, **11** (8), p. 1959-1961.
51. Tang, F.; Sakka, Y.; Uchikoshi, T., Electrophoretic deposition of aqueous nano-sized zinc oxide suspensions on a zinc electrode. *Materials Research Bulletin,* 2003, **38** (2), p. 207-212.
52. Tang, F.; Uchikoshi, T.; Sakka, Y., Electrophoretic deposition behavior of aqueous nanosized zinc oxide suspensions. *Journal of the American Ceramic Society,* 2002, **85** (9), p. 2161-2165.
53. Wang, Y. C.; Leu, I. C.; Hon, M. H., Preparation and characterization of nanosized ZnO arrays by electrophoretic deposition. *Journal of Crystal Growth,* 2002, **237–239** (0), p. 564-568.
54. Wang, Y. C.; Leu, I. C.; Hon, M. H., Effect of colloid characteristics on the fabrication of ZnO nanowire arrays by electrophoretic deposition. *Journal of Materials Chemistry,* 2002, **12** (8), p. 2439-2444.

55. Wu, K. M.; Zhitomirsky, I., Electrophoretic deposition of ceramic nanoparticles. *International Journal of Applied Ceramic Technology,* 2011, **8** (4), p. 920-927.
56. Chen, H.-W.; Lin, C.-Y.; Lai, Y.-H.; Chen, J.-G.; Wang, C.-C.; Hu, C.-W.; Hsu, C.-Y.; Vittal, R.; Ho, K.-C., Electrophoretic deposition of ZnO film and its compression for a plastic based flexible dye-sensitized solar cell. *Journal of Power Sources,* 2011, **196** (10), p. 4859-4864.
57. Yin, X.; Liu, X.; Wang, L.; Liu, B., Electrophoretic deposition of ZnO photoanode for plastic dye-sensitized solar cells. *Electrochemistry Communications,* 2010, **12** (9), p. 1241-1244.
58. Miao, L.; Cai, S.; Xiao, Z., Preparation and characterization of nanostructured ZnO thin film by electrophoretic deposition from ZnO colloidal suspensions. *Journal of Alloys and Compounds,* 2010, **490** (1–2), p. 422-426.
59. Lee, J. H.; Leu, I. C.; Chung, Y. W.; Hon, M. H., Fabrication of ordered ZnO hierarchical structures controlled via surface charge in the electrophoretic deposition process. *Nanotechnology,* 2006, **17** (17), p. 4445-4450.
60. Verde, M.; Caballero, A. C.; Iglesias, Y.; Villegas, M.; Ferrari, B., Electrophoretic deposition of flake-shaped ZnO nanoparticles. *Journal of the Electrochemical Society,* 2010, **157** (1), p. H55-H59.
61. Verde, M.; Peiteado, M.; Caballero, A. C.; Villegas, M.; Ferrari, B., Electrophoretic deposition of transparent ZnO thin films from highly stabilized colloidal suspensions. *Journal of Colloid and Interface Science,* 2012, **373** (1), p. 27-33.
62. Boccaccini, A. R.; Zhitomirsky, I., Application of electrophoretic and electrolytic deposition techniques in ceramics processing. *Current Opinion in Solid State & Materials Science,* 2002, **6** (3), p. 251-260.
63. Wu, X. J.; Zhu, F.; Mu, C.; Liang, Y. Q.; Xu, L. F.; Chen, Q. W.; Chen, R. Z.; Xu, D. S., Electrochemical synthesis and applications of oriented and hierarchically quasi-1D semiconducting nanostructures. *Coordination Chemistry Reviews,* 2010, **254** (9-10), p. 1135-1150.
64. Therese, G. H. A.; Kamath, P. V., Electrochemical synthesis of metal oxides and hydroxides. *Chemistry of Materials,* 2000, **12** (5), p. 1195-1204.
65. Peulon, S.; Lincot, D., Cathodic electrodeposition from aqueous solution of dense or open-structured zinc oxide films. *Advanced Materials,* 1996, **8** (2), p. 166-&.
66. Gan, X.; Li, X.; Gao, X.; He, X.; Zhuge, F., Deposition potential dependence of ZnO–eosin Y hybrid thin films prepared by electrochemical deposition and their photoelectrochemical properties. *Materials Chemistry and Physics,* 2009, **114** (2–3), p. 920-925.
67. Weng, J.; Zhang, Y.; Han, G.; Zhang, Y.; Xu, L.; Xu, J.; Huang, X.; Chen, K., Electrochemical deposition and characterization of wide band semiconductor ZnO thin film. *Thin Solid Films,* 2005, **478** (1–2), p. 25-29.
68. Wang, F.; Liu, R.; Pan, A.; Cao, L.; Cheng, K.; Xue, B.; Wang, G.; Meng, Q.; Li, J.; Li, Q.; Wang, Y.; Wang, T.; Zou, B., The optical properties of ZnO sheets electrodeposited on ITO glass. *Materials Letters,* 2007, **61** (10), p. 2000-2003.
69. Mahalingam, T.; John, V. S.; Raja, M.; Su, Y. K.; Sebastian, P. J., Electrodeposition and characterization of transparent ZnO thin films. *Solar Energy Materials and Solar Cells,* 2005, **88** (2), p. 227-235.
70. Wellings, J. S.; Chaure, N. B.; Heavens, S. N.; Dharmadasa, I. M., Growth and characterisation of electrodeposited ZnO thin films. *Thin Solid Films,* 2008, **516** (12), p. 3893-3898.
71. Liu, Z.; E, L.; Ya, J.; Xin, Y., Growth of ZnO nanorods by aqueous solution method with electrodeposited ZnO seed layers. *Applied Surface Science,* 2009, **255** (12), p. 6415-6420.

72. Gür, E.; Asıl, H.; Coşkun, C.; Tüzemen, S.; Meral, K.; Onganer, Y.; Şerifoğlu, K., Optical and structural properties of ZnO thin films; effects of high energy electron irradiation and annealing. *Nuclear Instruments and Methods in Physics Research Section B: Beam Interactions with Materials and Atoms,* 2008, **266** (9), p. 2021-2026.
73. Ramírez, D.; Silva, D.; Gómez, H.; Riveros, G.; Marotti, R. E.; Dalchiele, E. A., Electrodeposition of ZnO thin films by using molecular oxygen and hydrogen peroxide as oxygen precursors: Structural and optical properties. *Solar Energy Materials and Solar Cells,* 2007, **91** (15–16), p. 1458-1461.
74. Lee, M.-K.; Tu, H.-F., Optical emissions of Zn and ZnO in Zn-ZnO structure synthesized by electrodeposition with aqueous solution of zinc nitrate-6-hydrate. *Crystal Growth & Design,* 2008, **8** (6), p. 1785-1788.
75. Tena-Zaera, R.; Elias, J.; Lévy-Clément, C.; Mora-Seró, I.; Luo, Y.; Bisquert, J., Electrodeposition and impedance spectroscopy characterization of ZnO nanowire arrays. *physica status solidi (a),* 2008, **205** (10), p. 2345-2350.
76. Leprince-Wang, Y.; Yacoubi-Ouslim, A.; Wang, G. Y., Structure study of electrodeposited ZnO nanowires. *Microelectronics Journal,* 2005, **36** (7), p. 625-628.
77. Dimova-Malnovska, D.; Andreev, P.; Sendova-Vassileva, M.; Nichev, H.; Starbova, K., Preparation of ZnO nanowires by electrochemical deposition. *Energy Procedia,* 2010, **2** (1), p. 55-58.
78. Fahoume, M.; Maghfoul, O.; Aggour, M.; Hartiti, B.; Chraïbi, F.; Ennaoui, A., Growth and characterization of ZnO thin films prepared by electrodeposition technique. *Solar Energy Materials and Solar Cells,* 2006, **90** (10), p. 1437-1444.
79. Jamali Sheini, F.; Mulla, I. S.; Joag, D. S.; More, M. A., Influence of process variables on growth of ZnO nanowires by cathodic electrodeposition on zinc substrate. *Thin Solid Films,* 2009, **517** (24), p. 6605-6611.
80. Lupan, O.; Pauporté, T.; Chow, L.; Viana, B.; Pellé, F.; Ono, L. K.; Roldan Cuenya, B.; Heinrich, H., Effects of annealing on properties of ZnO thin films prepared by electrochemical deposition in chloride medium. *Applied Surface Science,* 2010, **256** (6), p. 1895-1907.
81. Pauporté, T.; Lincot, D., Hydrogen peroxide oxygen precursor for zinc oxide electrodeposition II—Mechanistic aspects. *Journal of Electroanalytical Chemistry,* 2001, **517** (1–2), p. 54-62.
82. Guo, M.; Yang, C.; Zhang, M.; Zhang, Y.; Ma, T.; Wang, X.; Wang, X., Effects of preparing conditions on the electrodeposition of well-aligned ZnO nanorod arrays. *Electrochimica Acta,* 2008, **53** (14), p. 4633-4641.
83. Pauporté, T.; Jirka, I., A method for electrochemical growth of homogeneous nanocrystalline ZnO thin films at room temperature. *Electrochimica Acta,* 2009, **54** (28), p. 7558-7564.
84. Karuppuchamy, S.; Ito, S., Cathodic electrodeposition of nanoporous ZnO thin films from new electrochemical bath and their photoinduced hydrophilic properties. *Vacuum,* 2008, **82** (5), p. 547-550.
85. Lee, K. K.; Chin, W. S.; Sow, C. H., Cobalt-based compounds and composites as electrode materials for high-performance electrochemical capacitors. *Journal of Materials Chemistry A,* 2014, **2** (41), p. 17212-17248.
86. Zou, W. Q.; Mo, Z. R.; Lu, Z. L.; Lu, Z. H.; Zhang, F. M.; Du, Y. W., Magnetic and optical properties of $Zn_{1-x}Co_xO$ thin films prepared by plasma enhanced chemical vapor deposition. *Physica B: Condensed Matter,* 2008, **403** (19–20), p. 3686-3688.
87. Sharma, V. K.; Najim, M.; Srivastava, A. K.; Varma, G. D., Structural and magnetic studies on transition metal (Mn, Co) doped ZnO nanoparticles. *Journal of Magnetism and Magnetic Materials,* 2012, **324** (5), p. 683-689.

88. Nair, M. G.; Nirmala, M.; Rekha, K.; Anukaliani, A., Structural, optical, photo catalytic and antibacterial activity of ZnO and Co doped ZnO nanoparticles. *Materials Letters,* 2011, **65** (12), p. 1797-1800.
89. Godlewski, M.; Lukasiewicz, M. I.; Guziewicz, E.; Ivanov, V. Y.; Owczarczyk, L.; Witkowski, B. S., Optical and magnetic properties of ZnCoO layers. *Optical Materials,* 2012, **34** (12), p. 2045-2049.
90. Colis, S.; Bieber, H.; Begin-Colin, S.; Schmerber, G.; Leuvrey, C.; Dinia, A., Magnetic properties of Co-doped ZnO diluted magnetic semiconductors prepared by low-temperature mechano synthesis. *Chemical Physics Letters,* 2006, **422** (4-6), p. 529-533.
91. Jayakumar, O. D.; Sudakar, C.; Gopalakrishnan, I. K., Surfactant-assisted synthesis of $Zn_{0.95}Co_{0.05}O$ and $Zn_{0.85}Co_{0.05}Li_{0.10}O$ nanoparticles showing room temperature ferromagnetism. *Journal of Crystal Growth,* 2008, **310** (13), p. 3251-3255.
92. Guo, H. X.; Chen, J. H.; Weng, W.; Wang, Q. X.; Li, S. X., Facile template-free one-pot fabrication of $ZnCo_2O_4$ microspheres with enhanced photocatalytic activities under visible-light illumination. *Chemical Engineering Journal,* 2014, **239**, p. 192-199.
93. Belghazi, Y.; Aouaj, M. A.; El Yadari, M.; Schmerber, G.; Ulhaq-Bouillet, C.; Leuvrey, C.; Colis, S.; Abd-lefdil, M.; Berrada, A.; Dinia, A., Elaboration and characterization of Co-doped ZnO thin films deposited by spray pyrolysis technique. *Microelectronics Journal,* 2009, **40** (2), p. 265-267.
94. Reddy, K. T. R.; Supriya, V.; Murata, Y.; Sugiyama, M., Effect of Co-doping on the properties of $Zn_{1-x}Co_xO$ films deposited by spray pyrolysis. *Surface & Coatings Technology,* 2013, **231**, p. 149-152.
95. Chi, B.; Li, J. B.; Yang, X. Z.; Lin, H.; Wang, N., Electrophoretic deposition of $ZnCo_2O_4$ spinel and its electrocatalytic properties for oxygen evolution reaction. *Electrochimica Acta,* 2005, **50** (10), p. 2059-2064.
96. Li, J. J.; Zhang, L. T.; Zhu, J. B.; Liu, Y.; Hao, W. C., Controllable synthesis of $Zn_{0.95}Co_{0.05}O$ nanowires and nanotubes by electrophoretic deposition method. *Transactions of Nonferrous Metals Society of China,* 2012, **22**, p. S95-S99.
97. Bouloudenine, M.; Viart, N.; Colis, S.; Dinia, A., $Zn_{1-x}Co_xO$ diluted magnetic semiconductors synthesized under hydrothermal conditions. *Catalysis Today,* 2006, **113** (3-4), p. 240-244.
98. Zhu, G. X.; Xu, H.; Liu, Y. J.; Xu, X.; Ji, Z. Y.; Shen, X. P.; Xu, Z., Enhanced gas sensing performance of Co-doped ZnO hierarchical microspheres to 1,2-dichloroethane. *Sensors and Actuators B-Chemical,* 2012, **166**, p. 36-43.
99. Straumal, B. B.; Mazilkin, A. A.; Protasova, S. G.; Myatiev, A. A.; Straumal, P. B.; Baretzky, B., Increase of Co solubility with decreasing grain size in ZnO. *Acta Materialia,* 2008, **56** (20), p. 6246-6256.
100. Pivin, J. C.; Socol, G.; Mihailescu, I.; Berthet, P.; Singh, F.; Patel, M. K.; Vincent, L., Structure and magnetic properties of ZnO films doped with Co, Ni or Mn synthesized by pulsed laser deposition under low and high oxygen partial pressures. *Thin Solid Films,* 2008, **517** (2), p. 916-922.
101. Zhang, L. Q.; Ye, Z. Z.; Lu, B.; Lu, J. G.; He, H. P.; Zhang, Y. Z.; Zhu, L. P.; Jiang, J.; Wu, K. W.; He, B., Fabrication and properties of Li-doped ZnCoO diluted magnetic semiconductor thin films. *Superlattices and Microstructures,* 2011, **50** (3), p. 261-268.
102. Xu, X. H.; Qin, X. F.; Jiang, F. X.; Li, X. L.; Chen, Y.; Gehring, G. A., The dopant concentration and annealing temperature dependence of ferromagnetism in Co-doped ZnO thin films. *Applied Surface Science,* 2008, **254** (16), p. 4956-4960.
103. El Mir, L.; Ben Ayadi, Z.; Rahmouni, H.; El Ghoul, J.; Djessas, K.; von Bardeleben, H. J., Elaboration and characterization of Co doped, conductive ZnO thin films deposited by

radio-frequency magnetron sputtering at room temperature. *Thin Solid Films,* 2009, **517** (21), p. 6007-6011.
104. Sati, P.; Schafer, S.; Morhain, C.; Deparis, C.; Stepanov, A., Magnetic properties of single crystalline $Zn_{1-x}Co_xO$ thin films. *Superlattices and Microstructures,* 2007, **42** (1-6), p. 191-196.
105. Lu, Z. L.; Bian, X. F.; Zou, W. Q.; Xu, M. X.; Zhang, F. M., The origin of ferromagnetism in Co-doped ZnO single crystalline films upon reducing annealings. *Journal of Alloys and Compounds,* 2010, **492** (1-2), p. 31-34.
106. Wei, L.; Li, Z. H.; Zhang, W. F., Influence of Co doping content on its valence state in $Zn_{1-x}Co_xO$ ($0 <= x <= 0.15$) thin films. *Applied Surface Science,* 2009, **255** (9), p. 4992-4995.
107. Heiba, Z. K.; Arda, L., XRD, XPS, optical, and Raman investigations of structural changes of nano Co-doped ZnO. *Journal of Molecular Structure,* 2012, **1022**, p. 167-171.
108. El Manouni, A.; Tortosa, M.; Manjon, F. J.; Mollar, M.; Mari, B.; Sanchez-Royo, J. F., Effect of annealing on $Zn_{1-x}Co_xO$ thin films prepared by electrodeposition. *Microelectronics Journal,* 2009, **40** (2), p. 268-271.
109. Cao, P.; Zhao, D. X.; Zhang, J. Y.; Shen, D. Z.; Lu, Y. M.; Fan, X. W.; Wang, X. H., N-doping-related room temperature ferromagnetism of electrodeposited ZnCoO films. *Physica B-Condensed Matter,* 2007, **392** (1-2), p. 255-258.
110. Jaramillo, T. F.; Baeck, S. H.; Kleiman-Shwarsctein, A.; Choi, K. S.; Stucky, G. D.; McFarland, E. W., Automated electrochemical synthesis and photoelectrochemical characterization of $Zn_{1-x}Co_xO$ thin films for solar hydrogen production. *Journal of Combinatorial Chemistry,* 2005, **7** (2), p. 264-271.
111. Wang, Y. X.; Ding, X.; Cheng, Y.; Zhang, Y. J.; Yang, L. L.; Liu, H. L.; Fan, H. G.; Liu, Y.; Yang, J. H., Properties of Co-doped ZnO films prepared by electrochemical deposition. *Crystal Research and Technology,* 2009, **44** (5), p. 517-520.
112. Bazuev, G. V.; Gyrdasova, O. I.; Grigorov, I. G.; Koryakova, O. V., Preparation of $ZnCo_2O_4$ spinel whiskers from zinc cobalt oxalate. *Inorganic Materials,* 2005, **41** (3), p. 288-292.
113. Kim, T. W.; Woo, M. A.; Regis, M.; Choi, K.-S., Electrochemical synthesis of spinel type $ZnCo_2O_4$ electrodes for use as oxygen evolution reaction catalysts. *The Journal of Physical Chemistry Letters,* 2014, **5** (13), p. 2370-2374.
114. Lin, C.-C.; Li, Y.-Y., Synthesis of ZnO nanowires by thermal decomposition of zinc acetate dihydrate. *Materials Chemistry and Physics,* 2009, **113** (1), p. 334-337.
115. Azároff, L. V., Elements of X-ray crystallography. New York: McGraw-Hill Book Company, 1968, p. 576.
116. Baltrusaitis, J.; Usher, C. R.; Grassian, V. H., Reactions of sulfur dioxide on calcium carbonate single crystal and particle surfaces at the adsorbed water carbonate interface. *Physical Chemistry Chemical Physics,* 2007, **9** (23), p. 3011-3024.
117. Shakti, N.; Gupta, P. S., Structural properties and photoluminescence of ZnO thin film and nanowires. *Optoelectronics and Advanced Materials-Rapid Communications,* 2010, **4** (5), p. 662-664.
118. Valatka, E.; Kulesius, Z., TiO_2-mediated photoelectrochemical decoloration of methylene blue in the presence of peroxodisulfate. *Journal of Applied Electrochemistry,* 2007, **37** (4), p. 415-420.
119. Georgieva, J.; Armyanov, S.; Valova, E.; Poulios, I.; Sotiropoulos, S., Enhanced photocatalytic activity of electrosynthesised tungsten trioxide–titanium dioxide bi-layer coatings under ultraviolet and visible light illumination. *Electrochemistry Communications,* 2007, **9** (3), p. 365-370.

120. Gupta, V.; Kusahara, T.; Toyama, H.; Gupta, S.; Miura, N., Potentiostatically deposited nanostructured alpha-$Co(OH)_2$: A high performance electrode material for redox-capacitors. *Electrochemistry Communications,* 2007, **9** (9), p. 2315-2319.
121. Duan, Y.; Li, J.; Yang, X.; Hu, L.; Wang, Z.; Liu, Y.; Wang, C., Kinetic analysis on the non-isothermal dehydration by integral master-plots method and TG–FTIR study of zinc acetate dihydrate. *Journal of Analytical and Applied Pyrolysis,* 2008, **83** (1), p. 1-6.
122. Meyers, R. A., Encyclopedia of Analytical Chemistry. New York: John Wiley & Sons, 2012, p. 2188.
123. Ishioka, T.; Shibata, Y.; Takahashi, M.; Kanesaka, I.; Kitagawa, Y.; Nakamura, K. T., Vibrational spectra and structures of zinc carboxylates I. Zinc acetate dihydrate. *Spectrochimica Acta Part a-Molecular and Biomolecular Spectroscopy,* 1998, **54** (12), p. 1827-1835.
124. Vahur, S.; Teearu, A.; Leito, I., ATR-FT-IR spectroscopy in the region of 550-230 cm^{-1}) for identification of inorganic pigments. *Spectrochimica Acta Part a-Molecular and Biomolecular Spectroscopy,* 2010, **75** (3), p. 1061-1072.
125. Besra, L.; Liu, M., A review on fundamentals and applications of electrophoretic deposition (EPD). *Progress in Materials Science,* 2007, **52** (1), p. 1-61.
126. Rajeshwar, K., Fundamentals of Semiconductor Electrochemistry and Photoelectrochemistry. Encyclopedia of Electrochemistry. Weinheim: WILEY-VCH Verlag GmbH & Co. KGaA, 2007, p. 586.
127. Domenech, X.; Ayllon, J. A.; Peral, J., H_2O_2 formation from photocatalytic processes at the ZnO/water interface. *Environmental Science and Pollution Research,* 2001, **8** (4), p. 285-287.
128. Spathis, P.; Poulios, I., The corrosion and photocorrosion of zinc and zinc-oxide coatings. *Corrosion Science,* 1995, **37** (5), p. 673-680.
129. Betova, I.; Bojinov, M.; Laitinen, T.; Makela, K.; Pohjanne, P.; Saario, T., The transpassive dissolution mechanism of highly alloyed stainless steels I. Experimental results and modelling procedure. *Corrosion Science,* 2002, **44** (12), p. 2675-2697.
130. Solarska, R.; Rutkowska, I.; Morand, R.; Augustynski, J., Photoanodic reactions occurring at nanostructured titanium dioxide films. *Electrochimica Acta,* 2006, **51** (11), p. 2230-2236.
131. Wang, H. H.; Xie, C. S.; Zeng, D. W., Controlled growth of ZnO by adding H_2O. *Journal of Crystal Growth,* 2005, **277** (1-4), p. 372-377.
132. Canava, B.; Lincot, D., Nucleation effects on structural and optical properties of electrodeposited zinc oxide on tin oxide. *Journal of Applied Electrochemistry,* 2000, **30** (6), p. 711-716.
133. Inamdar, A. I.; Sonavane, A. C.; Sharma, S. K.; Im, H.; Patil, P. S., Nanocrystalline zinc oxide thin films by novel double pulse single step electrodeposition. *Journal of Alloys and Compounds,* 2010, **495** (1), p. 76-81.
134. Palms, D.; Norwig, J.; Wegner, G., Electrochemically induced growth of zinc oxide. *Chemphyschem,* 2007, **8** (15), p. 2260-2264.
135. Georgieva, J.; Armyanov, S.; Valova, E.; Tsacheva, T.; Poulios, I.; Sotiropoulos, S., Photoelectrochemical behaviour of electrodeposited tungsten trioxide and electrosynthesised titanium dioxide single component and bilayer coatings on stainless steel substrates. *Journal of Electroanalytical Chemistry,* 2005, **585** (1), p. 35-43.
136. Lachheb, H.; Puzenat, E.; Houas, A.; Ksibi, M.; Elaloui, E.; Guillard, C.; Herrmann, J. M., Photocatalytic degradation of various types of dyes (alizarin S, crocein orange G, methyl red, congo red, methylene blue) in water by UV-irradiated titania. *Applied Catalysis B-Environmental,* 2002, **39** (1), p. 75-90.

137. Villarreal, T. L.; Gómez, R.; Neumann-Spallart, M.; Alonso-Vante, N.; Salvador, P., Semiconductor photooxidation of pollutants dissolved in water: a kinetic model for distinguishing between direct and indirect interfacial hole transfer. I. Photoelectrochemical experiments with polycrystalline anatase electrodes under current doubling and absence of recombination. *The Journal of Physical Chemistry B,* 2004, **108** (39), p. 15172-15181.
138. Hykaway, N.; Sears, W. M.; Morisaki, H.; Morrison, S. R., Current-doubling reactions on titanium dioxide photoanodes. *The Journal of Physical Chemistry,* 1986, **90** (25), p. 6663-6667.
139. Turchi, C. S.; Ollis, D. F., Photocatalytic degradation of organic-water contaminants - mechanisms involving hydroxyl radical attack. *Journal of Catalysis,* 1990, **122** (1), p. 178-192.
140. Ostachavičiūtė, S. *Synthesis, structure and activity of WO_3, Se-WO_3 and TiO_2/WO_3 photocatalysts*. PhD thesis summary, 2014, KTU: Kaunas.
141. Rajamathi, M.; Kamath, P. V.; Seshadri, R., Chemical synthesis of alpha-cobalt hydroxide. *Materials Research Bulletin,* 2000, **35** (2), p. 271-278.
142. Zhu, Y. C.; Li, H. L.; Koltypin, Y.; Gedanken, A., Preparation of nanosized cobalt hydroxides and oxyhydroxide assisted by sonication. *Journal of Materials Chemistry,* 2002, **12** (3), p. 729-733.
143. Schumacher, L. C.; Holzhueter, I. B.; Hill, I. R.; Dignam, M. J., Semiconducting and electrocatalytic properties of sputtered cobalt oxide-films. *Electrochimica Acta,* 1990, **35** (6), p. 975-984.
144. Alim, K. A.; Fonoberov, V. A.; Shamsa, M.; Balandin, A. A., Micro-Raman investigation of optical phonons in ZnO nanocrystals. *Journal of Applied Physics,* 2005, **97** (12), p. 124313-124318.
145. Wang, X. F.; Xu, J. B.; Yu, X. J.; Xue, K.; Yu, J. G.; Zhao, X. J., Structural evidence of secondary phase segregation from the Raman vibrational modes in $Zn_{1-x}Co_xO$ ($0 < x < 0.6$). *Applied Physics Letters,* 2007, **91** (3), p. 031908-031911.
146. Windisch, C. F.; Exarhos, G. J.; Owings, R. R., Vibrational spectroscopic study of the site occupancy distribution of cations in nickel cobalt oxides. *Journal of Applied Physics,* 2004, **95** (10), p. 5435-5442.
147. Christoskova, S.; Stoyanova, M.; Georgieva, M.; Mehandjiev, D., Preparation and characterization of a higher cobalt oxide. *Materials Chemistry and Physics,* 1999, **60** (1), p. 39-43.
148. Biesinger, M. C.; Payne, B. P.; Grosvenor, A. P.; Lau, L. W. M.; Gerson, A. R.; Smart, R. S., Resolving surface chemical states in XPS analysis of first row transition metals, oxides and hydroxides: Cr, Mn, Fe, Co and Ni. *Applied Surface Science,* 2011, **257** (7), p. 2717-2730.
149. Baltrusaitis, J.; Jayaweera, P. M.; Grassian, V. H., XPS study of nitrogen dioxide adsorption on metal oxide particle surfaces under different environmental conditions. *Physical Chemistry Chemical Physics,* 2009, **11** (37), p. 8295-8305.
150. Baltrusaitis, J.; Cwiertny, D. M.; Grassian, V. H., Adsorption of sulfur dioxide on hematite and goethite particle surfaces. *Physical Chemistry Chemical Physics,* 2007, **9** (41), p. 5542-5554.
151. Chambers, S. A.; Droubay, T.; Kaspar, T. C.; Gutowski, M., Experimental determination of valence band maxima for $SrTiO_3$, TiO_2, and SrO and the associated valence band offsets with Si(001). *Journal of Vacuum Science & Technology B,* 2004, **22** (4), p. 2205-2215.
152. Joshi, A. G.; Sahai, S.; Gandhi, N.; Krishna, Y. G. R.; Haranath, D., Valence band and core-level analysis of highly luminescent ZnO nanocrystals for designing ultrafast optical sensors. *Applied Physics Letters,* 2010, **96** (12), p. 123102-123117.

153. Qiao, L.; Xiao, H. Y.; Meyer, H. M.; Sun, J. N.; Rouleau, C. M.; Puretzky, A. A.; Geohegan, D. B.; Ivanov, I. N.; Yoon, M.; Weber, W. J.; Biegalski, M. D., Nature of the band gap and origin of the electro-/photo-activity of Co_3O_4. *Journal of Materials Chemistry C,* 2013, **1** (31), p. 4628-4633.
154. Zhou, G.; Zhu, J.; Chen, Y.; Mei, L.; Duan, X.; Zhang, G.; Chen, L.; Wang, T.; Lu, B., Simple method for the preparation of highly porous $ZnCo_2O_4$ nanotubes with enhanced electrochemical property for supercapacitor. *Electrochimica Acta,* 2014, **123** (0), p. 450-455.
155. Kelpsaite, I.; Baltrusaitis, J.; Valatka, E., Electrochemical deposition of porous cobalt oxide films on AISI 304 type steel. *Materials Science-Medziagotyra,* 2011, **17** (3), p. 236-243.
156. Wang, G.; Zhang, L.; Zhang, J., A review of electrode materials for electrochemical supercapacitors. *Chemical Society Reviews,* 2012, **41** (2), p. 797-828.
157. Zhang, Y.; Zhu, F.; Zhang, J. X.; Xia, L. L., Converting layered zinc acetate nanobelts to one-dimensional structured ZnO nanoparticle aggregates and their photocatalytic activity. *Nanoscale Research Letters,* 2008, **3** (6), p. 201-204.
158. Lin, H.; Huang, C. P.; Li, W.; Ni, C.; Shah, S. I.; Tseng, Y.-H., Size dependency of nanocrystalline TiO_2 on its optical property and photocatalytic reactivity exemplified by 2-chlorophenol. *Applied Catalysis B: Environmental,* 2006, **68** (1–2), p. 1-11.
159. Amin, M.; Manzoor, U.; Islam, M.; Bhatti, A. S.; Shah, N. A., Synthesis of ZnO nanostructures for low temperature CO and UV sensing. *Sensors,* 2012, **12** (10), p. 13842-13851.
160. Rai, A. K.; Gim, J.; Anh, L. T.; Kim, J., Partially reduced Co_3O_4/graphene nanocomposite as an anode material for secondary lithium ion battery. *Electrochimica Acta,* 2013, **100** (0), p. 63-71.
161. Ma, R.; Liu, Z.; Takada, K.; Fukuda, K.; Ebina, Y.; Bando, Y.; Sasaki, T., Tetrahedral Co(II) coordination in α-type cobalt hydroxide: rietveld refinement and X-ray absorption spectroscopy. *Inorganic Chemistry,* 2006, **45** (10), p. 3964-3969.
162. Na, C. W.; Woo, H.-S.; Kim, H.-J.; Jeong, U.; Chung, J.-H.; Lee, J.-H., Controlled transformation of ZnO nanobelts into CoO/Co_3O_4 nanowires. *CrystEngComm,* 2012, **14** (10), p. 3737-3741.
163. Hu, L. L.; Qu, B. H.; Li, C. C.; Chen, Y. J.; Mei, L.; Lei, D. N.; Chen, L. B.; Li, Q. H.; Wang, T. H., Facile synthesis of uniform mesoporous $ZnCo_2O_4$ microspheres as a high-performance anode material for Li-ion batteries. *Journal of Materials Chemistry A,* 2013, **1** (18), p. 5596-5602.
164. Djaja, N. F.; Montja, D. A.; Saleh, R., The effect of Co incorporation into ZnO nanoparticles. *Advances in Materials Physics and Chemistry,* 2013, **3** (1), p. 33-41.

LIST OF PUBLICATIONS AND PROCEEDINGS ON THE THEME OF DISSERTATION

Publications corresponding to the list of Thomson Reuters™ Web of Science database

1. Šulčiūtė, Agnė; Valatka, Eugenijus. Electrodeposition and photoelectrocatalytic activity of ZnO films on AISI 304 type steel // Materials science = Medžiagotyra / Kaunas University of Technology, Academy of Sciences of Lithuania. Kaunas: KTU. ISSN 1392-1320. 2012, Vol. 18, no. 4, p. 318-324.
2. Ivanauskas, Algimantas; Šulčiūtė, Agnė; Valatka, Eugenijus. Photoelectrochemical activity of electrophoretically deposited zinc oxide coatings on stainless steel substrates // Chemija. Vilnius: Lithuanian Academy of Sciences. ISSN 0235-7216. 2013, Vol.24, No. 2, p. 97-102.
3. Šulčiūtė, Agnė; Jonas, Baltrušaitis; Valatka, Eugenijus. Structure, morphology and electrochemical properties of zinc-cobalt oxide films on AISI 304 type steel // Journal of applied electrochemistry. Dordrecht: Springer. ISSN 0021-891X. 2015, Vol. 45, iss. 5, p. 405-417. DOI: 10.1007/s10800-015-0802-7.

Articles in the Lithuanian Journals Approved by the Department of Science and Studies

1. Šulčiūtė, Agnė; Valatka, Eugenijus. Cinko–kobalto oksidinių dangų sintezė, sudėtis ir fotoelektrocheminis aktyvumas // Cheminė technologija / Kauno technologijos universitetas. Kaunas: Technologija. ISSN 1392-1231. 2011, Nr. 1-2(57), p. 23-30.

Publications in Proceedings of Conferences

1. Šulčiūtė, Agnė; Valatka, Eugenijus. ZnO dangų ant nerūdijančio plieno sintezė, struktūra ir fotoelektrocheminės savybės // Neorganinių junginių chemija ir technologija = Chemistry and Technology of Inorganic Compounds: konferencijos pranešimų medžiaga / Kauno technologijos universitetas. Kaunas: Technologija, 2011. ISBN 9789955259817. P. 44.
2. Kelpšaitė, Ieva; Mockūnaitė, Silvija; Ostachavičiūtė, Simona; Šulčiūtė, Agnė; Valatka, Eugenijus. Synthesis, structure and photocatalytic activity of some mixed metal oxides // Chemistry 2011 : abstracts of the 10th international conference of Lithuanian chemists, Vilnius, 14-15 October, 2011 / Lithuanian Academy of Sciences, Vilnius University, Institute of Chemistry. Vilnius: Lietuvos mokslų akademijos leidykla, 2011. ISBN 9789955634652. P. 67.
3. Ivanauskas, Algimantas; Šulčiūtė, Agnė; Valatka, Eugenijus. Photoelectrochemical activity of electrophoretically deposited zinc oxide // Neorganinių junginių chemija ir technologija = Chemistry and Technology of Inorganic Compounds: konferencijos pranešimų medžiaga / Kauno technologijos universitetas. Kaunas: Technologija, 2012. ISSN 2029-9222. P. 90-95.
4. Šulčiūtė, Agnė; Valatka, Eugenijus. Structure and electrochemical properties of mixed cobalt-zinc oxide films // Nanochemistry and nanomaterials: international conference of young chemists, 7-9 December 2012, Palanga, Lithuania: conference program and book of abstracts / Vilnius University. Faculty of Chemistry. Vilnius: Vilniaus universitetas, 2012. ISBN 9786094591389. P. 49.
5. Šulčiūtė, Agnė; Valatka, Eugenijus. Capacitive properties and structural characterization of Zn-Co-O films. // Chemistry and chemical technology of inorganic materials :

proceedings of scientific conference chemistry and chemical technology / Kaunas university of technology. Kaunas: Technologija. 2013. ISSN 2029-9222. P. 114-118.
6. Šulčiūtė, Agnė; Valatka, Eugenijus. Photoelectrochemical properties of ZnO films modified by cobalt-based catalyst // EcoBalt 2013: 18th international scientific conference, October 25-27, 2013 Vilnius, Lithuania: book of abstracts. Vilnius: Vilniaus universiteto leidykla, 2013. ISBN 9786094592416. P. 100.
7. Mardosaitė, Rasa; Ostachavičiūtė, Simona; Šulčiūtė, Agnė; Valatka, Eugenijus. Influence of a cobalt-based oxygen evolving catalyst on the photoactivity of semiconductor photoanodes // International Conference of Lithuanian Chemical Society: Chemistry and Chemical Technology, Kaunas, 25 April, 2014, Lithuania / Chemistry and Chemical Technology: Proceedings of the International conference. Kaunas: Technologija, 2014. ISSN 2351-5643. P. 156.

SL344. 2016-01-05, 11,75 leidyb. apsk. l. Tiražas 10 egz. Užsakymas 1.

Išleido Kauno technologijos universitetas, K. Donelaičio g. 73, 44249 Kaunas
Spausdino leidyklos „Technologija“ spaustuvė, Studentų g. 54, 51424 Kaunas